CHARACTERIZATION AND MODELLING OF POLYMERIC BATTERY SEPARATORS FOR CRASH SAFETY SIMULATION

By

Shutian Yan

A DISSERTATION

Submitted to
Michigan State University
in partial fulfillment of the requirements
for the degree of

Mechanical Engineering - Doctor of Philosophy

2019

ABSTRACT

CHARACTERIZATION AND MODELLING OF POLYMERIC BATTERY SEPARATORS FOR CRASH SAFETY SIMULATION

By

Shutian Yan

For the safety design and integration of battery modules in vehicles, a thermo-electro-mechanical battery model for vehicle crash simulations is under development. The current research focuses on thermomechanical modeling of the battery separators. A separator is a porous membrane with a thickness of several dozen microns. It prevents physical contact between the positive and negative electrodes while enabling ionic transport. The integrity of the separator is critical to the safety of the batteries. Separator failure can lead to a thermal event. Commonly used polymeric separators are manufactured by dry process and have anisotropic microstructures. During thermal ramp, they first expand and then shrink before reaching the melting temperature. The amount of shrinkage can be over 10%. In a constrained condition, the shrinkage induces tensile stress in the separator. To model the material behavior in this range, quantitative measurements of thermal and mechanical properties are needed. The models for this application need to consider the anisotropy, rate and temperature dependence of the material properties, and thermal shrinkage.

Currently, the experimental data are incomplete for the development of such models. This is largely due to lack of characterization methods for thin polymeric membranes. In this research, experimental methods have been developed to measure the thermal and mechanical properties.

For the thermal property characterization, an experimental method has been developed to measure the thermal expansion/shrinkage and the coefficient of thermal expansion (CTE) using a dynamic mechanical analyzer (DMA). The measurements were carried out for three common types

of polymer based separators. The CTE as a function of temperature from ambient to near melting point was determined. The DMA offers continuous measurements in an automatic fashion, which is an efficient and convenient method to characterize the thermal expansion/shrinkage behavior of thin polymer films.

The mechanical behavior of an orthotropic material is described by the stress-strain relationships in the principal material directions and shear, and the Poisson's ratios. The measurements of the shear property and the Poisson's ratio for polymer films with a thickness of tens micrometers have not been well established. In this work, these measurements were attempted with a DMA. Digital image correlation (DIC) was used for strain measurements. The shear property was measured using the off-axis tensile experiment. Based on the analogy for anisotropy between the elastic and linear viscoelastic domains, the shear creep response was also measured. The creep compliances in shear and in the principal material directions were determined.

Due to its thin thickness, compression experiments with a single/a few layers of separator are difficult to perform. In this work, a capacitance based displacement set-up has been developed for the measurement of the through thickness direction compression stress-strain behavior of the separator and the investigation of its interaction with the electrode. The experiments were performed for a stack of two layers of separator, and separator/cathode/separator stack.

The thermomechanical model is developed on an orthotropic viscoelastic framework. A discretization algorithm has been proposed for the evaluation of a stiffness-based hereditary integral with a kernel of Prony series. The model has been implemented in commercial FE package LS-DYNA® as a user defined material model. The implemented model has been verified with analytical solutions and validated with experiments under uniaxial loading conditions. The model validation for biaxial loading cases is ongoing.

ACKNOWLEDGEMENTS

I would like to express my deepest appreciation to my advisor Dr. Xinran Xiao for her continuous guidance throughout my Ph.D study. She patiently guided me not only on solving specific problems, but also on the research methodologies. She trained me repeatedly to work smart and efficiently. Without her guidance, it would have been impossible for me to finish my Ph.D study. Her integrity, enthusiasm and standards of conduct set an excellent example for me to follow.

I would deeply thank my committee members Dr. Alfred Loos, Dr. Seungik Baek and Dr. Weiyi Lu for their helpful directions and suggestions on my researches. Additionally, special thanks to our collaborator Dr. Xiaosong Huang at General Motor R&D and Dr. Jie Deng and Dr. Chulheung Bae at Ford Motor Company for their insightful comments and discussions to the projects.

I am grateful for my labmates Miao Wang, Wu Zhou, Andy Vanderklok, Yalla Abushawashi, Wei Zhang, Danghe Shi, Christopher Cater, Wei Wu, Jim Dorer for their suggestions in my experiments and simulations. I would also thank the undergraduate assistances Yuhao He, Albert Asta, Zhengyuan Xie to repeat the experiments. I am thankful for the effort made by Beckett Clifford and Erik Stitt in CVRC lab to repair the machines. I appreciate the trainings from Michael Rich and assistances in experiments from Dr. Per Askeland in CMSC lab.

I would like to thank my parents, for their persistently support, encouragements and love.

This research is supported by the Ford/MSU Alliance Program. I would thank ME Department, College of Engineering, and Graduate School MSU for the funding support.

TABLE OF CONTENTS

LIST OF TABLES

LIST OF FIGURES

KEY TO ABBREVIATIONS

MD	Machine direction as 1st material directions of battery separator
TD	Transverse direction as 2nd material directions of battery separator
TTD	Through thickness direction as 3rd material directions of battery separator
DMA	Dynamic Mechanical Analyzer
CTE	Coefficient of Thermal Expansion
AR	Aspect Ratio

KEY TO SYMBOLS

E_{11}	modulus in the 1st material directions
E_{22}	modulus in the 2nd material directions
v_{12}	the major Poisson's ratio
v_{21}	the minor Poisson's ratio
G_{12}	in-plane shear modulus.
τ_{12}	in-plane shear stress
γ_{12}	in-plane engineering shear strain
σ	longitudinal stress
θ	the angle between the longitudinal direction and the 1st principal material direction
ε_0	strain measured by the virtual extensometers orientated at the MD
ε_{90}	strain measured by the virtual extensometers orientated at the TD
ε_{45°	strain measured by the virtual extensometer oriented at 45º to the MD
$J(t)$	creep compliance
$G(t)$	stress relaxation
G_i	stress relaxation constants
τ_i	relaxation times
C	capacitance
ε_0	permittivity of vacuum
ε_r	relative permittivity of the dielectric property of the medium
A	area of capacitor
t_m	thickness of dielectric medium

$\Delta l_{calibration}$	dimensional change of the testing fixture
$\Delta l_{predicted}$	predicted dimensional change over the gage length *l* of the sample
$\Delta l_{measrued}$	the measured dimensional change by the DMA
α	CTE
l_0	the initial sample length
T	temperature
T_0	the initial temperature
$\Delta l_{corrected}$	the true dimensional change of the sample
ε	engineering strain
T_{Shrink}	the temperature when the sample starts to shrink
T_1	maximum temperature where the stress decreased with increasing temperature in iso-strain test
T_2	maximum temperature where the stress increased with temperature in iso-strain test
T_f	temperature where the sample fractured in iso-strain test
a_T	time-temperature shifting function
Δt	time increment
σ_∞	long term relaxation stress in Prony Series
$\sigma^i(t)$	i^{th} individual Maxwell component in Prony Series
$\boldsymbol{\varepsilon}^{\mathbf{vol}}$	the volumetric component of strain
$\boldsymbol{\varepsilon}^{\mathbf{dev}}$	the deviatoric component of strain
$K(t)$	bulk relaxation modulus of isotropic material
$\mu(t)$	shear relaxation modulus of isotropic material
$G_{11}(t)$	MD relaxation modulus
$G_{22}(t)$	TD relaxation modulus

$G_{66}(t)$	in-plane shear relaxation modulus
$G_{13}(t)$	out-of-plane shear relaxation modulus
$G_{23}(t)$	out-of-plane shear relaxation modulus
v_{23}	out-of-plane Poisson's ratio
L_C	the shortest element size
ρ	specific mass density

CHAPTER 1 INTRODUCTION

The current investigation is originated from the needs to predict the mechanical response of the separators in lithium-ion batteries (LIBs) under various conditions, particularly in thermal ramp scenarios. The mechanical integrity of separator is critical to the safety of the LIBs. A short circuit due to separator failure can lead to a thermal event [1, 2].

1.1 Battery Separator in Lithium-ion Batteries

The separator provides electrical insulation between the opposite electrodes while allows ionic transport through the pores [3,4] as shown in Fig. 1.1 [5]. Three common types of separators are porous polymeric membranes, nonwoven mats, and ceramic enhanced membranes. Currently, polymeric membranes are used predominantly due to their low cost and thin thickness. A thin separator facilitates the ionic transport and provide higher energy and power densities [4]. Common polymer separators are in the range of several dozen micrometer thickness (<40μm).

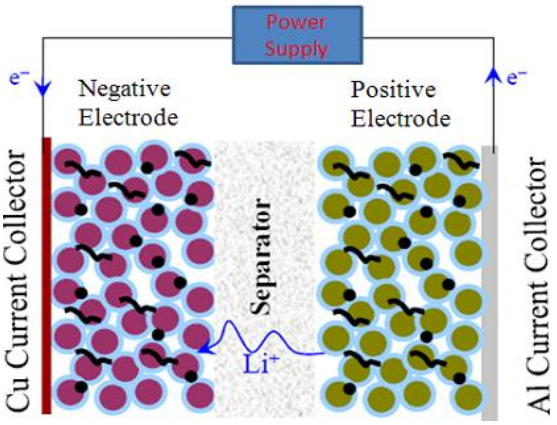

Figure 1.1 Schematic representation of a basic Li-ion battery single cell [5]

The process for making polymeric separators can be broadly divided into dry and wet processes [3]. Most of the polymer battery separators are dry processed, such as the commercially available Celgard® PE (Polyethylene) or PP (Polypropylene) single layer or their laminate

combination (trilayer PP-PE-PP) films. Therefore, only the dry process is discussed here. The dry process involves four steps: (1) melt-extrusion, (2) annealing to increase the size and amount of lamellae crystallites, (3) stretching, (4) heat fixation to stabilize the porous structure, reduce shrinkage and release internal stress. This process results in an anisotropic microstructure.

Figure 1.2 shows the typical surface microstructure and 3D representation of single layer PP separators. As seen, the pores are splits which are a fraction of micrometer long and tens to hundred nanometer apart. The fibrous liked structures that separates the splits are amorphous. The thick regions are semi-crystalline. The separator is usually treated as an orthotropic material with three material directions referred to as the machine direction (MD), the transverse direction (TD), and the through thickness direction (TTD).

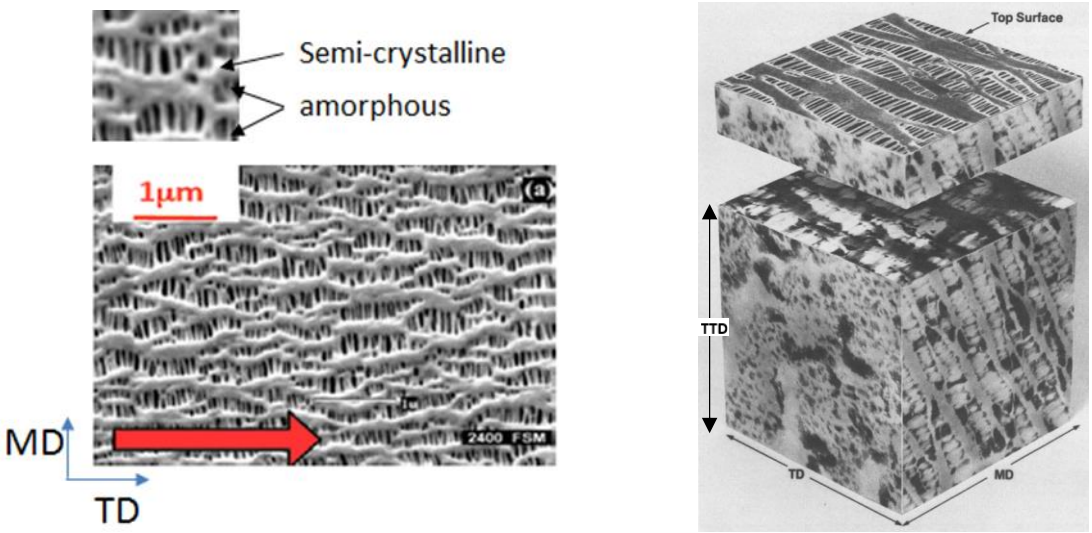

(a) (b)

Figure 1.2 (a): surface microstructure of Celgard® 2400 [3]. (b): 3D representation of Celgard® 2500 [6]. The three material directions are referred to as MD, TD, and TTD.

1.2 Modeling of the Separator

The mechanical integrity of the separator is critical to the safety of LIBs. For polymer separators, their thermomechanical property is of great concern, particular in thermal ramp

scenarios. It is known that, with increasing temperatures, polymer separators first expand and then start to shrink before final fracture/melting [3]. The amount of shrinkage can be significant for some separators [3]. In battery manufacturing, separators are sandwiched between electrodes, the sandwich layers are then wounded or stacked to form a battery cell, as shown in Fig. 1.3. In the stack, the separator is constrained by the rough surface of the electrodes. In a cylindrical or rectangular cell, the sandwich layer is constrained by cell casing. Pouch cells have a soft casing. Nevertheless, pouch cells are usually subjected to a compressive stress in a battery pack. In one word, in batteries, separators are not in a free-standing configuration. A larger shrinkage will induce higher stresses in the separator which may cause earlier failure.

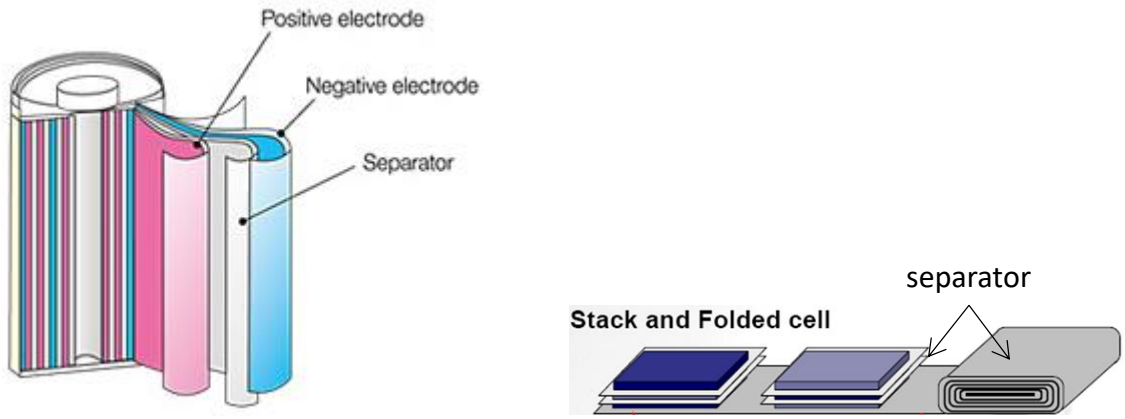

(a) (b)

Figure 1.3 Schematic of a cylindrical cell (left) [7] and a pouch cell (right) [8].

To model the thermomechanical behavior of separators in thermal ramp scenarios, at least four important aspects of constitutive behaviors must be included: (1) material anisotropy; (2) rate dependency [9-13]; (3) temperature dependency [9,11-13]; and (4) thermal shrinkage. To develop such a model, quantitative measurements of thermal and mechanical properties of the separators over this temperature range are needed.

So far, few works have modeled the separator in FEA explicitly and none of them has considered all four aspects of the constitutive behaviors. For example, the separators had been modeled as an isotropic viscoelastic material [14,15] which ignored the anisotropy; with an anisotropic honeycomb model which did not consider the time and temperature dependence [16]; and with an anisotropic viscoplastic Bergstrom-Boyce model [17] which did not consider the temperature dependence. In commercial finite element codes for crash safety simulation, e.g. LS-DYNA®, there is no suitable model to represent the orthotropic thermomechanical behavior of battery separators.

1.3 Objective and Scope of the Work

The overall objective of this work is to develop a thermomechanical material model for battery separator for the analysis of thermal ramp scenarios. As discussed in 1.2, the model should consider (1) material anisotropy; (2) rate dependency; (3) temperature dependency; and (4) thermal shrinkage. The first three aspects can be modeled with an orthotropic thermoviscoelastic model. The last aspect can be considered by coupled thermal-mechanical analysis, provided that the thermal expansion/shrinkage property is known.

The work presented in this thesis is the first step in this process.

The model development requires a complete set of experimental data. As to be discussed in Chapter 2, the available data are far from complete. Furthermore, certain properties have not been reported previously for thin polymer films. The experimental techniques and the testing methodologies are yet to be developed.

In this thesis, the experimental methods for the measurement of TTD compression, the thermal expansion/shrinkage property, and the characterization of orthotropic properties of thin

polymer films were investigated. A common type of PP separator Celgard® 2400 was used in most of the experiments.

For model development, a model based linear viscoelastic framework has been completed and implemented as a user material model in a commercial FEA package LS-DYNA®.

The thesis is organized as follows.

Chapter 1 introduces the problem and defines the scope of work.

Chapter 2 presents a brief review on the characterization techniques, the available experiment data on the rate and temperature dependent behavior of common separators, and thermoviscoelastic models.

Chapter 3 presents the methodology for the measurement of stress-strain relationships and the Poisson's ratios for an orthotropic thin film. With digital image correlation (DIC) technique, the shear property was measured with off-axis tension. The creep compliances in principle directions and in shear were determined.

Chapter 4 presents the development of a capacitance-based displacement set-up for the measurement of TTD compression stress-strain behavior of the separator. The interaction between the separator and the electrodes are also investigated by this set-up.

Chapter 5 presents the development of an experimental method for the measurement of coefficient of thermal expansion (CTE) of thin polymer films using a dynamic mechanical analyzer (DMA). The expansion/shrinkage property were determined for three typical separators: Celgard® 2400 (monolayer PP), Celgard® 2325 (trilayer PP/PE/PP), and Celgard® Q20S1HX (ceramic coated trilayer PP/PE/PP).

Chapter 6 presents the measurement of creep compliances at elevated temperatures. A master curve was constructed to yield the time-temperature shift factor.

Chapter 7 presents the formulation and implementation of an orthotropic linear viscoelastic material model in LS-DYNA, and its verification.

Chapter 8 provides a summary and major conclusion of this thesis, and future work.

REFERENCES

REFERENCES

1. M.D. Farrington, Proposed Amendments to UNST/SG/AC.10/11: Transport of Dangerous Goods-Lithium Batteries, Journal of Power Sources, 80 (1999) 278-285.

2. M.D. Farrington, Safety of Lithium Batteries in Transportation, Journal of Power Sources, 96 (2001) 260-265.

3. P. Arora, Z. Zhang, Battery Separators, Chemical Reviews, 104 (2004) 4419–4462.

4. S.S. Zhang, A review on the separators of liquid electrolyte Li-ion batteries, Journal of Power Sources, 164 (2007) 351–364.

5. S.J. Harris, A. Timmons, D.R. Baker, C. Monroe, Direct in situ measurements of Li transport in Li-ion battery negative electrodes, Chemical Physics Letters, 485 (2010) 265–274.

6. T. Sarada, L.C. Sawyer, M.I. Ostler, Three dimensional structure of Celgard® microporous membranes, Journal of Membrane Science, 15 (1983) 97–113.

7. http://global.kawasaki.com/en/energy/solutions/battery_energy/about_gigacell/structure.html

8. M. Alamgir, Presentation at the 26th International Battery Seminar & Exhibit, Fort Lauderdale, FL, March 16–19 (2009).

9. J. Zhu, T. Wierzbicki, W. Li, A review of safety-focused mechanical modeling of commercial lithium-ion batteries, Journal of Power Sources, 378 (2018) 153–168.

10. A. Sheidaei, X. Xiao, X. Huang, J. Hitt, Mechanical behavior of a battery separator in electrolyte solutions, Journal of Power Sources, 196 (2011) 8728-8734.

11. J. Xu, L. Wang, J. Guan, S. Yin, Coupled effect of strain rate and solvent on dynamic mechanical behaviors of separators in lithium ion batteries, Materials & Design, 95 (2016) 319-328.

12. I. Avdeev, M. Martinsen, A. Francis, Rate- and Temperature-Dependent Material Behavior of a Multilayer Polymer Battery Separator, Journal of Materials Engineering and Performance, 23 (2013) 315–325.

13. J. Cannarella, X. Liu, C.Z. Leng, P.D. Sinko, G.Y. Gor, C.B. Arnold, Mechanical Properties of a Battery Separator under Compression and Tension, Journal of The Electrochemical Society, 161 (2014) F3117–F3122.

14. W. Wu, X. Xiao, X. Huang, S. Yan, A multiphysics model for the in-situ stress analysis of the separator in a lithium-ion battery cell, Computational Materials Science, 83 (2014) 127-136.

15. R. Behrou, A Thermo-Poro-Viscoelastic Model for the Behavior of Polymeric Porous Separators, ECS Transactions, 80 (2017) 583-591.

16. X. Zhang, E. Sahraei, K. Wang, Deformation and failure characteristics of four types of lithium-ion battery separators, Journal of Power Sources, 327 (2016) 693–701.

17. M. Martinsen, Material Behavior Characterization of a Tin Film Polymer Used in Lithium-Ion Batteries (Master thesis), University of Wisconsin-Milwaukee, 2012.

CHAPTER 2 LITERATURE REVIEW

This chapter presents a review of characterization techniques, experiment results and thermomechanical modeling.

2.1 Characterization Techniques

To model the mechanical behavior of an orthotropic material requires the knowledge of the stress-strain relationships in the principal material directions and shear, and the Poisson's ratios. A model based on an orthotropic viscoelastic framework will also require the viscoelastic functions in these directions. This section summarizes the characterization techniques.

2.1.1 In plane

For common types of polymer separator, the stress-strain relations in the MD and TD are available [1-8]. They can be measured by DMA or common tensile test machine. However, the data on Poisson's ratio and shear properties are scarce. The viscoelastic measurement for polymer separators has only been reported for the MD [1,2].

The shear property of an orthotropic material may be measured by an off-axis tensile experiment. This method has been widely used in the shear property measurement of unidirectional composites [9-11]. It has also been used in measuring the shear modulus of polymer thin films [12,13] but the details of the experiments were not provided.

2.1.2 In the Through Thickness Direction (TTD)

The characterization of the TTD mechanical properties is far more challenging. It requires a displacement measurement with a submicron resolution and a high parallelism in loading. Limited by the resolution of conventional displacement measurement methods such as the linear variable differential transformers (LVDT), the compression measurements have been performed

with a stack of 32, 40 and 224 layers of separator [6,14-16]. For commercial separator with MD and TD directions, to ensure the measurement accuracy, the samples need to be carefully aligned in the same direction in the stack to avoid the trapping of thin air layers between the layers. Nanoindentation is another technique which has been used for such measurements. Nanoindentation can achieve a high resolution in TTD displacement measurement. However, as the radius of the indenter tip is comparable to the size of the microscopic features of the separators, the measured property depended on the locations of the indentation [17]. In addition, the nanoindentation measures the surface properties, not exactly the bulk properties in the TTD. For the purpose of the quick screening of separator materials and the accurate measurements of the material stress-strain responses, it is desirable to have a technique to measure the compression response using a single layer/a few layers of separator.

In the literature, a number of techniques have been investigated for thin film thickness measurement, including the capacitance based displacement measurement technique [18–23], prism coupling technique [24], hydrostatic strain measurement technique [25], picosecond laser ultrasonics [26], Brillouin light scattering technique [27].

Compared to other methods, the investment for the experimental set-up with the capacitance technique is relatively low, and the capacitance sensor can be incorporated in a compression test as demonstrated in the measurement of the elastic modulus of solid films of 75 μm [18] and 4–20 μm thicknesses [20]. The principle of the capacitance technique and previous reported efforts using this method are reviewed here.

Parallel plate capacitors (PPC) have been used widely as a displacement/thickness sensor. The capacitance C of two parallel conductive plates facing each other with an area A and a separation distance/thickness t is given by

$$C = \frac{\varepsilon_0 \varepsilon_r A}{t} \tag{2.1}$$

where ε_0 is permittivity of vacuum as 8.854pF/m, ε_r is the relative permittivity of the dielectric property of the medium which fills *t*. *C* can be measured by a capacitance meter. Once ε_r is known, *t* can be calculated.

Capacitance based displacement technique is suitable for thin film behavior characterization in the through-thickness direction because *t* is reciprocal to the measured quantity-*C* in Eq. 2.1. Smaller thickness can magnify the capacitance response if the other parameters are the same. The displacement resolution can be higher when thinner sample is tested because the capacitance change ΔC is reciprocal to t^2 by the derivative of Eq. 2.1 as $\Delta C = -\frac{\varepsilon_0 \varepsilon_r A}{t^2}$.

In a capacitance based displacement measurement, the specimen can be placed either in in-situ [19,21] or ex-situ configurations [18,20].

2.1.2.1 In-situ experiment

In-situ experiments use sample/film as the dielectric medium in capacitor. In this case, the capacitance increase is not only caused by the sample thickness reduction, but also by the increase of dielectric permittivity ε_r with reducing the sample thickness. To consider this coupled effect, ref.23 presented a method that required the use of two separate fixtures simultaneously during in-situ experiment. The first fixture is shown in Fig. 2.1a [21]. Polymer sample is sandwiched between electrodes of parallel plate capacitor as dielectric medium. The fixture will be compressed using a load frame. The capacitance increases according to Eq. 2.1 as a result of the decrease in thickness *t* and increase in relative permittivity ε_r due to charge density increment. To determine the change in thickness *t*, the influence of the relative permittivity ε_r needs to be decoupled.

Interdigitated electrodes (IDE) as shown in Fig. 2.1b [21] can realize this function. This fixture with sample will be compressed by the load frame. The IDE are designed in a way that the measured capacitance is only affected by the change of ε_r of the polymer, but not by the change of *t*. To satisfy this requirement, the geometry parameters, e.g. electrode digit width *W*, are determined by electrostatic FEM simulation. Simulation results shows that by choosing a proper ratio of *t*/*W*, most of the energy of the fringing electric fields as shown in Fig. 2.1c [28] can be contained only within the polymer and the substrate, and very little energy can reach beyond the polymer surface. When the maximum strain is very small like 1%, this condition is still satisfied. Therefore, the influence of relative permittivity can be obtained and the thickness change during compression can be measured.

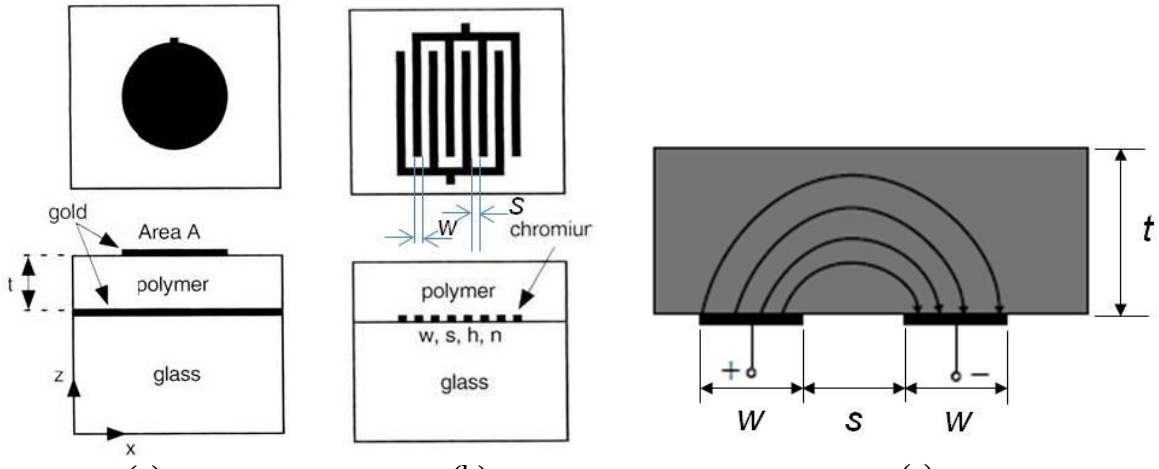

(a) (b) (c)

Figure 2.1 Schematic representation of (a) Parallel plate capacitor (b) Interdigitated electrodes [21] (c) Fringing electric field between two electrode digits with width *W* and space *S* [28]

2.1.2.2 Ex-situ experiment

The ex-situ experiments usually use air as the dielectric in the capacitor. Unlike in-situ experiment, the relative permittivity of the air does not change if it can diffuse away freely. Therefore, the capacitance is only a function of air gap thickness.

For ex-situ experiments, two fixtures designs have been reported in literature [18,20]. Fig. 2.2a shows the design presented in [18]. This fixture can be used in conjunction with a conventional load frame, such as Instron or MTS. The target plate and housing worked as compression platens with samples spaced between them. To reduce the alignment problem, a single point loading scheme is used by placing a ball bearing in the center of the upper surface of the target plate. The capacitance gauges were used to measure the air gap thickness between the target plate and housing. They were embedded in the housing, secured by the set screws. Using the measured capacitance, the air gap thickness can be calculated. As the air gap thickness is equal to the sample thickness, the sample thickness can be known. This fixture has an advantage that the commonly encountered machine stiffness problem in film compression test can be eliminated because the capacitor directly measures the thickness of the air gap/the sample.

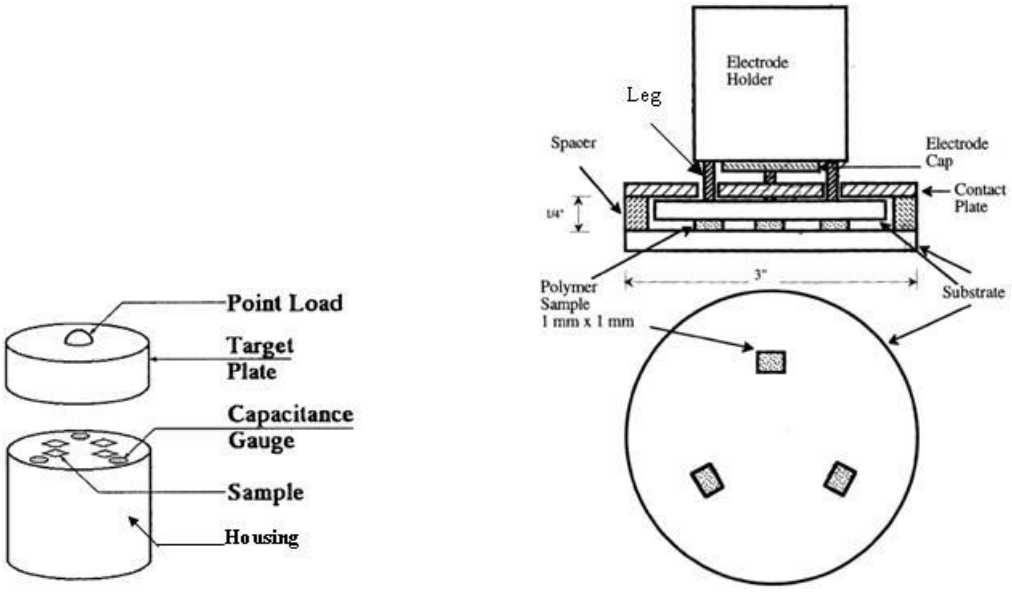

(a) (b)

Figure 2.2 Fixture presented in (a) [18] (b)[20]

The fixture discussed in [20] is shown in Fig. 2.2b. Three pieces of polymer samples are placed between two parallel substrates to self-align the substrates during compression. The compressive force is transmitted from the electrode holder to the upper substrate through three

legs connecting them. A capacitor using air as the dielectric medium is formed between the electrode cap and the contact plate. Using the measured capacitance, the air gap thickness can be calculated. The decrease in air gap thickness is equal to the decrease in sample thickness because the contact plate-1/4" spacer-lower substrate are stationary while the electrode holder-three legs-upper substrate move together. The disadvantage of this fixture is that it requires high precision machining.

2.1.3 Thermal Shrinkage

The standard methods determine the CTE of a material through measuring the volume or lengthwise change of a free standing sample [29,30]. These techniques are not suitable for materials in the form of thin films.

For thin films, several CTE measurement techniques have been reported. A common method is laying an unconstrained sample on a flat surface in an oven with an optical window and using non-contact optical methods such as interferometry [31] or digital image correlation [32] to measure the dimensional change. For metal foils, the CTE can be measured using a bi-layer configuration with a substrate of known CTE [33]. The optical measurement requires special equipment. The bi-layer configuration is not suitable for polymer thin films because the stiffness of these materials is too low to generate needed deformation with commonly used substrates.

The thin film CTE measurement has also been attempted for a clamped sample. El-Tonsy [34] presented a system that measures the length change of a clamped polymer film sample under a small hanging weight. This system has some similarity to the thermal mechanical analyzer (TMA) DMA commonly used in polymer characterization. TMA [35,36] and DMA [1,2,37,38] have been used widely in the characterization of battery separators. Baldwin et al [37] characterized the

shrinkage of battery separators under isothermal conditions using a DMA under tensile mode. These works indicate the potential of TMA and DMA in thin film CTE measurement.

2.2 Available Data

2.2.1 Stress-Strain Behavior In Air and In Solvent

The mechanical properties of the separators are commonly measured in tension in the two in-plane directions, i.e. MD and TD [1-8], and in compression in TTD [6, 14-16]. The typical stress-strain curves of Celgard® 2400 are shown in Fig. 2.3. Celgard® 2400 exhibits a softer stress-strain response in electrolyte solutions such as DMC and EC/DMC [2]. This effect is more noticeable in MD as the DMC molecules can penetrate the fibrous amorphous regions of the separator much easier than the semi-crystalline regions [39]. Table 2.1 provides a summary of the elastic moduli of Celgard® 2400 in three material directions in air and in DMC. The ratio of the modulus in DMC to that in air is 0.49 in MD, 0.88 in TD, and 0.84 in TTD.

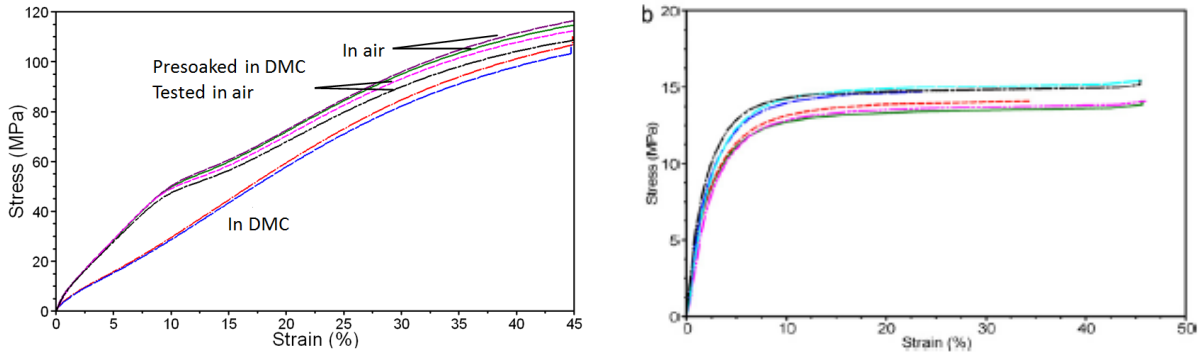

(a) (b)

Figure 2.3 The stress–strain curves of Celgard® 2400. (a) MD tensile in air and in DMC[2]. (b) TD tensile in air[2]. (c) TD tensile in DMC[2]. (d) TTD compression[40].

Figure 2.3(cont'd)

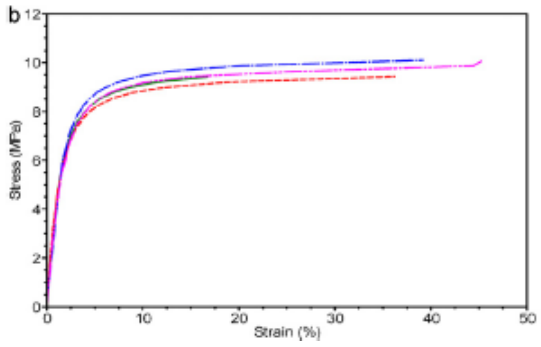

(c)

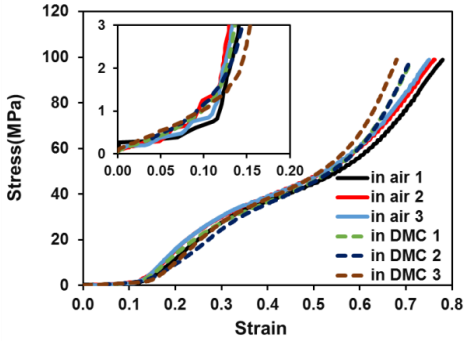

(d)

Table 2.1 The Elastic Modulus of Celgard® 2400 in Air and in DMC

Modulus / Test	In Air (GPa)	In DMC (GPa)	DMC/Air Ratio
MD tensile [2]	0.843±0.020	0.409±0.028	0.49
TD tensile [2]	0.430±0.028	0.377±0.010	0.88
TTD compression [40]	0.191±0.020	0.165±0.020	0.84

Figure 2.3 shows that the shapes of the tensile stress-strain curves in MD and TD are very different. The stress-strain curve in TD exhibits a clear yielding point. Although DMC has a relatively samll effect on the TD tensile modulus, its effect on TD yield is much greater. The yield stress is lowered from 14.2MPa in air to 9.6MPa in DMC [2].

2.2.2 Strain Rate Dependent Behavior

Strain rate dependent tensile behaviors of various separators have been investigated widely: Celgard® 2400 and Celgard® 2340 trilayer separator in air and in DMC [1], Celgard® 2400 in air and in Lithium salted electrolyte solution [8], Celgard® 3501 PP separator in air and in DMC [6], Celgard® 2325 trilayer separator in air [7], and Celgard® C480 trilayer separator in air and in DMC [3]. These separators display strong rate dependent behaviors, as shown in Fig. 2.4 for Celgard®

2400 as an example along MD and TD in air, and in Fig. 2.5 in DMC. The stress-strain response of trilayer separator Celgard® 2340 is similar to that of Celgard® 2400 [1].

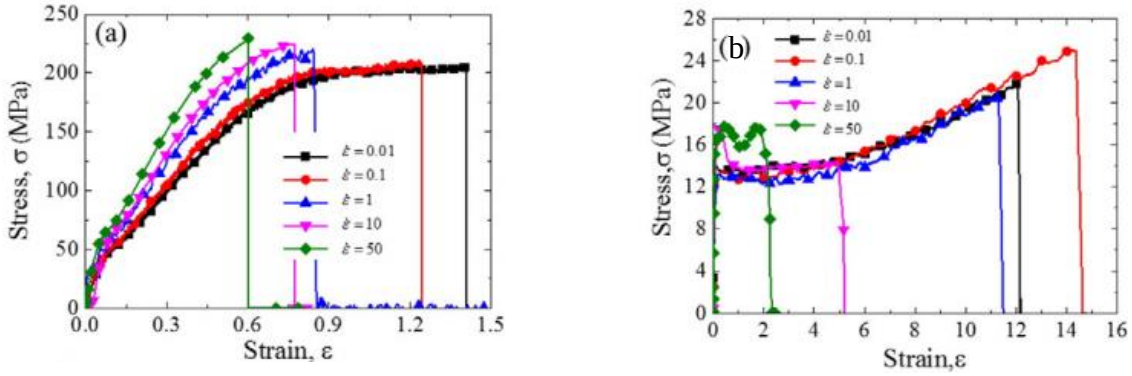

(a) (b)

Figure 2.4 Stress–strain curves under different strain rates in air for Celgard® 2400 [1] (a) MD; (b) TD.

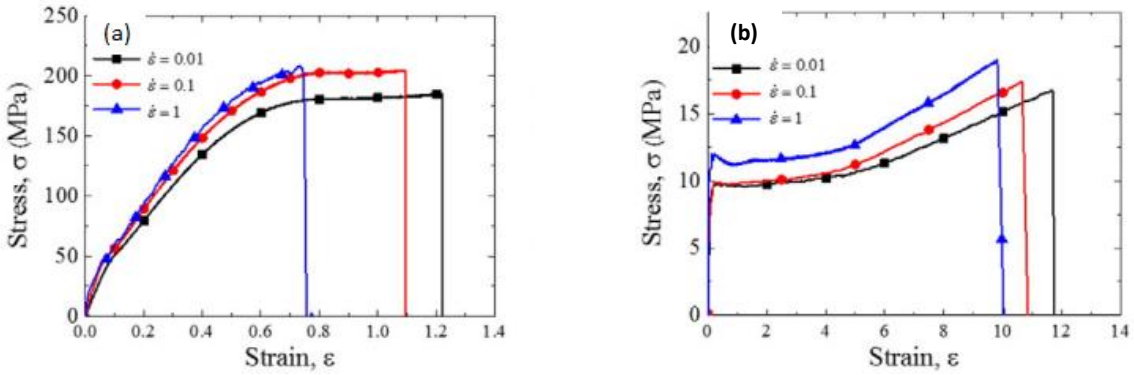

(a) (b)

Figure 2.5 Stress–strain curves under different strain rates in DMC for Celgard® 2400 [1] (a) MD; (b) TD.

Rate dependent TTD compressive behavior has been studied for Celgard® 3501 PP separator in air and in DMC [6]. Fig 2.6a shows softening in DMC was present at strain rates smaller than about $10^{-2}s^{-1}$. At higer strain rates, the poroelastic effects due to fluid immersion stiffen the response. Therefore, the effective modulus in DMC was gradually increased and even become larger than that in air.

Compared with the effective tensile modulus along MD and TD as shown in Fig. 2.6b&c, the effective compressive modulus along TTD is more similar in value to the one along TD under tension, both of which are much smaller than the one along MD in tension. This is due to that only MD is significantly strengthened through the uniaxial stretching process during manufacturing while both TD and TTD are not hardened [6].

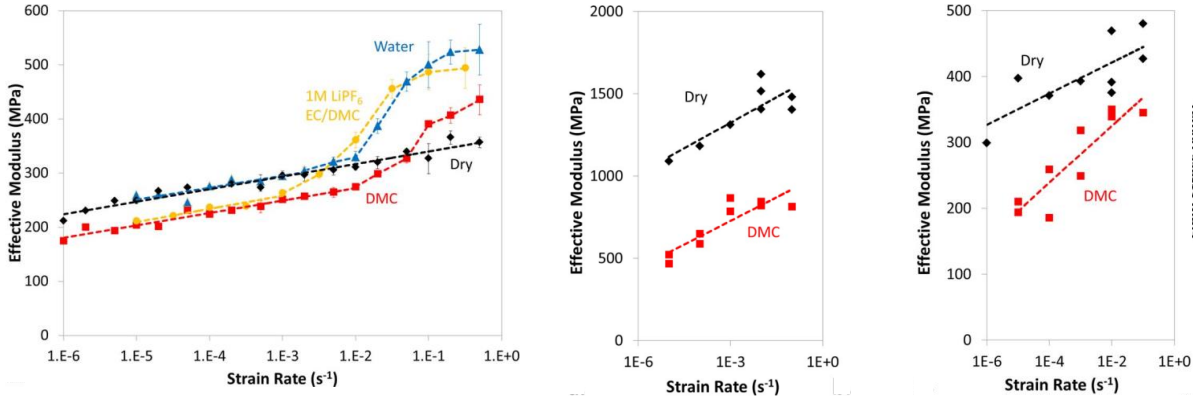

Figure 2.6 Rate dependent modulus for Celgard® 3501 [6] (a) TTD in compression; (b) MD in tension; (c) TD in tension.

2.2.3 Temperature Dependent Behavior

Strain-strain behavior has been measured by several researchers. Zhang et al measured the tensile stress-strain curves of dry-processed PP separator up to 60ºC in air [41]. Avdeev et al [3] measured the tensile stress-strain curves of trilayer Celgard® C480 at 28, 55 and 80ºC in air and in DMC, as shown in Fig. 2.7. Kalnaus et al [7] measured the in-plane tensile stress-strain curves and through thickness compressive stress-strain curve of trilayer Celgard® 2325 up to 120 ºC in air. In all these tests, the separators were structurally anisotropic. Along MD, it showed viscoelastic behavior up to 40% strain. Along TD, it showed elastic-plastic behavior.

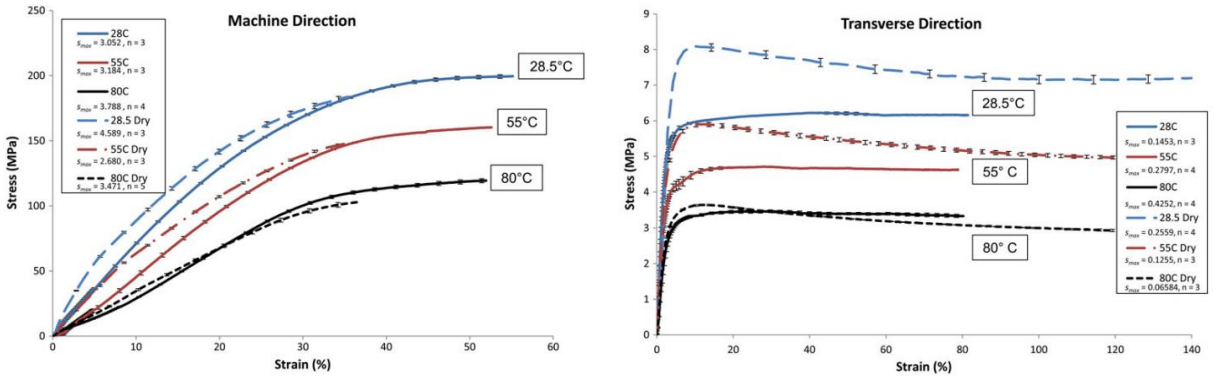

(a) (b)

Figure 2.7 Celgard® C480 stress–strain curves at 28, 55 and 80ºC in air and in DMC [3] along (a) MD (b) TD.

2.2.4 Thermal Shrinkage

Love [38] investigated the thermal shrinkage of Celgard® 2320 and Entek® Gold LP using DMA. Celgard® 2320 is a trilayer PP/PE/PP separator. The behavior of Celgard® 2320 is also similar to Celgard ®2400. On the other hand, Entek® Gold LP, made of Ultra-high-molecular-weight polyethylene (UHMWPE), displays a nearly isotropic in-plane property. Figure 2.8 presents the thermal shrinkage of these two separators.

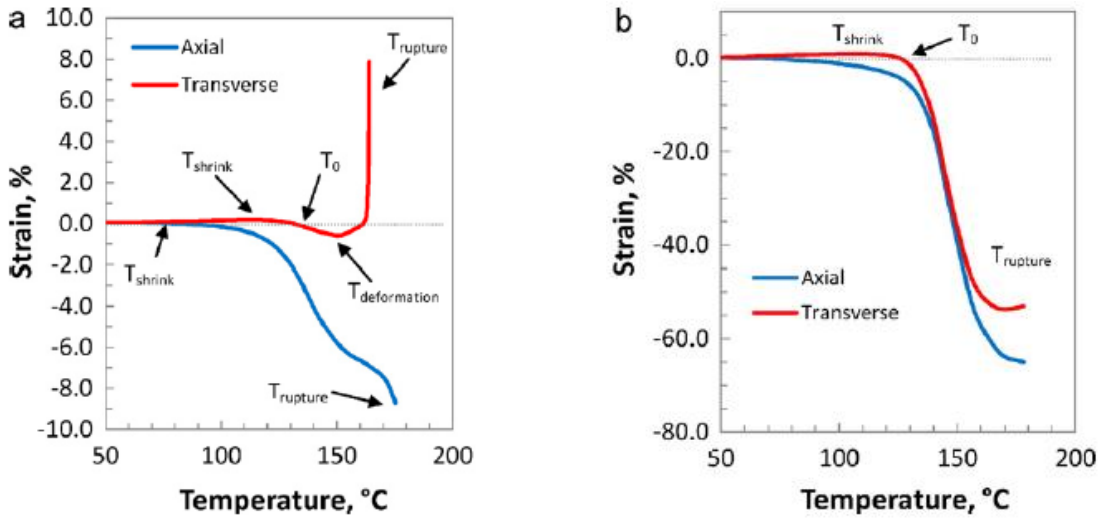

(a) (b)

Figure 2.8 Thermomechanical behavior of (a) Celgard® 2320, an anisotropic battery separators (this behavior is also typical for polymer separators: Celgard® 2400 and Celgard® 2500) and (b) Entek® Gold LP, a nearly isotropic biaxial battery separator, with static load applied in the axial

Figure 2.8(cont'd) and transverse-directions [38].

2.3 Thermomechanical Modeling

As shown in 2.2, the typical Celgard® separators are structurally anisotropic materials with different behavior up to failure in MD, TD and TTD. As the first step, it can be considered as orthotropic material in linear elastic region. To model the separator, four constitutive behaviors are critical as emphasized in Section 1.2: (1) anisotropy; (2) temperature dependency; (3) rate dependency; and (4) thermal shrinkage.

2.3.1 Evaluation of Material Models in LS-DYNA

Modeling of thermal ramp scenarios is most likely to be coupled with vehicle crash analysis. The most widely used FEA package in vehicle crash analysis is LS-DYNA®. LS-DYNA® has close to 300 material models. These models were evaluated for separator modeling.

Table 2.2 summarizes this evaluation. It should be noted that there are numbers of material models bearing "anisotropic" in their name. However, a close examination shows that most of these models are based on an isotorpic elastic framework and the anisotropy is only considered in yield flow behavior. Therefore, the model evaluation emphasizes three capabilities: elastic anisotropy, strain rate dependency, and temperature dependency.

Models for metallic materials, such as 24, 33, 36, 37, and etc., are based on an isotropic elastic framework. These models generally consider the strain rate effect on the yielding stress and flow curve. Some advanced models consider anisotropic plasticity. However, none of these models considers the temperature dependency of the material properties.

Models for orthotropic materials, such as 40, 86, 108, and etc., are based on an orthotropic elastic framework. Some can consider nonlinear behavior. However, none of these models considers the temperature dependency of the material properties.

Models for viscoelastic materials, such as 6, 61, 76, 86, 134, 164, 234, 276, and etc., are based on an isotropic viscoelastic framework. These models consider the strain rate dependency but not the temperature dependency.

Models for hyper-elasticity, viscoplasticity, such as 53, 73, 77, 87, 91, 124, 127, 129, and etc., consider the strain rate dependency but not the temperature dependency.

MAT_224 (MAT_TABULATED_JOHNSON_COOK) is a recent development. It allows tabulated data input [42] with the rate dependent and temperature dependent properties. However, MAT_224 is isotropic model. Its anisotropic version MAT_213 is currently under development. It has been confirmed that MAT_213 does not consider the temperature dependency [43].

The results show that no one model can satisfy all three requirements. Therefore, a user thermomechanical material model needs to be developed. An orthotropic thermo-viscoelastic model has been identified for this development.

Table 2.2 Evaluation of Material Models in LS-DYNA® for Separator Modeling

Model types	Examples	Elastic Anisotropy	Strain Rate Dependency	Temperature Dependency
Metals	24, 33, 36, 37…	×	✓	×
Orthotropic	40, 86, 108, …	✓	×	×
Viscoelastic	6, 61, 76, 86, 134, 164, 234, 276, …	×	✓	×
Hyper-Elasticity, Viscoplasticity	53, 73, 77, 87, 91, 124, 127, 129, …	×	✓	×

Table 2.2 (cont'd)

Tabulated	224	×	✓	✓

2.3.2 Thermoviscoelastc Material Model

A framework of thermoviscoelasticity for PE thin films used in the NASA superpressure balloons has been proposed by Li et al. in [12]. Based on the time-temperature superposition principle (TTSP) of the viscoelasticity theory, the stress-strain behavior of a linear viscoelastic material is described as [12]

$$\varepsilon(t) = \int_0^t D(t-s)\frac{d\sigma}{ds}ds + \int_0^t \alpha \frac{dT}{ds}ds \tag{2.2}$$

where $D(t)$ the creep compliance matrix and α is the CTE.

For the plane stress condition

$$\sigma[t] = \begin{bmatrix} \sigma_1(t) \\ \sigma_2(t) \\ \sigma_6(t) \end{bmatrix} \tag{2.3}$$

$D(t)$ is reduced to

$$[D(t)] = \begin{bmatrix} D_{11}(t) & D_{12}(t) & 0 \\ D_{21}(t) & D_{22}(t) & 0 \\ 0 & 0 & D_{66}(t) \end{bmatrix} \tag{2.4}$$

The components of the compliance matrix are often expressed by Prony series

$$D(t) = D_0 + \sum_{i=1}^{n} D_i\,(1 - exp(-t/\tau_i)) \tag{2.5}$$

where t is time, D_0 is the instantaneous compliance, D_i are the creep constants, and τ_i are the corresponding retardation times.

With the TTSP, the effect of temperature is represented using a master curve and a time-temperature shifting function a_T. Eq. 2.2 can then be expressed in terms of reduced time *t'* to account for temperature effect as

$$\varepsilon(t') = \int_0^{t'} D(t'-s)\frac{d\sigma}{ds}ds + \int_0^t \alpha\frac{dT}{ds}ds \tag{2.6}$$

where $t' = \int_0^t \frac{ds}{a_T(s)}$. The final expression of evaluation of hereditary integral in Eq. 2.6 could be found in [12]. However, the procedure was not shown.

REFERENCES

REFERENCES

1. J. Xu, L. Wang, J. Guan, S. Yin, Coupled effect of strain rate and solvent on dynamic mechanical behaviors of separators in lithium ion batteries, Materials & Design, 95 (2016) 319–328.

2. A. Sheidaei, X. Xiao, X. Huang, J. Hitt, Mechanical behavior of a battery separator in electrolyte solutions, Journal of Power Sources, 196 (2011) 8728–8734.

3. I. Avdeev, M. Martinsen, A. Francis, Rate- and Temperature-Dependent Material Behavior of a Multilayer Polymer Battery Separator, Journal of Materials Engineering and Performance, 23 (2013) 315–325.

4. J. Chen, Y. Yan, T. Sun, Y. Qi, X. Li, Deformation and fracture behaviors of microporous polymer separators for lithium ion batteries, RSC Advances, 4 (2014) 14904.

5. G. Venugopal, J. Moore, J. Howard, S. Pendalwar, Characterization of microporous separators for lithium-ion batteries, Journal of Power Sources, 77 (1999) 34–41.

6. J. Cannarella, X. Liu, C.Z. Leng, P.D. Sinko, G.Y. Gor, C.B. Arnold, Mechanical Properties of a Battery Separator under Compression and Tension, Journal of The Electrochemical Society, 161 (2014) F3117–F3122.

7. S. Kalnaus, Y. Wang, J. Li, A. Kumar, J.A. Turner, Temperature and strain rate dependent behavior of polymer separator for Li-ion batteries, Extreme Mechanics Letters, 20 (2018) 73-80.

8. J. Chen, H. Hu, S. Li, Y. He, Evolution of mechanical properties of polypropylene separator in liquid electrolytes for lithium-ion batteries, Journal of Applied Polymer Science, 135 (2018) 46441.

9. M.J. Pindera, C.T. Herakovich, Shear Characterization of Unidirectional Composites with the Off-Axis Tension Test, Experimental Mechanics, 26 (1986) 103-112.

10. I.M. Daniel, O. Ishai, Engineering Mechanics of Composite Materials, Oxford University Press, New York, 1994.

11. L.A. Carlsson, R.B. Pipes, Experimental Characterization of Advanced Composite Materials, Technomic Publishing Company, Lancaster (1997).

12. J. Li, K. Kwok, S. Pellegrino, Thermoviscoelastic models for polyethylene thin films, Mechanics of Time-Dependent Materials, 20 (2016) 13-43.

13. J. Zhu, X. Zhang, T. Wierzbicki, Stretch-induced wrinkling of highly orthotropic thin films, International Journal of Solids and Structures, 139-140 (2018) 238-249.

14. X. Zhang, E. Sahraei, K. Wang, Li-ion Battery Separators, Mechanical Integrity and Failure Mechanisms Leading to Soft and Hard Internal Shorts, Scientific Reports, 6 (2016) 32578.

15. X. Zhang, E. Sahraei, K. Wang, Deformation and failure characteristics of four types of lithium-ion battery separators, Journal of Power Sources, 327 (2016) 693–701.

16. M. Gilaki, I. Avdeev, Impact modeling of cylindrical lithium-ion battery cells: a heterogeneous approach, Journal of Power Sources, 328 (2016) 443–451.

17. I.C. Halalay, M.J. Lukitsch, M.P. Balogh, C.A. Wong, Nanoindentation testing of separators for lithium-ion batteries, Journal of Power Sources, 238 (2013) 469–477.

18. T.Y. Wu, D.L. Questad, Mechanical Characterization and Constitutive Description of Thin-Film Polymeric Materials, in: Symposium G – Electronic Packaging Materials Science VI, (1992) 143-161.

19. K.S. Patel, P.A. Kohl, S.A. Bidstrup-Allen, Novel technique for measuring through-plane modulus in thin polymer films, IEEE Transactions on Components, Packaging, and Manufacturing Technology: Part B. 21 (1998) 199–202.

20. H.C. Liou, R. Willecke, P.S. Ho, Study of out-of-plane elastic properties of PMDA-ODA and BPDA-PDA polyimide thin films, Thin Solid Films, 323 (1998) 203–208.

21. K.S. Patel, P.A. Kohl, S.A. B. Allen, Dual capacitor technique for measurement of through-plane modulus of thin polymer films, Journal of Polymer Science Part B Polymer Physics, 38 (2000) 1634–1644.

22. M. van Soestbergen, L.J. Ernst, K.M.B. Jansen, W.D. van Driel, M. Bartek, A. Polyakov, Measuring in-thickness mechanical properties of submicron polymer dielectric films, in: EuroSime 2006 - 7th International Conference on Thermal, Mechanical and Multiphysics Simulation and Experiments in Micro-Electronics and Micro-Systems, (2006) 1–5.

23. M. van Soestbergen, L.J. Ernst, K.M.B. Jansen, W.D. van Driel, Measuring the through-plane elastic modulus of thin polymer films in situ, Microelectronics Reliability, 47 (2007) 1983–1988.

24. F. Ay, A. Kocabas, C. Kocabas, A. Aydinli, S. Agan, Prism coupling technique investigation of elasto-optical properties of thin polymer films, Journal of Applied Physics, 96 (2004) 7147–7153.

25. M.J. Chen, Pressure -volume -temperature and wave propagation studies of polyimide films (Doctoral dissertation), University of Massachusetts Amherst, 1998.

26. H.T. Grahn, H.J. Maris, J. Tauc, Picosecond ultrasonics, IEEE Journal of Quantum Electronics, 25 (1989) 2562–2569.

27. S.T. Bailey, Transparent Tissues and Porous Thin Films: A Brillouin Light Scattering Study (Doctoral dissertation), The Ohio State University, 2013.

28. M. Vakilian, B.Y. Majlis, Study of interdigitated electrode sensor for lab-on-chip applications, 2014 IEEE International Conference on Semiconductor Electronics (ICSE), (2014) 201–204.

29. ASTM D696 Test Method for Coefficient of Linear Thermal Expansion of Plastics Between -30°C and 30°C with a Vitreous Silica Dilatometer, ASTM International.

30. ASTM E831-06 Standard Test Method for Linear Thermal Expansion of Solid Materials by Thermo-mechanical Analysis, ASTM International.

31. C. Dudescu, J. Naumann, M. Stockmann, S. Nebel, Characterization of thermal expansion coefficient of anisotropic materials by electronic speckle pattern interferometry, Strain, 42 (2006) 197–205.

32. P. Bing, X. Hui-min, H. Tao, A. Asundi, Measurement of coefficient of thermal expansion of films using digital image correlation method, Polymer Testing, 28 (2009) 75–83.

33. W. Fang, C. Lo, On the thermal expansion coefficients of thin films, Sensors and Actuators A: Physical, 84 (2000) 310–314.

34. M.M. El-Tonsy, Automatic measurement of the absolute CTE of thin polymer samples: I—effect of multiple processing on thermal expansion of polypropylene films, Polymer Testing, 23 (2004) 355–360.

35. P. Arora, Z.M. Zhang, Battery Separators, Chemical Reviews, 104 (2004) 4419–4462.

36. B. Xiong, R. Chen, F. Zeng, J. Kang, Y. Men, Thermal shrinkage and microscopic shutdown mechanism of polypropylene separator for lithium-ion battery: In-situ ultra-small angle X-ray scattering study, Journal of Membrane Science, 545 (2018) 213–220.

37. R.S. Baldwin, W.R. Bennet, E.K. Wong, M.R. Lewton, M.K. Harris, Battery Separator Characterization and Evaluation Procedures for NASA's Advanced Lithium-Ion Batteries, NASA/TM-2010-216099.

38. C.T. Love, Thermomechanical analysis and durability of commercial micro-porous polymer Li-ion battery separators, Journal of Power Sources, 196 (2011) 2905-2912.

39. S. Yan, X. Xiao, X. Huang, X. Li, Y. Qi, Unveiling the environment-dependent mechanical properties of porous polypropylene separators, Polymer, 55 (2014) 6282-6292.

40. S. Yan, Y. He, A. Asta, J. Deng, C. Bae, X. Xiao, Characterization of the In-plane Orthotropic Viscoelastic Property of a Polymeric Battery Separator, Polymer Testing, 72, 46-54, 2018.

41. X. Zhang, Mechanical Behavior of Shell Casing and Separator of Lithium-ion Battery (Doctoral dissertation), Massachusetts Institute of Technology, 2017.

42. MAT_224 User Guide, LS-DYNA® Aerospace Working Group, 2015.

43. R. Goldberg, private communication.

CHAPTER 3 IN-PLANE ORTHOTROPIC PROPERTY CHARACTERIZATION

3.1 Introduction

This Chapter presents the development of experimental methods for the characterization of the in-plane orthotropic property of polymer separator Celgard® 2400. The experiments were performed with a dynamic mechanical analyzer (DMA). The measurements included the stress-strain curves in the MD, TD and shear under three loading rates, the major and minor Poisson's ratios, and the creep responses in the MD, TD and shear. Digital image correlation (DIC) was used for strain measurements. The shear property was measured with an off-axis tensile experiment. Based on the analogy for anisotropy between the elastic and linear viscoelastic domains, the shear creep response was measured with the off-axis tensile creep experiments. The relationships for the elastic orthotropic solid such as the symmetry condition and the relation between the shear modulus and the off-axis modulus were also examined.

3.2 Experimental

3.2.1 Material

A representative separator Celgard® 2400 was investigated in this work. Celgard® 2400 is a monolayer PP porous film with a nominal thickness of 25μm. Its surface microstructure is shown in Fig. 1.2. Specimens in the form of long strips were cut from a 93 mm wide separtor roll using a razor blade. Figure 3.1 shows the orientation of the MD, TD and 45°off-axis specimens. The nominal dimensions of the specimen were 45 mm in length and 5 mm in width.

For an orthotropic solid, the two in-plane material directions are defined as 1 and 2 directions. In later discussions, the MD and TD are also referred to as 1 and 2 directions, respectively.

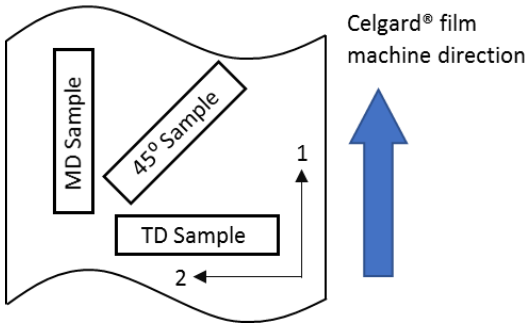

Figure 3.1 The MD, TD, and 45° off-axis samples.

3.2.2 Loading

All experiments were performed with a TA 2980 DMA under tensile mode. The DMA measures the mechanical properties of materials as a function of time, temperature, and frequency. It is widely used in viscoelastic characterization of polymers.

Two types of experiment were performed. The tensile stress-strain curves were measured at three loading rates at 0.1, 1, 10N/min. The viscoelastic properties were measured in tensile creep mode. The experimental set-up was the same for both experiments. Figure 3.2 shows a specimen mounted in the DMA tensile clamp. The test legnth of the specimen was about 15 mm. All measurements were conducted at the ambient temperature.

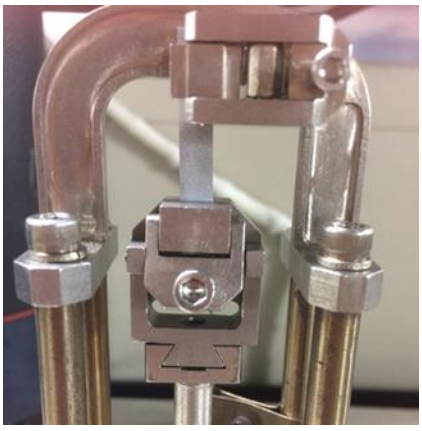

Figure 3.2 A sample in tensile clamp.

3.2.3 Strain Measurement

The measurement of the Poisson's ratio and shear properties requires measuring strains in other orientations in addition to the longitudinal direction. The DIC technique was used in these measurements. DIC is a noncontact, full field experimental technique. In this method, the surface of the specimen is covered by random speckle patterns. Successive images are taken before and during the deformation of the specimen. Through correlating successive images, the movement and relative locations of the random speckles are tracked and the displacement and strain fields are computed.

A Stingray F-201B monochrome CCD camera together with an Edmund™ Optics telecentric lens (primary magnification 0.75X, 120 mm working distance) was used in imaging, as shown in Fig. 3.3a. The telecentric lens allows the camera to focus on a small viewing area from a sufficiently large distance, which reduces the errors due to the out-of-plane displacement and lens distortion.

The resolution of the camera was 1024pixel×768 pixel. The field of view in the measurement was 5.9mm×4.4mm, which gave a resolution of 5.7μm×5.7μm/pixel. Each pixel covered about 10 microscopic features shown in Fig. 1.2. Therefore, the DIC results represented the macroscopic behavior of the separator.

The speckle pattern was created by spraying black paint directly onto the separator surface using an air brush with a nozzel size of 0.35mm. Figure 3.3b shows a typical speckle pattern used in this work. The speckle size was about 8pixels×8pixels on average, corrsponding to an area of 46μm×46μm.

The image acquisition of the CCD camera was controlled by a computer with the Allied Vision® AcquireControl software. The image was taken every second for MD and TD samples and 0.25 second for 45º samples. The relationship between the DIC and the DMA outputs was established in post-processing according to the time elapsed from the starting point.

GOM Correlate-2D software was used to analyze the results. The strain was determined using the virtual extensometers defined at the surface of the specimen. The DIC resolution was estimated as 0.004% strain using two images taken without loading the sample.

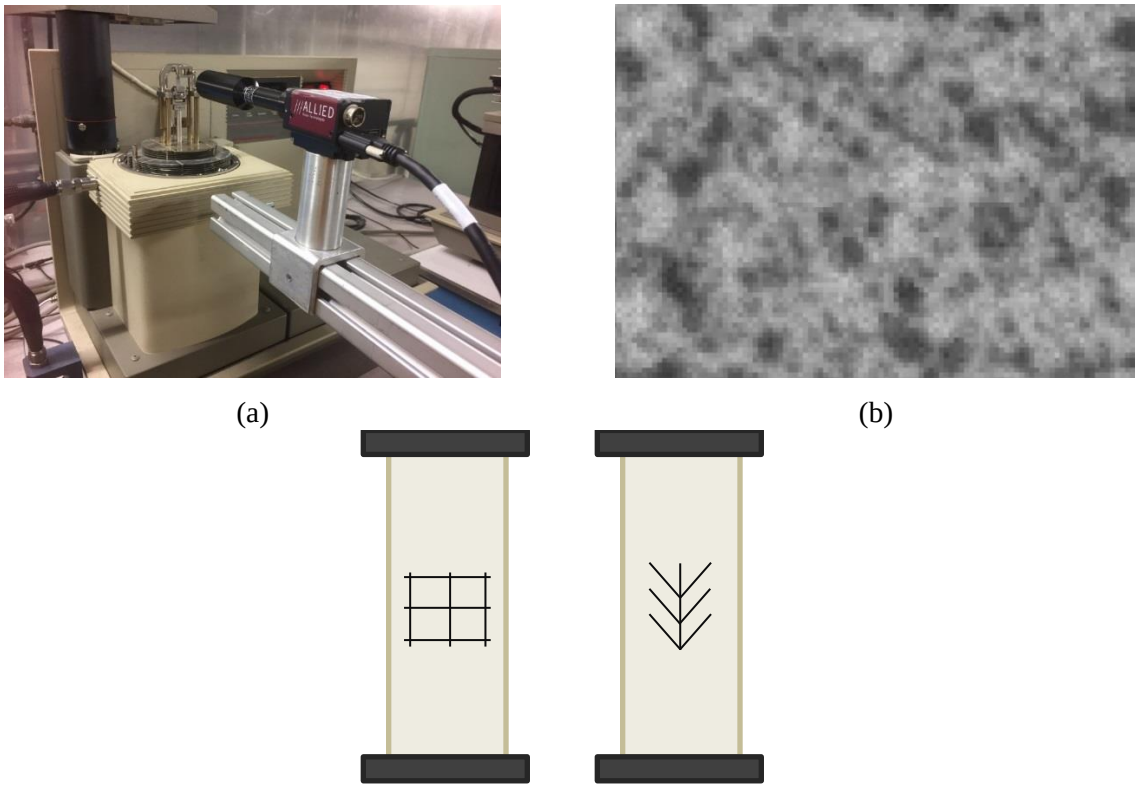

Figure 3.3 (a) The digital image correlation (DIC) measurement set-up. (b) A typical speckle pattern. (c) Three sets of virtual extensometer used in the DIC analysis for on-axis and off-axis tensile experiments.

For each experiment, three sets of virtual extensometer were used in DIC analysis. Figure 3.3c depicts the three sets of 0º/90º extensometer for analysis of the MD and TD specimens and

the 0º/45º/90º extensometer for the 45º specimen. The strain in a given orientation reported below was the averaged value from three extensometers.

To investigate whether the speckles would influence the deformation behavior of thin film specimens, the longitudinal modulus was determined from the strain measured with the DMA using the MD and TD specimens with and without speckles. The results are compared in Table 3.1. The difference between the specimens with and without speckles was within the experimental scatter.

Table 3.1 The longitudinal modulus of the MD and TD samples with and without speckles at a force ramp rate 0.1N/min

	Without speckles	With speckles	Difference
MD (MPa)	955±31	975±57	2.1%
TD (MPa)	485±17	485±36	0%

3.3 Results and Discussion

3.3.1 Tensile Behavior

3.3.1.1 Stress-Strain Curves

Figure 3.4 presents typical uniaxial tensile stress-strain curves measured with the MD, TD, and 45º specimens at ramp rates of 0.1, 1 and 10N/min. Repetitions were performed for each test condition as shown in Fig. A.1 in Appendix A.

The elastic modulus was determined using the initial linear portion of the stress-train curve as per ASTM D882 [1]. The shear modulus was determined from the 45º off-axis measurement. The details are presented in 3.3.1.3.

The rate dependence of the elastic modulus was observed in the MD, TD and shear. The trend of the rate dependence was the same for three orientations but their magnitude differed. Table 3.2 compares the rate dependence of the modulus in three directions. The trend is MD>shear>TD.

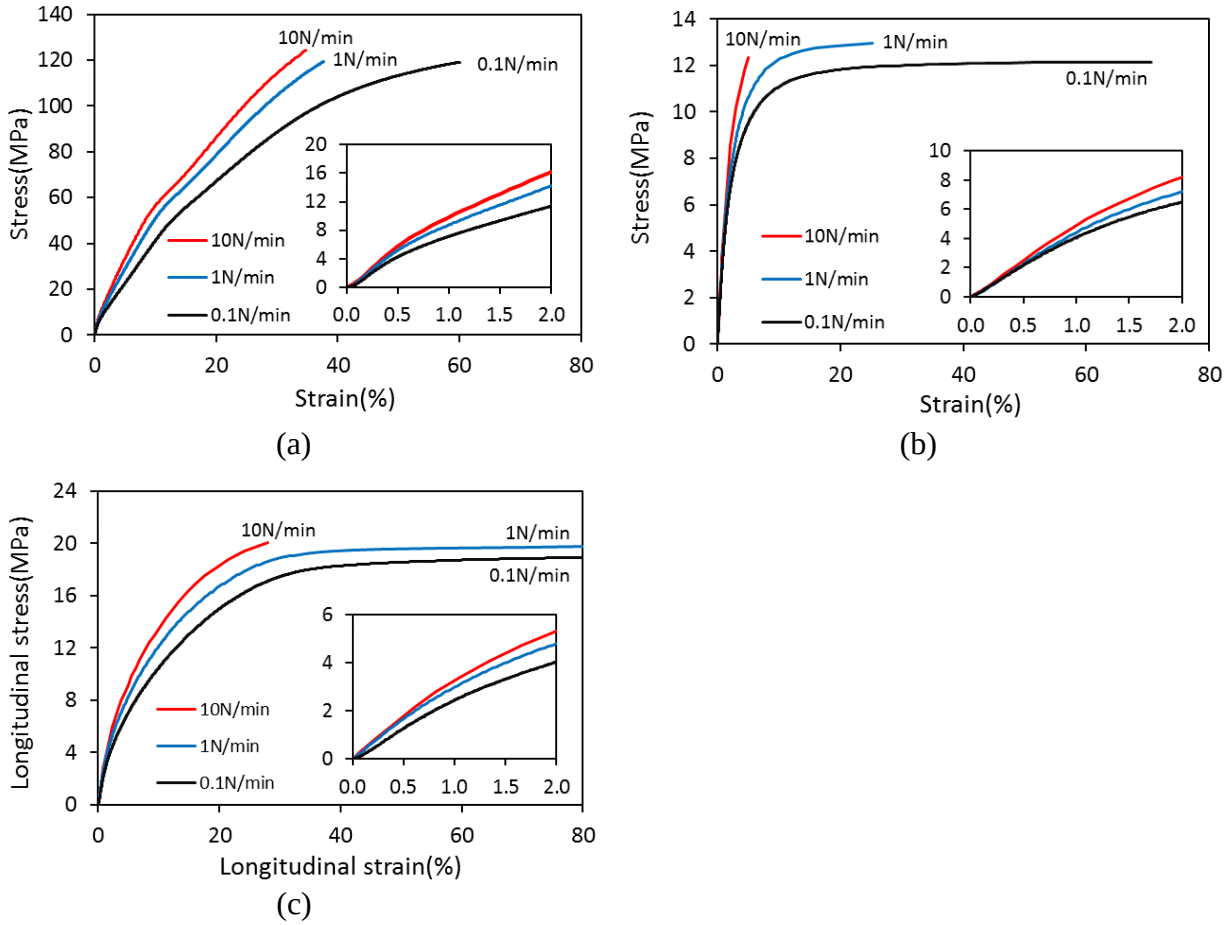

Figure 3.4 The stress-strain curves at different force ramp rates measured with (a) the MD, (b) the TD and (c) the 45º specimens.

Table 3.2 Measured elastic modulus for the MD, TD and 45º sample in the range of 0.1-0.5% strain at three rates and their ratio to 0.1N/min

Ramp rate (N/min)	MD Modulus (MPa)		TD Modulus (MPa)		45º Longitudinal Modulus (MPa)		Shear Modulus (MPa)	
		Ratio		Ratio		Ratio		Ratio
0.1	955±31	1.00	485±17	1.00	290±10	1.00	90±4	1.00
1	1134±23	1.19	510±18	1.05	323±27	1.11	101±11	1.12

Table 3.2(cont'd)

10	1282±9	1.34	526±1	1.08	351±6	1.21	110±3	1.22

3.3.1.2 Poisson's Ratio

For the plane stress condition, the in-plane compliance matrix is given by

$$\begin{bmatrix} J_{11} & J_{12} & 0 \\ J_{21} & J_{22} & 0 \\ 0 & 0 & J_{66} \end{bmatrix} \tag{3.1}$$

where $J_{11} = \frac{1}{E_{11}}$, $J_{22} = \frac{1}{E_{22}}$, $J_{12} = -\frac{v_{21}}{E_{22}}$, $J_{21} = -\frac{v_{12}}{E_{11}}$, $J_{66} = \frac{1}{G_{12}}$, v_{12} and v_{21} are the major and minor Poisson's ratios; E_{11} and E_{22} are the modulus in the 1st and 2nd material directions, and G_{12} is the in-plane shear modulus.

v_{12} and v_{21} were measured in tensile experiments at 0.1N/min with the MD and TD specimens, respectively. The longitudinal and transverse strains for each specimen were measured by three sets of DIC 0º/90º virtual extensometers covering an area of 4×4mm. Figure 3.5a plots the typical longitudinal vs. transverse strain curves for the MD and TD specimens. The repeated tests are shown in Fig. A.2 in Appendix A. The slope of the curve yields the Poisson's ratio. v_{12} and v_{21} determined in this way are shown in Fig. 3.5b. Over the strain range of 0.1 to 5%, v_{12} remained at a constant value of 0.17 whereas v_{21} increased with strain. The averaged v_{21} can be fit by a linear equation $v_{21}=0.0354\varepsilon_{longitudinal}+0.0801$. Table 3.3 summarizes these results.

For orthotropic materials, the components in the compliance matrix in Eq. 3.1 is subjected to a symmetry constrain such that $J_{12}=J_{21}$. Hence we have

$$\nu_{21} = \nu_{12}\frac{E_{22}}{E_{11}} \tag{3.2}$$

The validity of Eq. 3.2 was examined by comparing the measured and computed v_{21} values in Fig. 3.5c. The results indicate that the symmetry condition $J_{12}=J_{21}$ is valid up to 1% longitudinal strain in the TD direction. The reason that symmetry condition does not satisfied after 1% longitudinal strain in the TD direction may be different yielding point along MD and TD.

In Fig. 3.5c, the calculated v_{21} was obtained with $v_{12}=0.17$ and the instantaneous MD and TD moduli. The determination of the instantaneous MD and TD moduli is provided in the Appendix B.

It should be noted that the separator investigated here is very different from that reported in [2] where a PP separator with $E_{MD}=1114$ MPa and $E_{TD}=180$MPa was examined for its wrinkling in TD, a phenomenon observed in highly orthotropic PP separator at large strains.

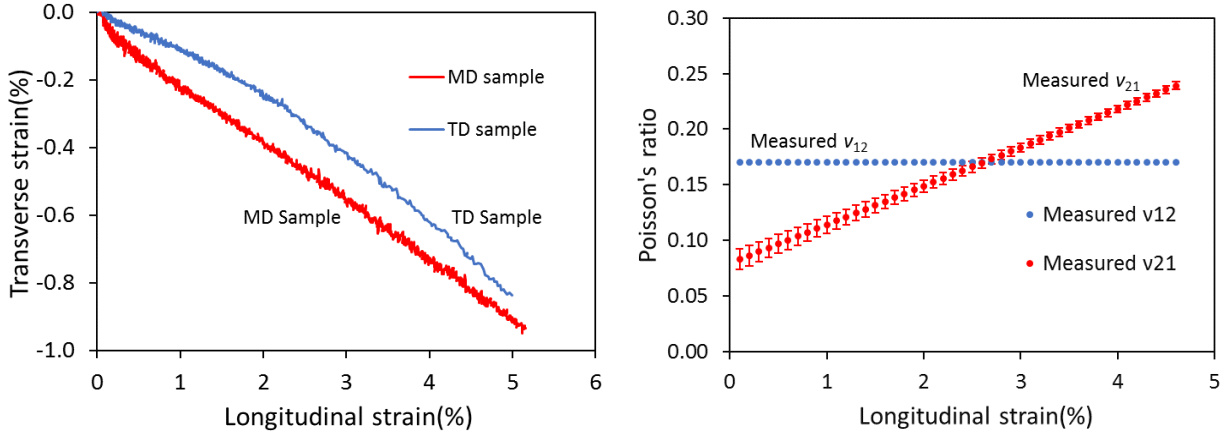

(a) (b)

Figure 3.5 (a) The typical transverse vs. longitudinal strain curves measured under uniaxial tensile loading of the MD and TD specimens. (b) The major and minor Poisson's ratio ν_{12} and ν_{21} (c) Comparison of the measured and calculated ν_{21}.

Figure 3.5(cont'd)

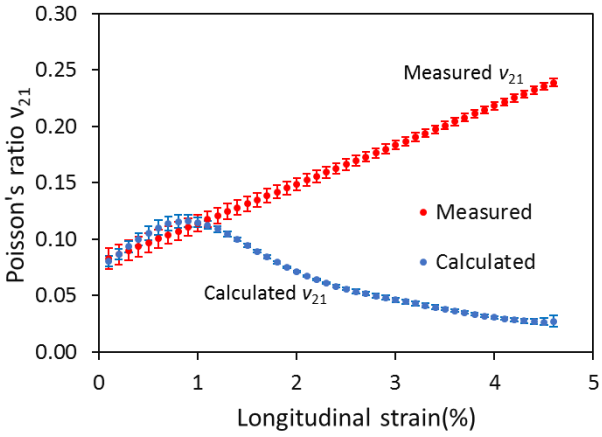

(c)

Table 3.3 Measured Poisson's ratios in the strain range 0.1-5%

Major Poisson's ratio v_{12}	0.17
Minor Poisson's ratio v_{21}	$0.0354\varepsilon_{\text{longitudinal}}+0.0801$

3.3.1.3 Shear Stress-Strain Curve

Figure 3.6 illustrates the off-axis tensile experiment for the shear property measurement of an orthotropic material. For a specimen loaded under uniaxial tension, a biaxial stress state arises at any off-axis angle to its axial direction. In the analysis, the off-axis angle θ is defined as the angle between the longitudinal (loading) direction and the 1st principal material direction. The shear stress in the material coordinate τ_{12} is related to the longitudinal stress σ by [3,4]

$$\tau_{12} = -\sigma sin\,\theta\, cos\,\theta \tag{3.3}$$

The shear strain in the material coordinate can be determined from the strains measured in three different orientations. In this work, the DIC 0º/45º/90º virtual extensometers were employed. The shear strain was determined by [5]

$$\gamma_{12} = 2\varepsilon_{45^\circ} - (\varepsilon_{0^0} + \varepsilon_{90^0}) \tag{3.4}$$

where ε_0, ε_{90} are the strains measured by the virtual extensometers orientated at the MD and TD, and ε_{45° is the strain measured by the virtual extensometer oriented at 45º to the MD. The shear stress-strain curve can be determined from the off-axis tension tests according to Eqs. 3.3 and 3.4.

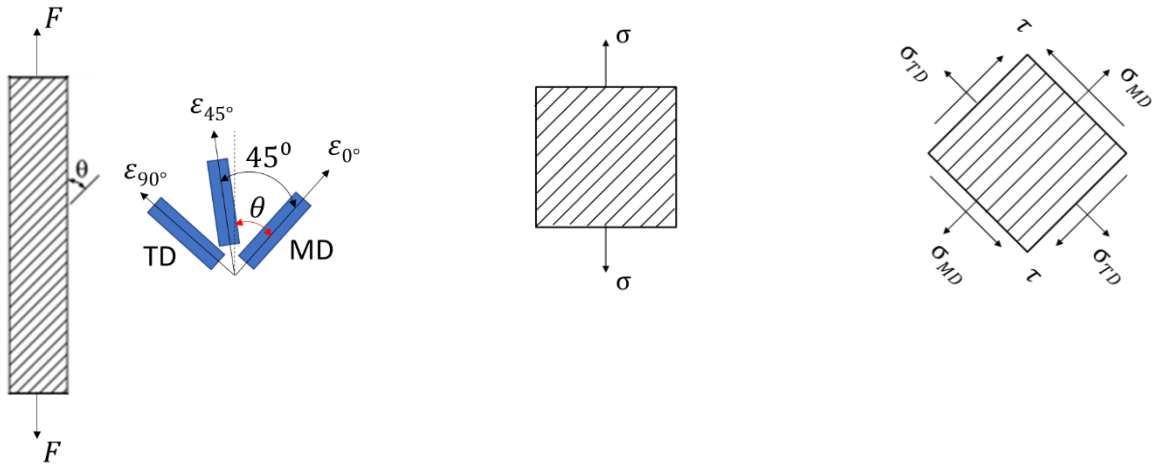

(a) (b) (c)

Figure 3.6 The off-axis tensile experiment for an orthotropic specimen. (a) The orientation of the 0/45º/90º virtual extensometers. (b) The longitudinal stress. (c) The stress components in the material coordinate system.

The off-axis tensile experiments were performed with 45º specimens under a force ramp rate of 0.1N/min. In off-axis tensile experiments, it is important to ensure that the contribution of the shear component is predominant over the normal strain components. Figure 3.7a present the measured ε_{0°, ε_{90°, and ε_{45°. The results from three sets of DIC 0/45º/90º virtual extensometers are presented. The strains from the three sets were very close, indicating the uniformity of the strain field across the specimen. The measured MD and TD strains were much smaller than the shear strains. The result confirms that the biaxial strain field in the material coordinate produced by the 45º off-axis tensile experiment is predominately in shear and, therefore, it is well suited for measuring the shear property of the separator. Figure 3.7b presents a typical shear stress-strain

curve. The repeated test is shown in Fig. A.3 in Appendix A. The shear modulus was determined as 102MPa over the strain region of 0.1-0.5%.

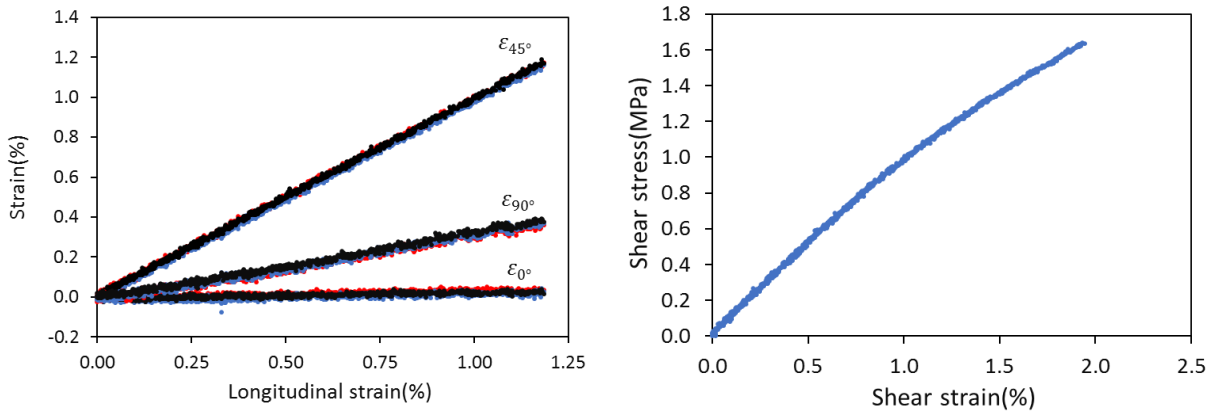

(a) (b)

Figure 3.7 (a) Strains from three sets of DIC extensometers in a 45º off-axis tension experiment. (b) The shear stress-strain curves determined by off-axis tension experiments.

The shear modulus can also be computed from the longitudinal modulus E_θ of the off-axis specimen and the elastic constants in the material directions from the following relationship derived through stress and strain transformation [3,4]

$$\frac{1}{G_{12}} = \left(\frac{1}{E_\theta} - \frac{cos^4\,\theta}{E_{11}} - \frac{sin^4\,\theta}{E_{22}}\right) / \left(sin^2\,\theta\, cos^2\,\theta\right) + \frac{2\nu_{12}}{E_{11}} \tag{3.5}$$

Table 3.4 compares the shear modulus values obtained by these two methods. The shear modulus determined from Eq. 3.5 was 101MPa. This value compared well with 102MPa determined from the DIC strain measurement. This indicates again that the separator follows the orthotropic framework.

Data on the shear modulus of battery separators is scarce in literature. A shear modulus of 44MPa was reported for a PP separator of 20μm thickness with E_{MD}=1114 MPa and E_{TD}=180MPa [2] but there were no details about the test method. A lower E_{TD}/E_{MD} ratio could lead to a lower shear modulus of the material.

Table 3.4 Shear modulus determined by the off-axis tension experiment using Eq. 3.5 and DIC strain measurement

Off-axis angle	Measured Longitudinal Modulus E_θ (MPa) (0.1-0.5% strain)	Shear modulus calculated with Eq. 3.5 (MPa)	Shear modulus measured with DIC strains (MPa) (0.1-0.5% shear strain)
45º	323±3	101±1	102±1

3.3.2 Viscoelastic Characterization

3.3.2.1 Creep Compliance

The viscoelastic characterization was performed in creep mode for the MD, TD and 45º specimens. To determine the linear viscoelastic range, the creep tests were performed under different stress levels. The creep duration was 20 minutes. A fresh sample was used at each stress level.

Figure 3.8a through 3.8c presents the typical creep strain $\varepsilon(t)$ and the creep compliance determined by $J(t)= \varepsilon(t)/\sigma$ at different stress levels for the MD, TD and 45º. The repeated tests are shown in Fig. A.4 in Appendix A. In the linear viscoelastic range, the measured compliance would be independent of the stress level. Judging with this criterion, the linear range was up to 5MPa for the MD, 2MPa for the TD, and 1.5MPa for the 45º orientation.

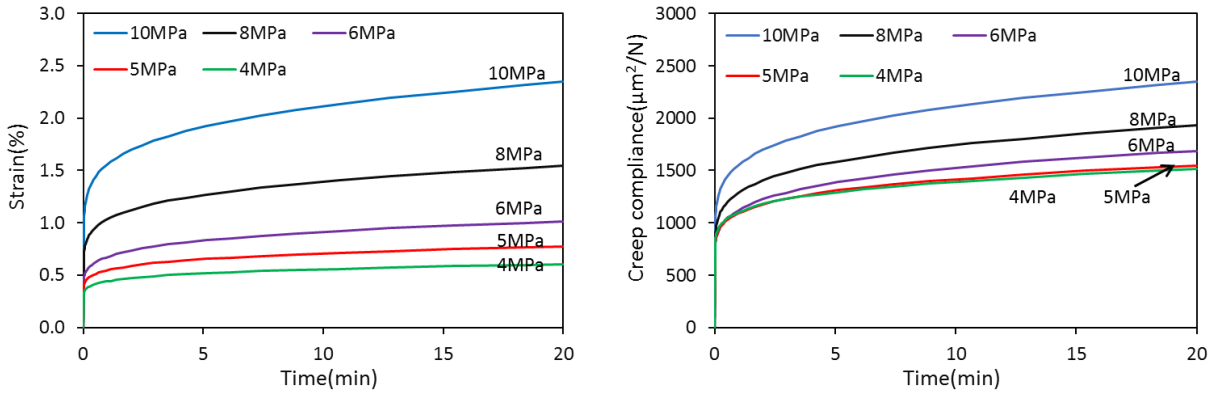

(a)

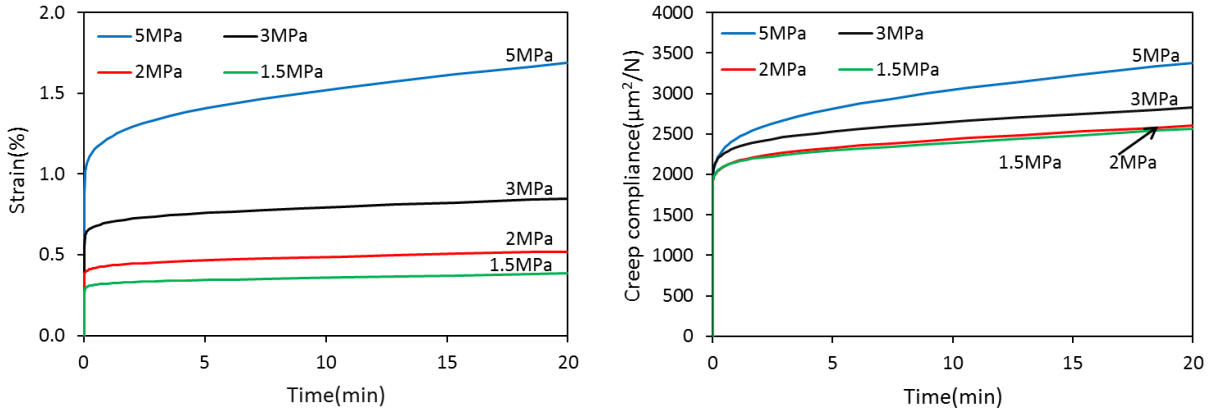

(b)

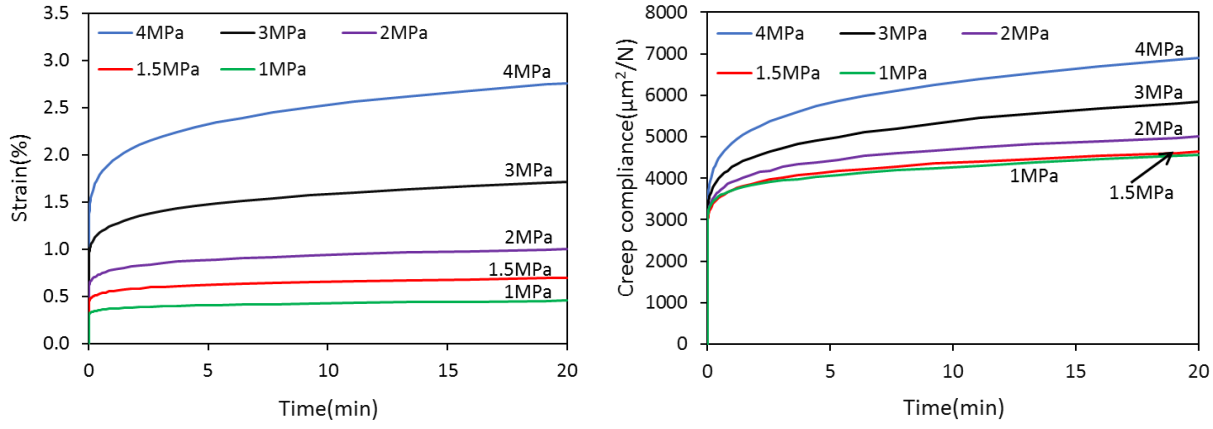

(c)

Figure 3.8 The creep strains (left) and creep compliances (right) measured under different stress levels, (a) the MD, (b) the TD, (c) the 45°, and (d) the shear calculated based on 45° sample at 1.5MPa.

Figure 3.8(cont'd)

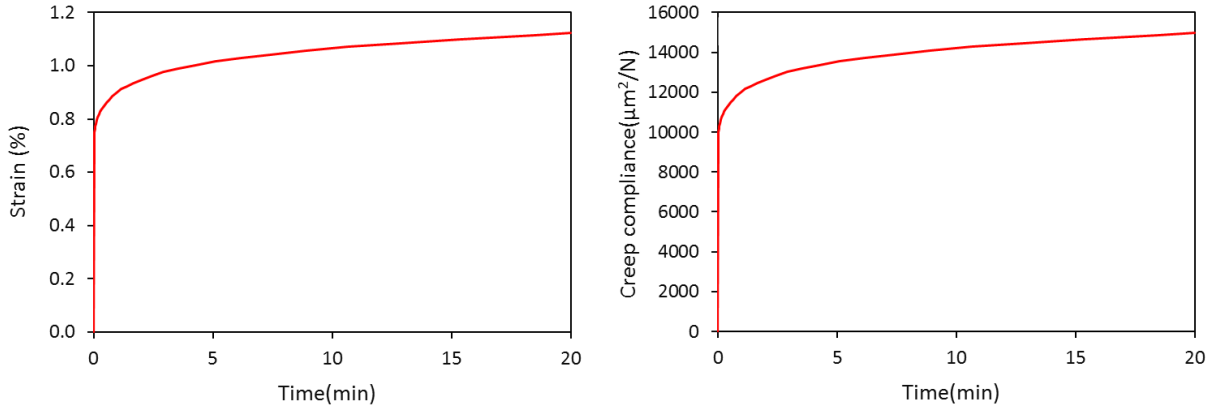

(d)

Assuming that the anisotropy in the linear viscoelastic domain is analogous to that in the elastic domain, Eq. 3.5 can be extended to the viscoelastic domain. For the compliance, it is written as

$$J_{66}(t) = \left(J_{\theta}(t) - m^4 J_{11}(t) - n^4 J_{22}(t) - 2m^2 n^2 J_{12}(t)\right)/(m^2 n^2) \tag{3.6}$$

where m=cos θ, n=sin θ. J_{66}(t) was determined using Eq. 3.6.

In viscoelastic models, the creep compliance is often represented by a Prony series [6]. In this work, the linear compliances were fitted with a five-term Prony series

$$J(t) = J_0 + \sum_{i=1}^{5} J_i \left(1 - exp\left(-\frac{t}{\beta_i}\right)\right) \tag{3.7}$$

where J_i were creep constants and β_i were retardation times. J_i were fitted using the same non-linear least-square technique as in [7,8] and the results are summarized in Table 3.5. The fitted creep compliances are shown in Fig. 3.9. The Prony series fit the experimental data very well. The data points in Fig. 3.9 were the average of three experiments. The scatter is shown by the error bars.

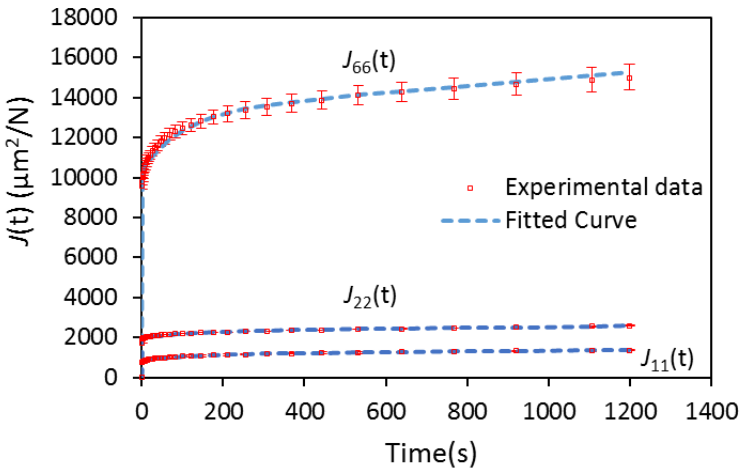

Figure 3.9 The creep compliances given by Prony series and the experimental data.

Table 3.5 Prony series parameters for the creep compliances

Creep constants (μm²/N)	MD J_{11}(t)	TD J_{22}(t)	Shear J_{66}(t)	Retardation time β_i (s)	
J_0	28	66	152	-	-
J_1	783	1890	10159	τ_1	0.1
J_2	325	308	2886	τ_2	100
J_3	59	61	26	τ_3	1000
J_4	1712	2408	17942	τ_4	10000
J_5	0.0134	23	21	τ_5	100000

3.3.2.2 Relaxation Modulus

The Relaxation modulus can be obtained from the creep compliance mathematically in the Laplace domain using Eq. 3.8 [7]

$$G(s)J(s) = \frac{1}{s^2} \tag{3.8}$$

The relaxation constants and times obtained by the Laplace transformation are summarized in Table 3.6. The G_{11}(t), G_{22}(t) and G_{66}(t) curves are compared in Fig. 3.10. The relaxation was

larger in the MD than in the TD and shear. As shown in Fig. 1.2, the amorphous fibers were major force carrier along MD while semi-crystalline region were major force carrier along the TD. The microstructure determines the difference in their viscoelastic responses.

Table 3.6 Prony series parameters for the relaxation modulus obtained by Laplace Transformation

MD $G_{11}(t)$		TD $G_{22}(t)$		Shear $G_{66}(t)$	
Stress relaxation constant(N/m^2)	Relaxation time(s)	Stress relaxation constant(N/m^2)	Relaxation time(s)	Stress relaxation constant(N/m^2)	Relaxation time(s)
G_∞=3.44x10^8	-	G_∞=2.10x10^8	-	G_∞= 3.21x10^7	-
G_1=3.42x10^{10}	τ_1=0.00348	G_1=1.46x10^{10}	τ_1=0.00339	G_1=6.48x10^9	τ_1=0.00148
G_2=3.62x10^8	τ_2=70.9895	G_2=7.10x10^7	τ_2=86.2649	G_2=2.16x10^7	τ_2=77.9138
G_3=5.57x10^7	τ_3=943.788	G_3=1.41x10^7	τ_3=971.119	G_3=1.94x10^5	τ_3=997.765
G_4=4.70x10^8	τ_4=4165.36	G_4=2.15x10^8	τ_4=4933.96	G_4=4.30x10^7	τ_4=4257.08
G_5=1.40x10^3	τ_5=100000	G_5=8.99x10^5	τ_5=99550	G_5=1.92x10^4	τ_5=99936

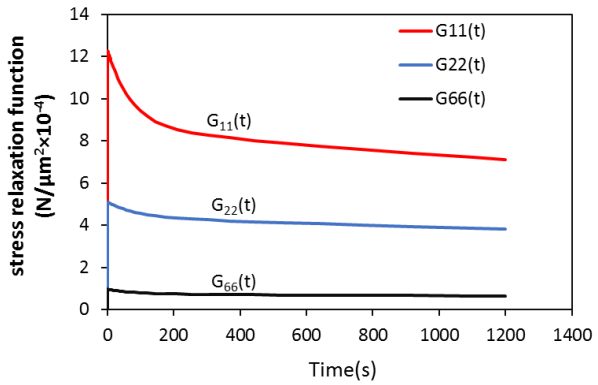

Figure 3.10 Relaxation modulus $G_{11}(t)$, $G_{22}(t)$ and $G_{66}(t)$ obtained through Laplace transformation.

3.4 Conclusions

The in-plane orthotropic elastic and viscoelastic characterization was performed for a PP battery separator of 25μm thickness using a dynamic mechanical analyzer (DMA). The shear properties were measured in uniaxial tension with specimens cut at an off-axis angle. The digital image correlation (DIC) technique was used in the strain measurements for the Poisson's ratio and the shear modulus.

The stress-strain curves for the MD, TD and shear were measured at three loading rates, 0.1N/min, 1N/min and 10N/min. The elastic modulus increased within this range as much as 34% in the MD, 22% in shear and 8% in the TD.

In the range of 0.1 to 5% strain, the measured major Poisson's ratio was a constant value of 0.17. The minor Poisson's ratio increased linearly with strain. The major and minor Poisson's ratios were found to follow the elastic symmetry relationship up to 1% longitudinal strain in TD.

The shear modulus was 102MPa and 101MPa determined from the DIC strain and from the off-axis modulus and the elastic constants, respectively. The close agreement between the two methods indicates that the separator follows the orthotropic elastic framework.

The viscoelastic characterization was performed in creep mode for the MD, TD and 45^{o} off-axis specimens. The linear viscoelastic range was determined. The creep compliance in the MD, TD and shear directions were determined. The results were fitted by a Prony series. From the creep function, the Prony series for relaxed modulus was obtained mathematically through Laplace transformation.

The orthotropic characterization performed here laid the foundation for the development of orthotropic elastic and viscoelastic models for battery separators.

APPENDICES

APPENDIX A Repeated uniaxial tests, Poisson's ratio measurements, shear modulus measurements and creep tests at room temperature

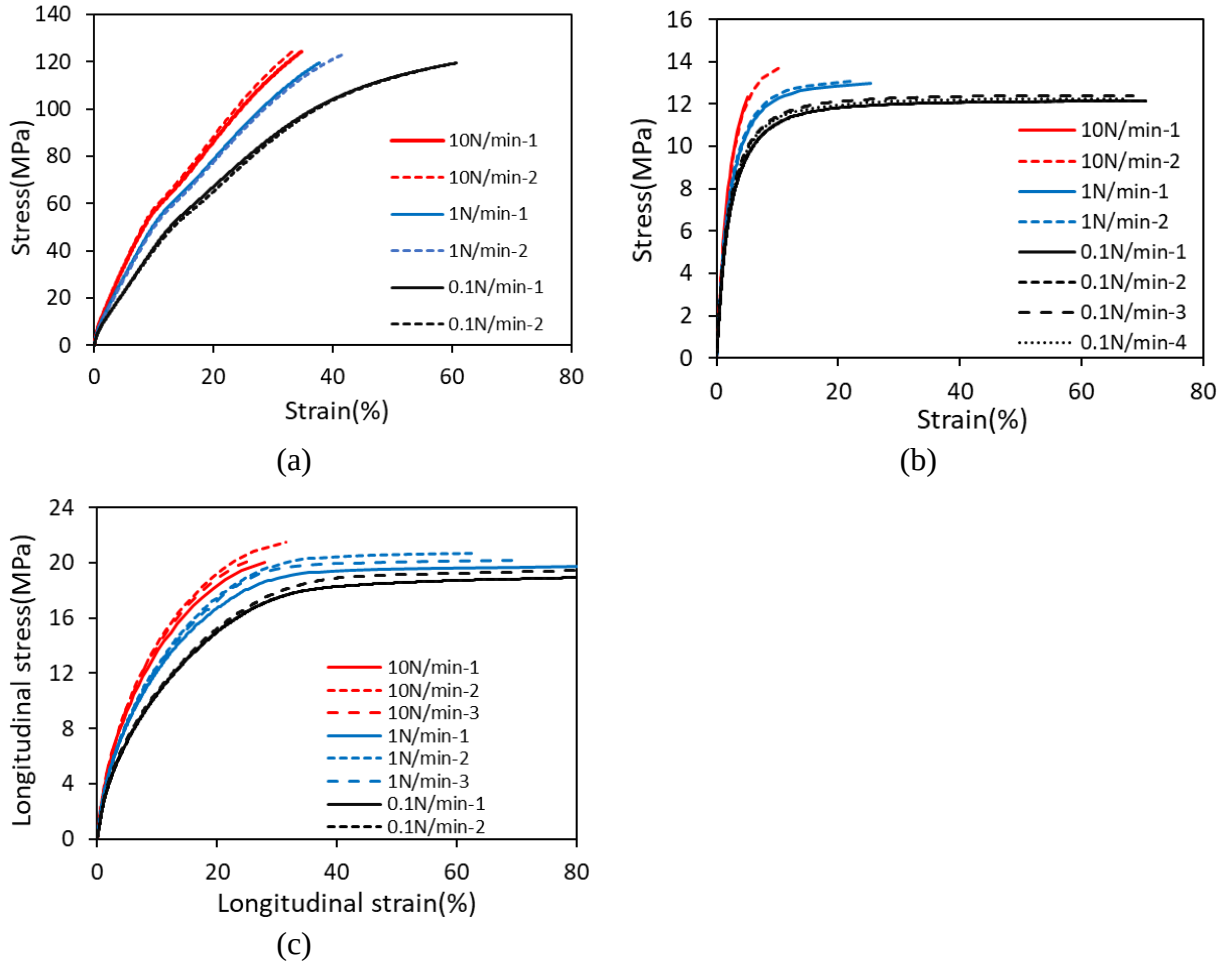

Figure A.1 The stress-strain curves at different force ramp rates measured with (a) the MD, (b) the TD and (c) the 45º specimens.

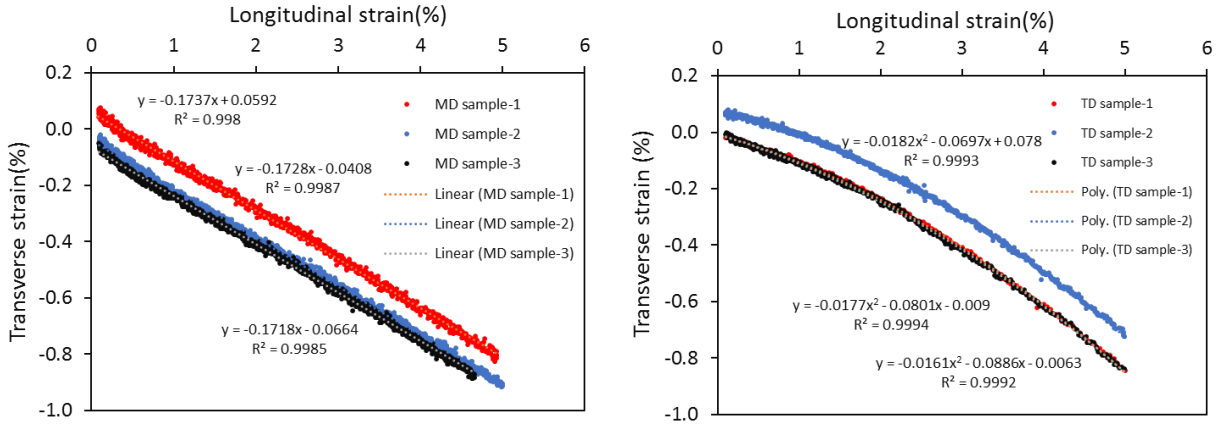

(a) (b)

Figure A.2 The typical transverse vs. longitudinal strain curves measured under uniaxial tensile loading of (a) the MD specimens, (b) the TD specimens.

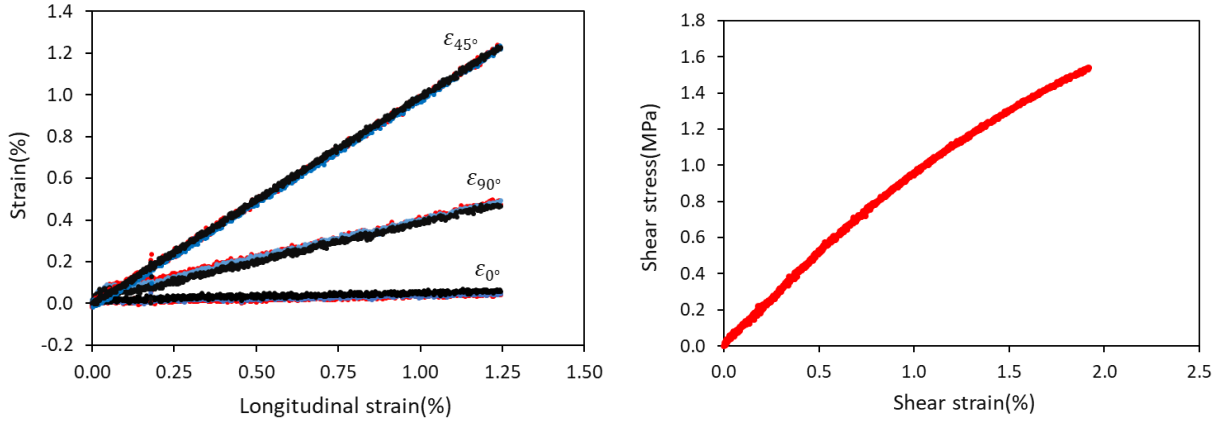

(a) (b)

Figure A.3 (a) Strains from three sets of DIC extensometers in a 45º off-axis tension experiment in repeated test. (b) The shear stress-strain curves determined by off-axis tension experiments.

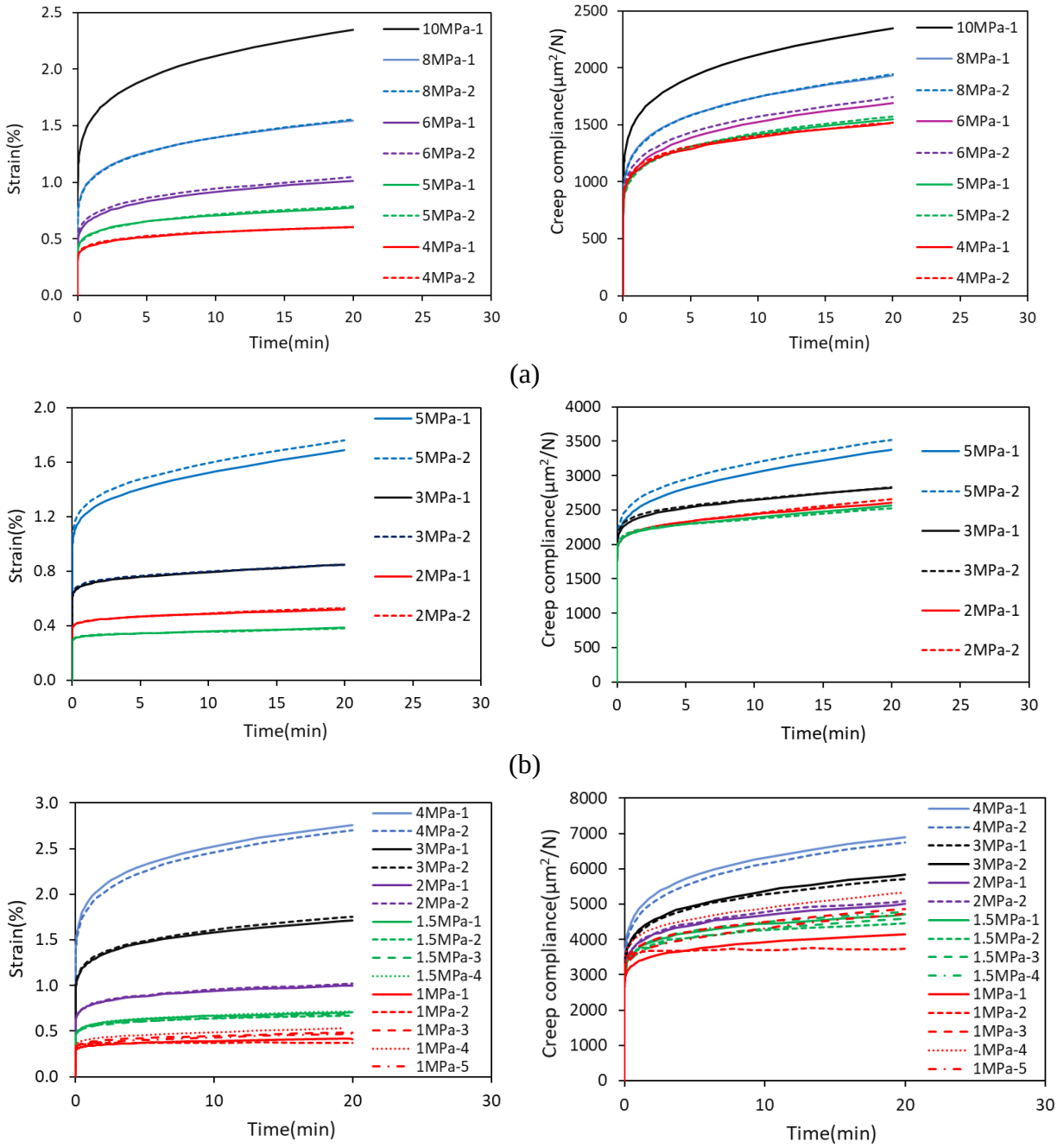

Figure A.4 The creep strains (left) and creep compliances (right) measured under different stress levels, (a) the MD, (b) the TD, (c) the 45°.

APPENDIX B Determination of the Instantaneous MD and TD Moduli

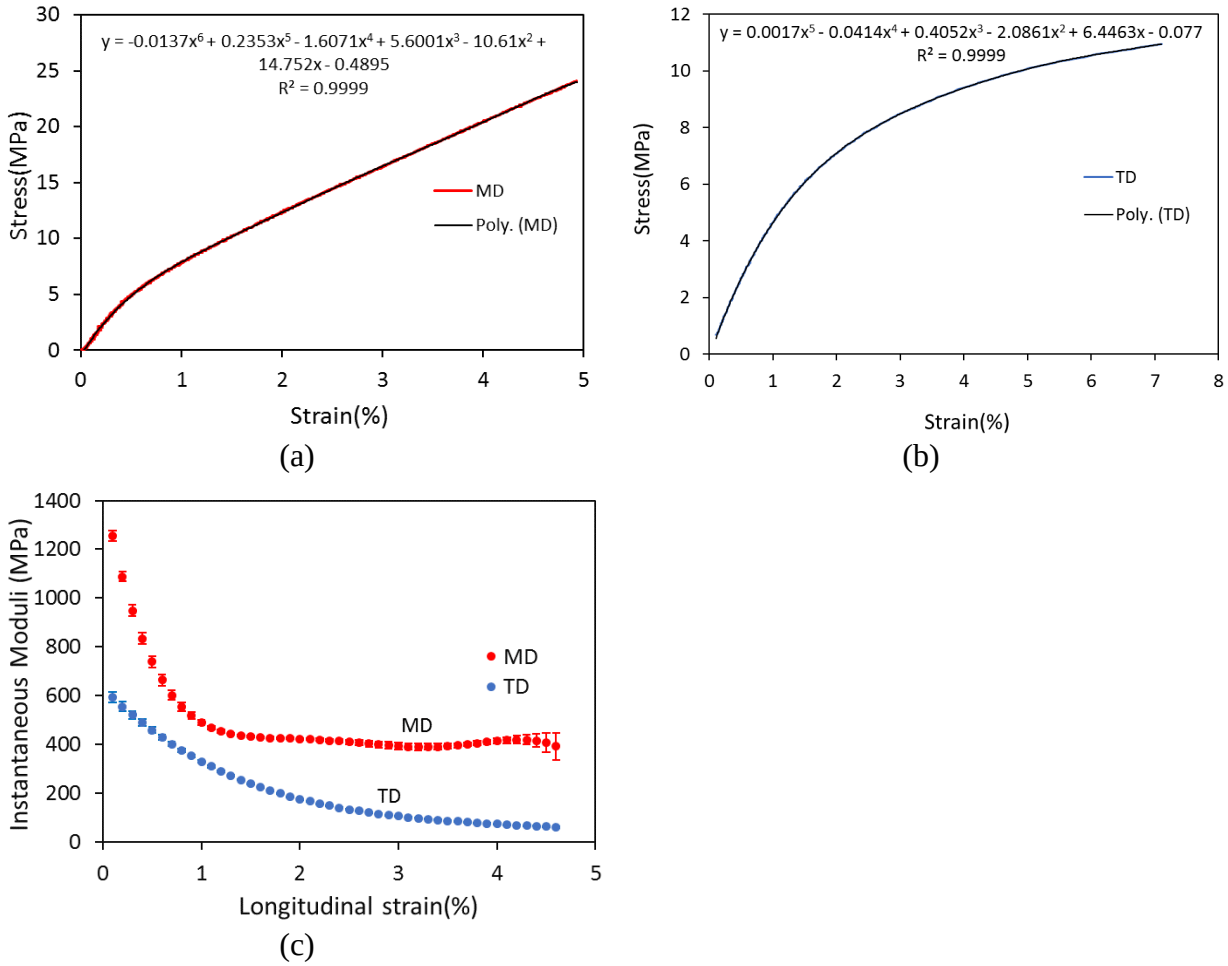

Figure B.1 (a) Polynomial fitting of the stress-strain curves for the MD sample (b) Polynomial fitting of the stress-strain curves for the TD sample (c) The instantaneous MD and TD moduli calculated from the derivative of the polynomial fitting of the stress-strain curves.

REFERENCES

REFERENCES

1. ASTM Standard D882, Standard Test Method for Tensile Properties of Thin Plastic Sheeting, ASTM International, West Conshohocken, PA (2012).

2. J. Zhu, X. Zhang, T. Wierzbicki, Stretch-induced wrinkling of highly orthotropic thin films, International Journal of Solids and Structures, 139-140 (2018) 238-249.

3. M.J. Pindera, C.T. Herakovich, Shear Characterization of Unidirectional Composites with the Off-Axis Tension Test, Experimental Mechanics, 26 (1986) 103-112.

4. I.M. Daniel, O. Ishai, Engineering Mechanics of Composite Materials, Oxford University Press, New York (1994).

5. A. Shukla, J.W. Dally, Experimental Solid Mechanics, College House Enterprises, Knoxville, TN (2014).

6. I.M. Ward, J. Sweeney, An Introduction to the Mechanical Properties of Solid Polymers, John Wiley & Sons Ltd, West Sussex, England (2004).

7. A. Sheidaei, X. Xiao, X. Huang, J. Hitt, Mechanical behavior of a battery separator in electrolyte solutions, Journal of Power Sources, 196 (2011) 8728-8734.

8. W. Wu, A Multiphysics Model for the Stress Analysis of the Separator In a Lithium-Ion Battery(Doctoral dissertation), Michigan State University, 2013.

CHAPTER 4 MEASUREMENT OF THE THROUGH THICKNESS COMPRESSION

4.1 Introduction

This Chapter presents the development of a capacitance-based displacement set-up for the measurement of the through thickness direction (TTD) compression stress-strain behavior of the separator and the investigation of its interaction with the electrode. The experiments were performed for a stack of two layers of Celgard® 2400 separator, NMC cathode, and separator/NMC cathode/separator stack in both air and electrolyte solvent (i.e. submersed in dimethyl carbonate DMC) conditions. The iso-stress based rule of mixtures was examined which was used to compute the compressive stress-strain curve for the stack from that of the separator and NMC layer.

4.2 Experiment

4.2.1 Capacitance Based Displacement Measurement System

To measure the TTD displacement of thin films, a capacitance-based measurement set-up has been developed in house. Figure 4.1 presents the experimental set-up. The main component is a pair of parallel discs made of precision glass. The disc has a diameter of 50.8 mm, thickness of 6.35 mm and a surface flatness ½ wavelength (~0.3 μm) at its smooth side. The discs are used as the compression platens for mechanical loading and as the capacitor plates. The capacitor electrode covers a circular area of 24 mm diameter at the center of the discs. It is a thin layer of tungsten coating of 5 nm thickness created by plasma sputtering. The electrical connection to the electrode is via a 3 mm wide conductive path created by tungsten coating on the disc. In the assembly shown in Fig. 4.1c, the two paths on the two discs were oriented at opposite directions with no overlap. Evidently, they did not contribute to the capacitance.

To maintain the parallelism of the glass discs, three small circular shaped samples will be tested simultaneously. This self-alignment method has been demonstrated in [1]. The samples will be placed between the two glass discs, outside the electrode measuring area and in equal spacing as shown in Fig. 4.1. The samples are 3 mm in diameter, having the same distance of 19 mm from the disc center. For easy sample positioning, three 3 mm×3 mm square marks have been created on the glass discs by plasma sputtering of a tungsten layer of 5 nm thickness.

The capacitance displacement measurement set-up will be used in air or in solvent conditions. The solvent used here is DMC, a common solvent in electrolyte for lithium-ion batteries. When testing in a solvent, the glass discs and sample assembly will be put into an Al container and the solvent will be added to submerse the assembly.

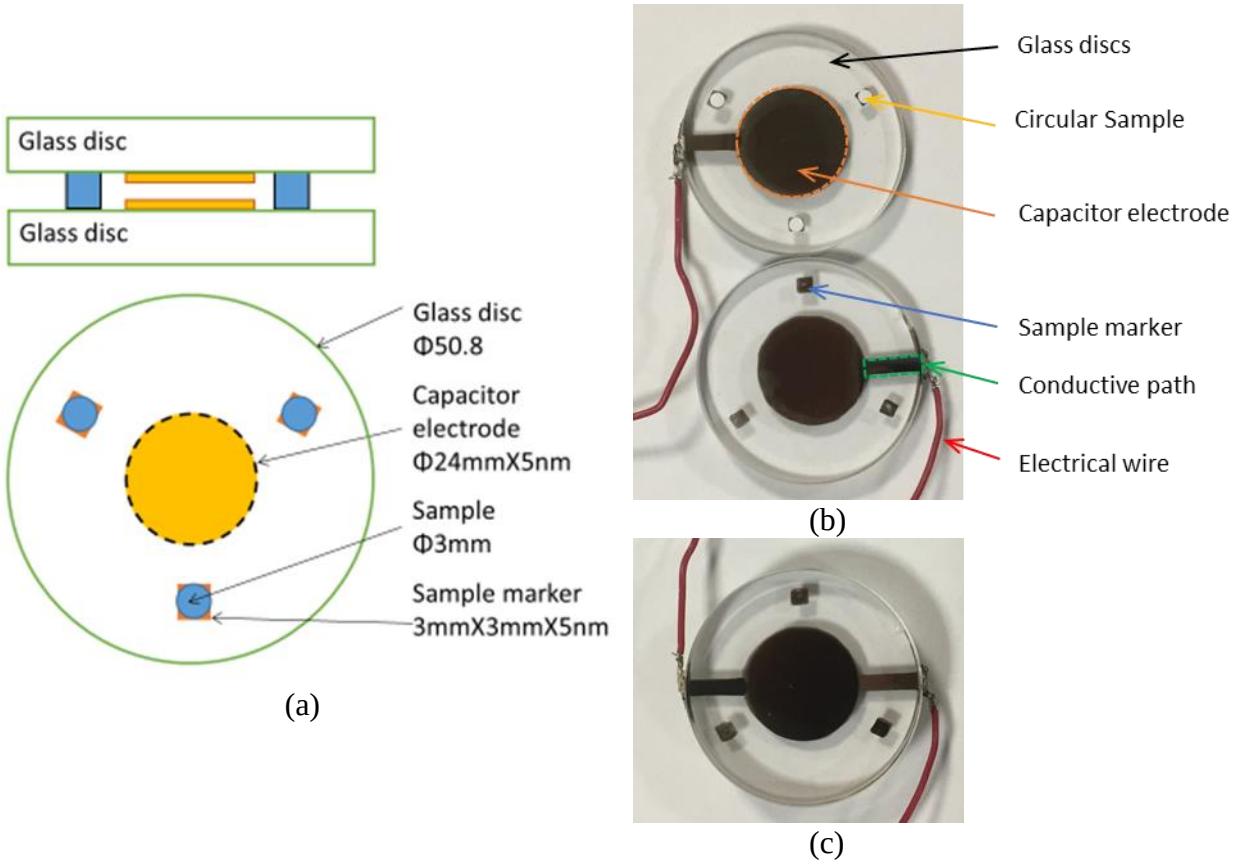

Figure 4.1 (a) Schematic plot of the capacitance based displacement measurement set-up. The glass discs with coated electrode and conductive path (b) before and (c) after assembly.

The capacitances were measured by a LCR meter Extech 380193. The applied AC voltage was 0.5 V with a frequency of 1 kHz. The capacitance data was recorded every 2 seconds through a built-in RS-232 interface with a data acquisition software. The accuracy of the capacitance measurement was ±0.1 pF.

For a parallel plate capacitor, the capacitance *C* depends on the distance between the two plates t_m

$$C = \frac{\varepsilon_0 \varepsilon_r A}{t_m} \tag{4.1}$$

where ε_0 is the permittivity in vacuum, ε_0=8.854x10^{-12} F/m; ε is the relative permittivity of the dielectric medium between the plate; and *A* is the area of the parallel plate capacitor. The value of ε in air is 1.00059 [2]. For DMC, the reported ε value was between 3.08 and 3.12 [3]. In the current work, ε=3.10 was used.

For the set-up in Fig. 4.1, ±0.1 pF corresponds to a displacement of ±0.015 μm to ±0.73 μm for a sample thickness ranging from 25 μm to 170 μm in air. In DMC, the resolution in displacement measurements is about three times higher.

4.2.2 Samples

Three types of samples have been tested. These are Celgard® 2400 separator, NMC cathode, and separator/cathode/separator stack.

Celgard® 2400 separator is a microporous polypropylene (PP) membrane with a nominal thickness of 25 μm. The NMC cathode used in this work is a double-side coated electrode on a 20 μm aluminum collector with a total nominal thickness of 110 μm. It was made in house. Fig. 4.2a

and 4.2b shows the surface images of the Celgard® 2400 separator and the NMC cathode, respectively.

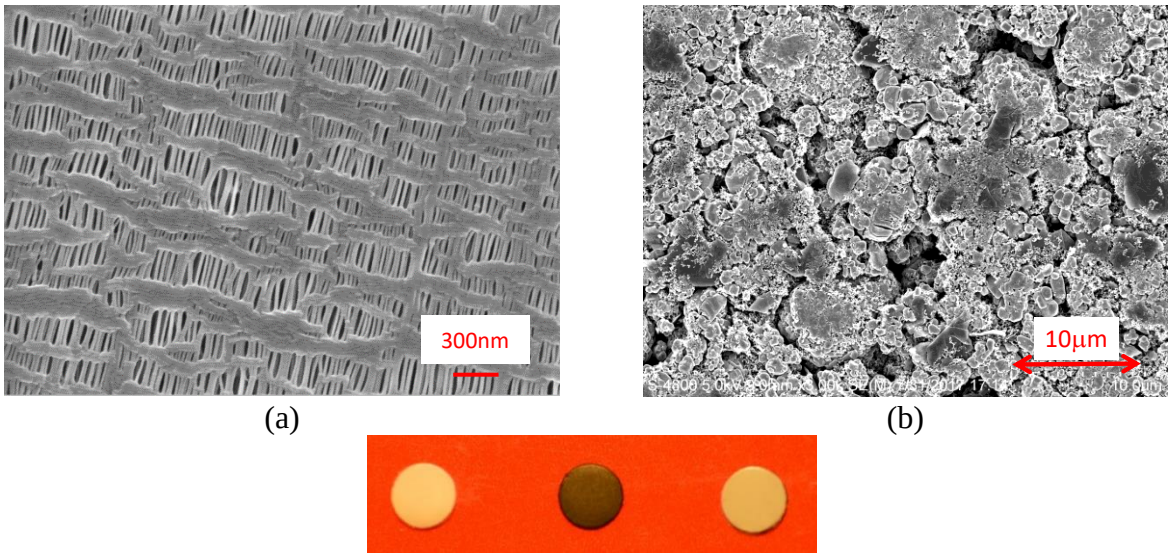

(a) (b)

(c)

Figure 4.2 Scanning electron microscope (SEM) image of the surface of (a) the Celgard® 2400 separator and (b) the NMC cathode. (c) Samples prepared by a hammer driven hole puncher. From left, PP separator, NMC cathode, PP/NMC/PP stack.

In a battery cell, the separator is sandwiched between electrodes and is stretched during the cell assembly process. The cell is slightly compressed when being assembled in a battery pack, and may be subjected to further compression during battery charging/discharging cycles [4], or in the event of impact [5,6]. To evaluate the effect of electrode roughness on the separator, a stack configuration of PP/NMC/PP was also tested, where PP represents one layer of Celgard® 2400 separator and NMC represents the NMC/Al current collector/NMC of 110 µm thickness. The nominal thickness of the stack is 160 µm.

All samples were cut using a hammer driven hole puncher. The samples were 3mm in diameter. Fig. 4.2c shows three types of samples prepared by this way. For samples with multiple layers of anisotropic separator, folding prior to cutting can help to orient the layers in the same direction [7].

4.2.3 Loading

The compression experiments were performed using a MTS Insight 10 load frame under a displacement controlled mode at a constant rate of 0.25 mm/min. The strain rate experienced by the separator samples was about 0.0005/s estimated by the sample thickness measurement. A 10 kN load cell was used for load measurement. The load cell has a resolution of 0.1N. The tests were terminated when the load reached 2.1 kN. All tests were conducted at room temperature.

To ensure that the load is uniformly applied to the glass disc assembly, rubber cushions were introduced between the upper compression platen of the testing machine and the glass disc assembly. Figure 4.3 presents the schematic of the loading mechanism in the compression experiments and a photo of the set-up. The load uniformity was found to be dependent on the shore hardness of the rubber [8]. A soft rubber will allow a better conformation to ensure the parallelism while a medium soft rubber will provide more uniform load transfer between components. One solution is to use two layers of rubbers of different hardness [9]. In this work, two grades of Neoprene rubbers were used, with a shore hardness of 10A and 40A. These hardness values are close to those used in [9]. The thickness ratio of the two rubber layers is also important. The thickness of the soft and the medium soft rubber was 6.4 mm and 9.5 mm, respectively. This resulted in a thickness ratio of 1:1.5, comparable to the ratio of 1:1.6 in Reference [9]. The rubbers were cut into 52 mm×52 mm squares.

All experiments used a compressive preload of ~1.5 N on three samples or 0.07 MPa/10 psi on each sample. The preload was applied manually by adjusting the thumb-wheel on the handset control of the MTS machine. It is expected that a small compression load will help to remove the air gap between the contact surfaces. When pouch cells are assembled in a pack, the

clamping stress can be at a level of 10 psi [10] and the applied pre-load in the current work is within this range.

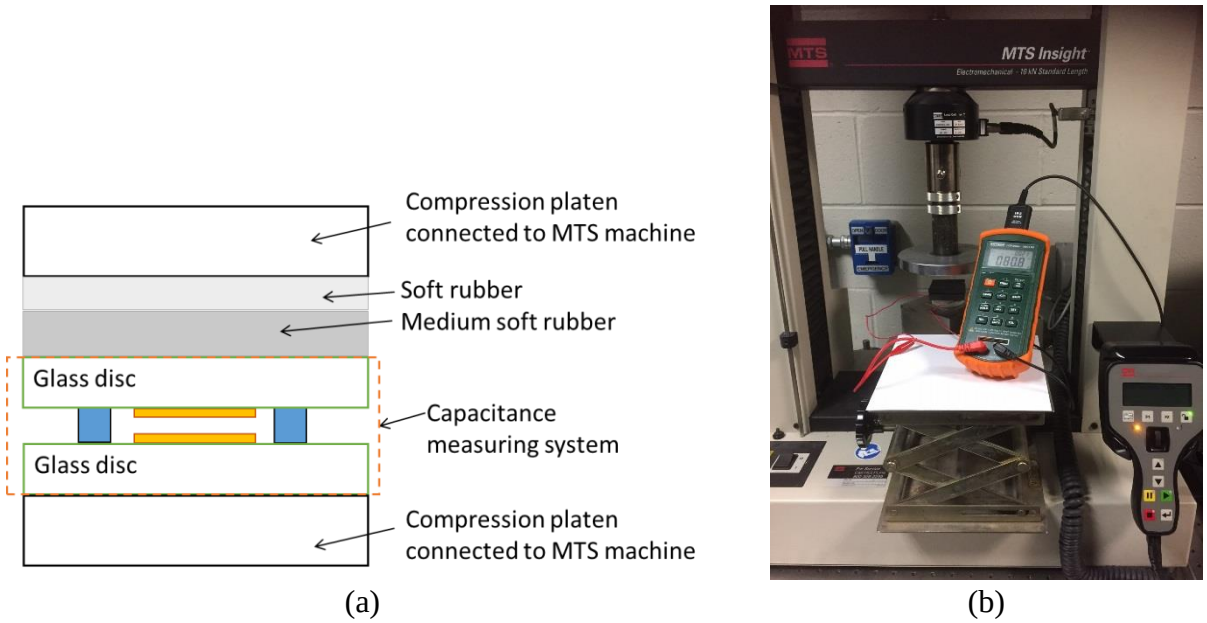

(a) (b)

Figure 4.3 The capacitance based displacement measurement set-up for the compression experiment (a) schematic plot (b) experimental set-up.

4.3 Calibration

The capacitance based displacement measurement needs to be calibrated. Such calibrations can be made using solid films of known thicknesses [11]. The calibration was carried out for the measurement set-up described in Section 2.1 in air and in DMC. In this work, Artus polyethylene terephalate (PET) films of 8 different nominal thicknesses were used in calibration. Table 4.1 provides a summary of the nominal thicknesses listed on Artus chart [12] and the values measured by a precision micrometer. The measured values were within ±3 µm (for thickness up 51 µm) and ±6 µm (for thickness larger than 51 µm) of that provided in Artus chart. By stacking two films together, additional thicknesses can be created. The calibration was performed with a total of 18 different thicknesses ranging from 12 to 171 µm. A new set of samples was used in each time. In calibration runs, the samples were only subjected to a compressive preload of ~1.5 N. Table 4.1

shows the nominal and measured thicknesses of the thin films used in calibration and a comparison of the theoretical and measured capacitance in air.

Table 4.1 The thin films used in calibration.

Artus Chart (in) (μm)	0.0005 13	0.00075 19	0.001 25	0.0015 38	0.002 51	0.003 76	0.004 101	0.005 127
Measured (μm)	12	22	24	39	52	82	105	132
Theoretical Capacitance (pF)	334.0	182.2	167.0	102.8	77.1	48.9	38.2	30.4
Measured Capacitance (pF)	216.3 ±6.9	154.3 ±1.3	149.9 ±5.5	100.8 ±2.4	78.4 ±0.3	55.4	44.9	37

Figure 4.4a plots the measured capacitance and the theoretical capacitance computed by Eq. 4.1 versus $1/t_m$ for the calibrations in air. According to Eq. 4.1, the C vs $1/t_m$ plot follows a linear relationship. At small $1/t$ values, the measured data, although slightly higher, agreed with Eq. 4.1. At large $1/t_m$, i.e. when the thickness is smaller than 50 μm, the measured capacitance starts to deviate from the linear relation. The deviation can be caused by the fringing and stray capacitances, or the limited capacitor electrode conductances due to their very small thicknesses. At t_m=50μm, the measured C value agreed well with the calculation using Eq. 4.1 with ε_{DMC}=3.10. At smaller thicknesses, the measured C values fell below the prediction of Eq. 4.1. The relationship between the capacitance and $1/t_m$ in air and in DMC can be fitted to a quadratic polynomial function. In the range of 12-171 μm, air, the relation is

$$C = -19947\left(\frac{1}{t_m}\right)^2 + 4181\left(\frac{1}{t_m}\right) + 6.6277 \tag{4.2}$$

In DMC, the relationship in the range of 12-171 μm can be determined as

$$C = -64718\left(\frac{1}{t_m}\right)^2 + 13175\left(\frac{1}{t_m}\right) + 8.6327 \tag{4.3}$$

Figure 4.4 indicates that the error in the current set-up tends to increase at smaller film thicknesses. The compression tests for Celgard® 2400 separator, therefore, were performed using samples consisting of two layers of separator. This gave an initial nominal thickness of ~50 µm.

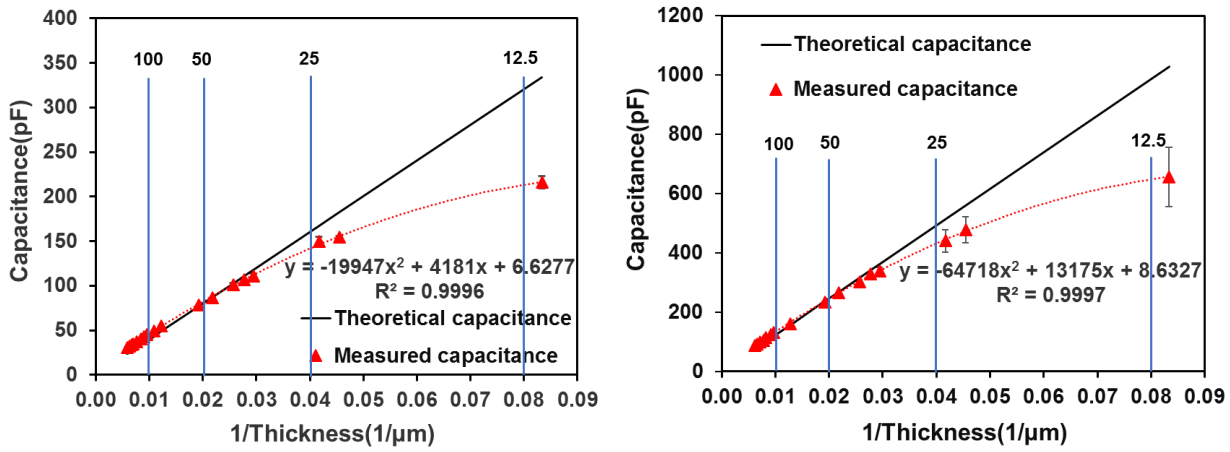

Figure 4.4 Calibration of capacitance based displacement measurement, (a) in air and (b) in DMC. The measured *C* vs *1/t* curve follows a quadratic polynomial function.

4.4 Results and Discussions

4.4.1 Separator

The compression test was performed with two layers of Celgard® 2400 separator. As shown in Calibration, the error increases at small thicknesses. Testing two layers (a total thickness of 50 microns) allow the separator to reach the compaction stage within the calibration range. The measurements were repeated three times for each condition. Each time a new set of samples was used. For the tests performed in air, the initial sample thickness measured by the capacitance method was in the range of 50.9 to 51.7 µm. For those in DMC, the initial sample thickness was 48.7~52.7 µm.

Figure 4.5 presents the measured force-capacitance and the engineering stress-strain curves. To calculate the engineering stress and strain, the dimensions of the sample measured in air were

used. The area and thickness changes after adding DMC were neglected. It was observed that the thickness change after adding DMC was less than 0.8% [13].

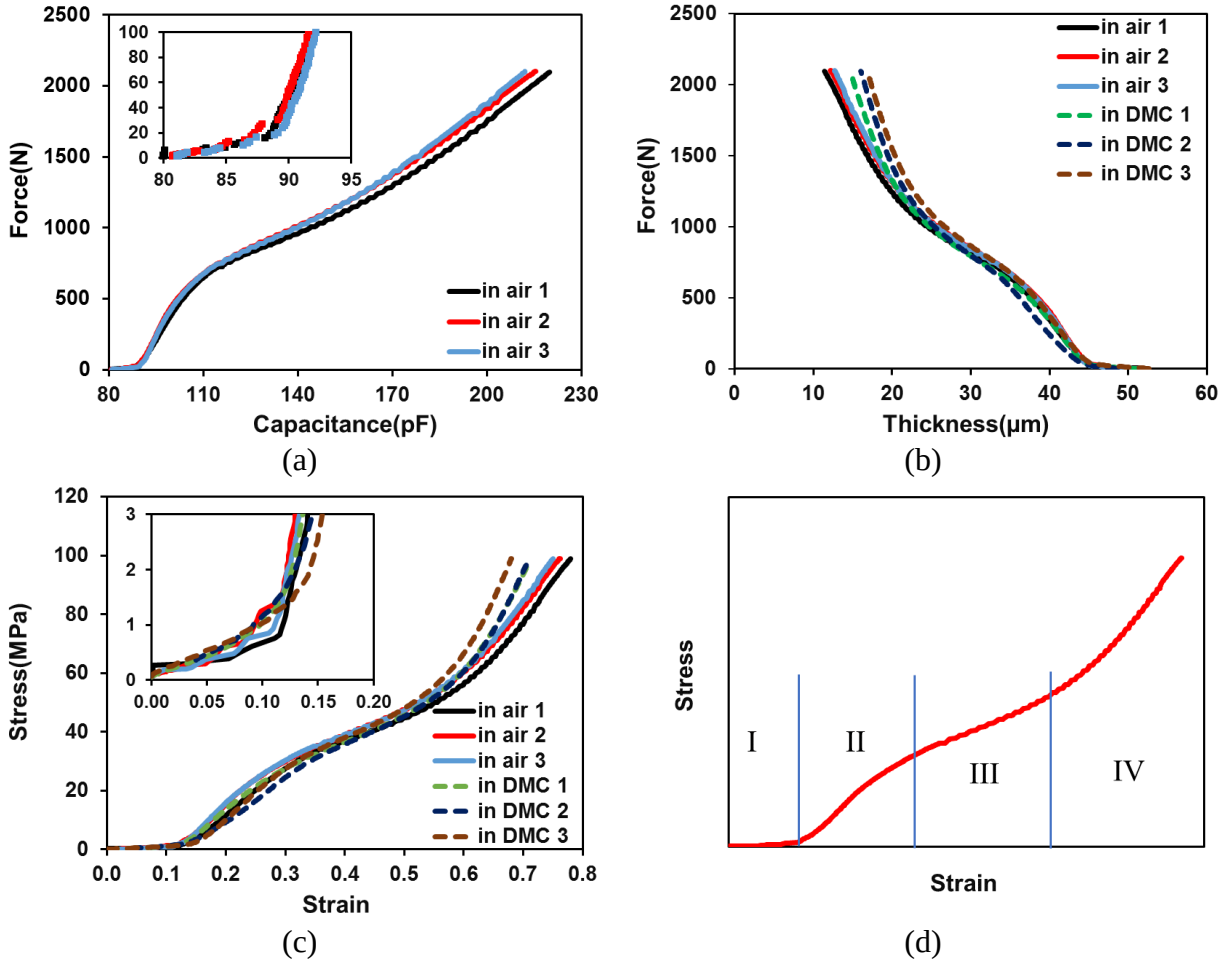

Figure 4.5 Results of compression experiments with two layers of Celgard® 2400 separator in air and in DMC. (a) The force-capacitance curves measured in air; (b) the force-thickness curves; (c) the engineering stress-strain curves. The insert shows the small strain region. (d) The four regions of the stress-strain curve.

Figure 4.5a shows that the measured curves displayed an initial region where the capacitance increased with little change in load. The insert in Fig. 4.5a presents a zoom in view of this region. As seen, the load actually increased with the capacitance in this region, although at a much lower pace. The initial region might be caused by several factors, such as the roughness of the sample surface and the burr at the sample edge as a result of sample cutting with the puncher.

These microscopic protruded areas would be loaded first. As the sample is compressed, more areas will come to contact with the glass discs and the apparent modulus of the sample material will increase with the displacement until a full contact is established. Additionally, in porous films, the deformation mechanisms during compression may evolve with the strain. For the separator investigated here, the insert of Fig. 4.5c show that it was compressed to 10% under a load of 0.8-1.0MPa before the stress-strain curve made a turn to follow a slope about 20 times greater than the load introduction region. Further investigation to understand the behaviors in this initial region is critical. This is because that the battery dimensional change in the TTD is an important parameter in the design and integration of battery packs, and the stress level in a pack under normal operational conditions falls into this initial region.

As depicted in Fig. 4.5d, the compression stress-strain curves of the separator can be divided into four regions: (I) the initial contact region, (II) the linear region, (III) yield, and (IV) compaction. The shape of the curve from II through IV is similar to the compressive stress-strain curves reported in literature [7,14,15]. In region II, the stress increases with strain in a nearly linear fashion. In region III, the slope of the curve reduces gradually as the material has reached a yield stress. In region IV, the slope of the curve increases again, as generally observed in the compaction stage in compression stress-strain curves of porous materials such as foams.

In this work, the compressive modulus of the separator was determined for regions II and IV. For II, the compressive modulus was determined in the strain range of 0.15-0.20. The value was 0.191±0.020 GPa in air and 0.165±0.020 GPa in DMC. These were close to the value of 0.21GPa in air and 0.17GPa in DMC for a monolayer PP separator Celgard® 3501 [7]. The value in air was within the range of the reported data or fitted values according to the reported stress-strain curve [6,7,14-17] of 0.1~0.3 GPa for several polymer separators measured by different

compression test methods. The ratio of the compressive modulus in DMC/in air was about 86%. This ratio is close to the estimated value of 84%~85% in the strain rate range 10^{-4} ~10^{-3}/s measured in TTD for Celgard® film 3501 separator [7], and is very close to the 88% ratio in the TD tensile modulus for Celgard® 2400 separator [18]. The results suggest a similarity in the mechanical properties between the TTD and TD.

The porous structure in PP separators such as Celgard® 2400 and 2500 is formed by a dry stretching process in which the stacked parallel lamellae is forced to separate. The resulted microstructure consists of semi-crystalline lamellae patches and amorphous nanofibers, as shown in Fig. 4.2a. The nanofibers are aligned along the MD and these are the major force carrier when the load is applied in the MD. On the other hands, the lamellae patches are oriented along the TD and TTD and they are the major force carrier in the TD and TTD. The similarity between the TD and TTD is determined by the microstructure of the separator.

In region IV, the PP separator displayed a stiffer response in DMC than that in air. The compressive modulus determined in this region was 0.386±0.035 in DMC and 0.270±0.004 in air. The stiffening in DMC at the compaction stage is likely due to the poroelastic effect where the pore solvent pressure contributes to the total stress [19]. At high strains, the pore channels can collapse leaving the solvent trapped in them. As the solvent fluid is incompressible, the resistance to compression is higher in separators whose pores are filled with immobile solvent than that with air.

4.4.2 Effect of Electrode

Figure 4.6a compares the force-thickness curves of the NMC samples measured in air and in DMC. Figure 4.6b presents the corresponding engineering stress-strain curves. As shown, NMC displayed a continuously stiffening response. Furthermore, the behavior in DMC is softer than it

is in air. In air, the compressive modulus of the NMC cathode was determined as 1.084±0.029 GPa in the strain range of 0.20-0.25. In DMC, the value was 0.892±0.033 GPa in the strain range of 0.22-0.29. These values appear to be high as compared with the values for other types of cathodes estimated from the literature data. The compressive modulus was about 0.232 GPa for a $LiCoO_2$ electrode [6] estimated in the strain range of 0.20 to 0.70, and 0.610 GPa for a $LiNiCoAlO_2$ electrode [16] in the strain range of 0.10 to 0.20. These cathodes [6,16] were taken from commercial batteries.

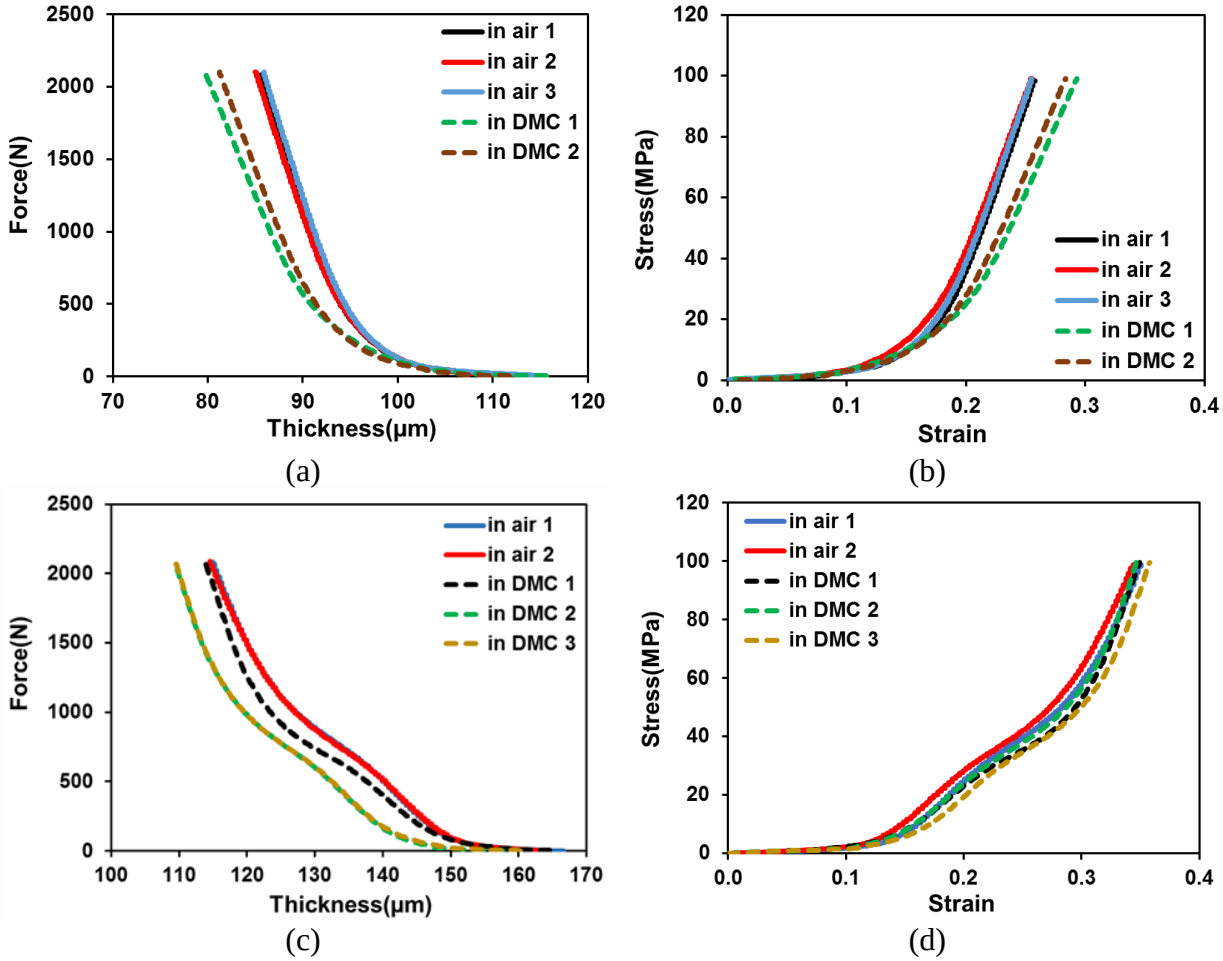

Figure 4.6 Compression of the NMC and PP/NMC/PP stack in air and in DMC. (a) Force-thickness curves of the NMC. (b) Engineering stress-strain curves of the NMC. (c) Force-thickness curves of the PP/NMC/PP stack. (d) Engineering stress-strain curves of the PP/NMC/PP stack.

Figure 4.6c and 4.6d present the results for the PP/NMC/PP stacks. The response of the PP/NMC/PP stack appears to be the combination of that of the NMC and separator. It displays four regions similar to the separator. The compressive modulus of the stack was 0.362 GPa in air and 0.336 GPa in DMC. Table 4.2 summarizes the compressive modulus of the PP separator, NMC cathode and the PP/NMC/PP stacks.

According to the iso-stress based rule of mixtures, the total deformation in the TTD of the stack equals to the summation of the deformation of the individual layers [20] and hence the strain is given by

$$\varepsilon_{PP/NMC/PP} = \frac{t_{PP}}{t_{PP} + t_{NMC}} \overline{\varepsilon_{PP}} + \frac{t_{NMC}}{t_{PP} + t_{NMC}} \overline{\varepsilon_{NMC}} \tag{4.4}$$

where $\overline{\varepsilon_{PP}}$ is the averaged strain of the three PP tests in Fig. 4.5c for the given stress, and $\overline{\varepsilon_{NMC}}$ that of the NMC tests in Fig. 4.6b; t_{PP} and t_{NMC} are the averaged initial thickness of two plies of separator and the cathode.

Fig. 4.7a plots the engineering stress-strain curves of the PP, NMC, and PP/NMC/PP in air. Fig. 4.7b compares the averaged engineering stress-strain curve of the PP/NMC/PP measured by experiments with the one computed from the stress-strain curves of the PP separator and NMC using Eq. 4.4. As shown, Eq. 4.4 provided a reasonable estimation up to a strain level of 0.16. The insert in Fig. 4.7b provides a zoom in view for the small strain region. It shows that Eq. 4.4 actually predicted a slightly stiffer response between 0.08-0.16 strains. At higher strains, the predicted stress-train behavior became softer. The result suggests a possible interaction between the PP and NMC layers. In a PP/NMC/PP stack, the PP separator is in contact with the glass disc at one side and NMC at another. Compared to that of the glass discs, the surface of the NMC layer is much rougher. At small strains, the rough surface of the NMC may press into the soft PP layer for a better

conformation between the two. If this happens, it would result in a softer response than that predicted by Eq. 4.4. At higher strains, the rough surface of the NMC may impose a greater restriction than that of the glass disc to the lateral movement/deformation of the separator. In the separator, the stress/strain state of the local areas near the surface would depend on the surface condition. A restriction in the lateral movement/deformation would raise the hydrostatic stress and increase the resistance to the deformation in TTD. This would result in a stiffer response than the prediction of Eq. 4.4. The rule of mixture was also examined for the stress-strain curve of the PP/NMC/PP stack in DMC. The results are shown in Fig. 4.7c and 4.7d. The trend is the same as that in air.

In summary, the capacitance based displacement technique is explored for the measurement of the TTD mechanical property of the separators. The capacitance change is highly sensitive to the distance change in a parallel-plate setting. This principle has been used widely in sensors in MEMS. It is the first time that the technique is used to measure the entire compressive stress-strain curves of a stand-alone thin film in air and in a solution. The TTD stress-strain curves obtained with two layers of separators is comparable to the reported work with a stack of separator. This paper reported an alternative method in characterizing the TTD behavior of the separator and other thin film materials. The capacitance based displacement technique is a good alternative method in testing the TTD mechanical property of thin films. Furthermore, the capacitance based displacement technique have been demonstrated in revealing the interaction of a single separator layer with the electrode layer. These data are in urgent need in order to precisely predict the behaviors of separators in a battery for battery pack design and under abuse conditions [5,14,21-23]. It should be emphasized here that this paper is focused on examining an alternative method for characterizing the TTD behavior of separator and its behavior in a stack. To achieve a complete

understanding of the interaction between the separator and electrode would need to couple multiple approaches which is beyond the scope of this paper.

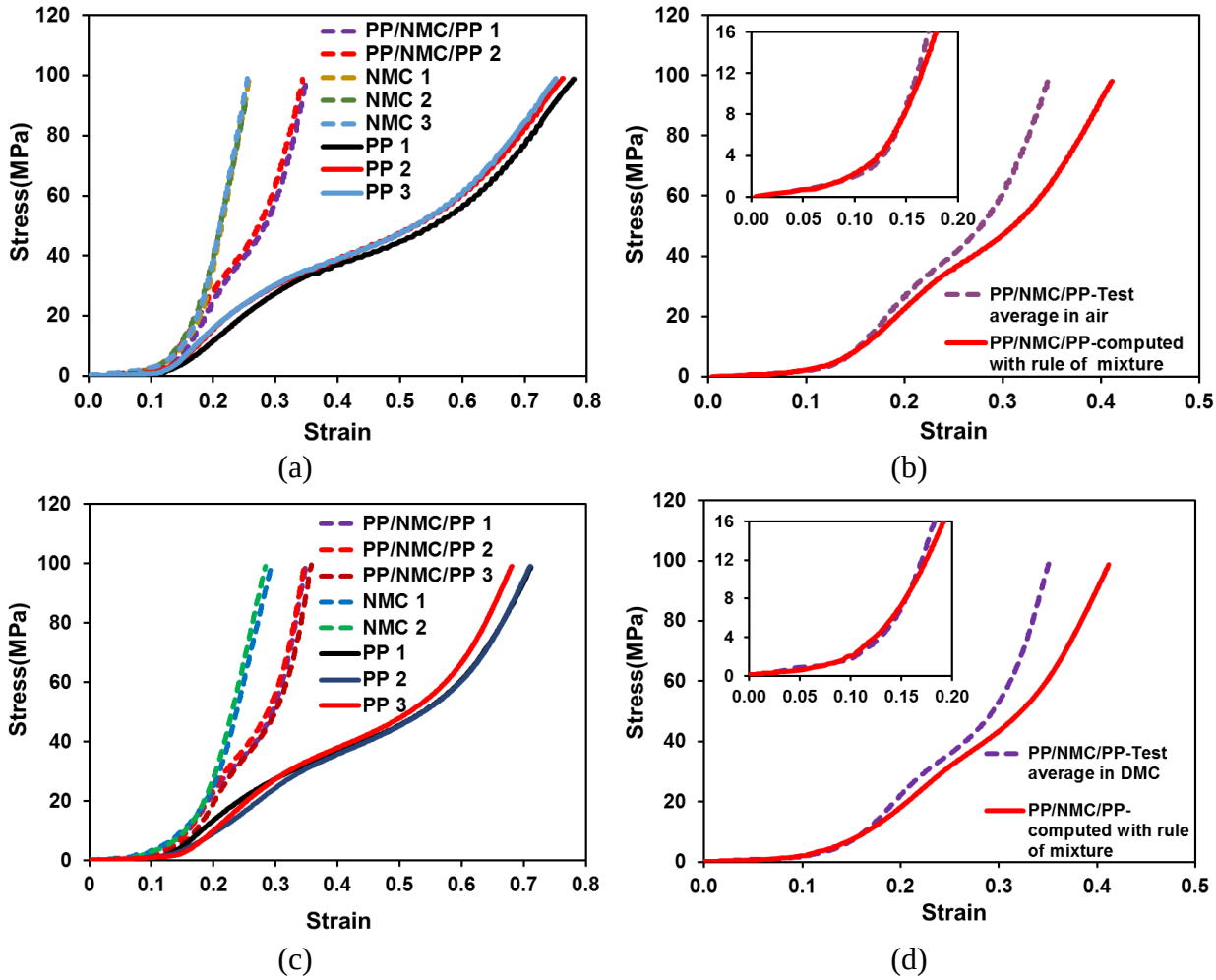

Figure 4.7 (a) The stress-strain curves of PP separator, NMC and PP/NMC/PP stack in air. (b) Comparison of the stress-strain curve of the PP/NMC/PP stack in air computed using the rule of mixtures with the measured average stress-strain curve. (c) The stress-strain curves of PP separator, NMC and PP/NMC/PP stack in DMC. (d) Comparison of the stress-strain curve of the PP/NMC/PP stack in DMC computed using the rule of mixtures with the measured average stress-strain curve.

Table 4.2 The TTD compressive modulus measured by experiment

Sample	Thickness (μm)	Compressive Modulus (GPa) in Air (strain range)	Compressive Modulus in DMC
Celgard® 2400 (PP)	51 (2 layers)	0.191±0.020 (0.15-0.20) 0.270±0.004 (0.65-0.80)	0.165±0.020 (0.15-0.20) 0.386±0.035 (0.60-0.70)

Table 4.2(cont'd)

NMC Cathode	112-116	1.084±0.029 (0.20-25)	0.892±0.033(0.22-0.29)
PP/NMC/PP	160-167	0.362±0.002 (0.15-0.20)	0.336±0.014 (0.17-0.22)

4.5 Conclusions

To measure the deformation in TTD in thin films, a capacitance based displacement measurement set-up has been developed in house. This method allows to measure the TTD compression stress-strain behavior with samples as thin as 50μm. It also allows to examine the interaction between the thin film and other materials. The TTD experiments were carried out for Celgard® 2400 PP separator, a NMC cathode and PP/NMC/PP stack.

The measurement using samples consisting of two layers of separator yielded the response comparable to the results of using a stack of separator layers. Furthermore, an initial load introduction region was observed. The PP separator was compressed up to 10% under a load of less than 0.8MPa before the stress-strain response made a turn and followed a slope about 20 times steeper. This initial region is usually omitted in published data.

The measurement was also carried out in DMC. For the PP separator, the ratio of the TTD compressive modulus in DMC/in air was 86%. The value was within the range of the TD tensile modulus measured for Celgard® 2400. The result indicates a similarity between the TD and TTD. Although initially being softer, the separator displayed a stiffer response at above 45% strain in DMC. A softer compressive response was also observed for the NMC.

The iso-stress based rule of mixtures was examined. The predicted compressive stress-strain curve for PP/NMC/PP stack was slightly stiffer first and then softer as compared to the experimental curve. Overall the prediction agreed with the experimental curve reasonably well up to about 0.16 strain. Above this strain, the measured response became increasingly stiffer than the

prediction. The rough surface of the NMC layer is likely the cause as it presents a greater constraint to the deformation of the separator at large strains.

REFERENCES

REFERENCES

1. H.C. Liou, R. Willecke, P.S. Ho, Study of out-of-plane elastic properties of PMDA-ODA and BPDA-PDA polyimide thin films, Thin Solid Films, 323 (1998) 203–208.

2. L.G. Hector and H.L. Schultz, The Dielectric Constant of Air at Radiofrequencies, Journal of Applied Physics, 7(1936) 133-136.

3. D.S. Hall, J. Self, J.R. Dahn, Dielectric constants for quantum chemistry and li-ion batteries: solvent blends of ethylene carbonate and ethyl methyl carbonate, The Journal of Physical Chemistry C, 119 (2015) 22322–22330.

4. W. Wu, X. Xiao, X. Huang, S. Yan, A multiphysics model for the in situ stress analysis of the separator in a lithium-ion battery cell, Computational Materials Science, 83 (2014) 127–136.

5. C. Zhang, S. Santhanagopalan, M.A. Sprague, A.A. Pesaran, Coupled mechanical-electrical-thermal modeling for short-circuit prediction in a lithium-ion cell under mechanical abuse, Journal of Power Sources, 290 (2015) 102–113.

6. E. Sahraei, R. Hill, T. Wierzbicki, Calibration and finite element simulation of pouch lithium-ion batteries for mechanical integrity, Journal of Power Sources, 201 (2012) 307–321.

7. J. Cannarella, X. Liu, C.Z. Leng, P.D. Sinko, G.Y. Gor, C.B. Arnold, Mechanical Properties of a Battery Separator under Compression and Tension, Journal of The Electrochemical Society, 161 (2014) F3117–F3122.

8. H. Wang, S. Li, X. Yue, Q. Wang, Study on Design and Test of Flexible Uniform Pressure Loading Device, Advanced Science Letters, 4 (2011) 646–650.

9. Q. Wang, H. Wang, S. Li, Z. Li, W. Li, B. Jiang, D. Wang, Development and test analysis of flexible uniform pressure loading device, Chinese Journal of Rock Mechanics and Engineering, 31 (2012) 133–139.

10. X. Xiao, W. Wu, X. Huang, A multi-scale approach for the stress analysis of polymeric separators in a lithium-ion battery, Journal of Power Sources, 195 (2010) 7649-60.

11. T.Y. Wu, D.L. Questad, Mechanical Characterization and Constitutive Description of Thin-Film Polymeric Materials, in: Symposium G – Electronic Packaging Materials Science VI, (1992) 143-161.

12. Plastic Shim Stock, Color Coded Shim Stock: Artus Corp., http://www.artuscorp.com/content.cfm/Shim-Stock/Plastic-Shim-Stock/category_id/2/content_id/3.

13. G.Y. Gor, J. Cannarella, C.Z. Leng, A. Vishnyakov, C.B. Arnold, Swelling and softening of lithium-ion battery separators in electrolyte solvents, Journal of Power Sources, 294 (2015) 167–172.

14. X. Zhang, E. Sahraei, K. Wang, Li-ion Battery Separators, Mechanical Integrity and Failure Mechanisms Leading to Soft and Hard Internal Shorts, Scientific Reports, 6 (2016) 32578.

15. X. Zhang, E. Sahraei, K. Wang, Deformation and failure characteristics of four types of lithium-ion battery separators, Journal of Power Sources, 327 (2016) 693–701.

16. M. Gilaki, I. Avdeev, Impact modeling of cylindrical lithium-ion battery cells: a heterogeneous approach, Journal of Power Sources, 328 (2016) 443–451.

17. I.C. Halalay, M.J. Lukitsch, M.P. Balogh, C.A. Wong, Nanoindentation testing of separators for lithium-ion batteries, Journal of Power Sources, 238 (2013) 469–477.

18. A. Sheidaei, X. Xiao, X. Huang, J. Hitt, Mechanical behavior of a battery separator in electrolyte solutions, Journal of Power Sources, 196 (2011) 8728–8734.

19. G.Y. Gor, J. Cannarella, J.H. Prévost, C.B. Arnold, A model for the behavior of battery separators in compression at different strain/charge rates, Journal of The Electrochemical Society, 161 (2014) F3065–F3071.

20. M.W. Hyer Stress Analysis of Fiber-Reinforced Composite Materials, DEStech Publications, Lancaster, PA, 2009.

21. B. Liu, H. Zhao, H. Yu, J. Li, J. Xu, Multiphysics computational framework for cylindrical lithium-ion batteries under mechanical abusive loading, Electrochimica Acta, 256 (2017) 172–184.

22. B. Liu, S. Yin, J. Xu, Integrated computation model of lithium-ion battery subject to nail penetration, Applied Energy, 183 (2016) 278–289.

23. J. Xu, B. Liu, X. Wang, D. Hu, Computational model of 18650 lithium-ion battery with coupled strain rate and SOC dependencies, Applied Energy, 172 (2016) 180–189.

CHAPTER 5 THERMAL EXPANSION/SHRINKAGE MEASUREMENT

5.1 Introduction

This Chapter presents a systematical investigation on the use of a DMA under tensile mode for the thermal expansion/shrinkage and CTE measurement of battery separators. Factors such as the calibration procedure, the influence of the tensile load and the temperature ramp rate were examined. Using the established method, the measurements were carried out for three common types of LIB separator from ambient to the maximum temperature that the measurement can be performed. The CTE as a function of temperature was determined from the DMA data.

5.2 Experimental

5.2.1 Materials

Three representative separators were investigated in this work. They were: (1) Celgard® 2400, a monolayer PP; (2) Celgard® 2325, a trilayer PP/PE/PP; and (3) Celgard® Q20S1HX, a ceramic coated trilayer PP/PE/PP. The film thickness was 25μm for 2400 and 2325, and 20 μm for Q20S1HX.

5.2.2 Measurement

The experiment was performed with a TA Q800 DMA under tensile mode. DMA is a common mechanical testing equipment to characterize the viscoelastic behavior of materials. Figure 5.1 shows the experimental set-up. The sample was gripped at both ends with tension clamps. Then, the cell was closed and the temperature ramped. The thermal shrinkage can be investigated by two modes: the iso-stress mode and the iso-strain mode. Under the iso-stress mode, a constant force was maintained and the lengthwise variation of the sample gage length was measured. This helps to evaluate the thermal shrinkage and the coefficient of thermal expansion

(CTE). Under the iso-strain mode, the force variation is measured. It helps to investigate the fracture stress.

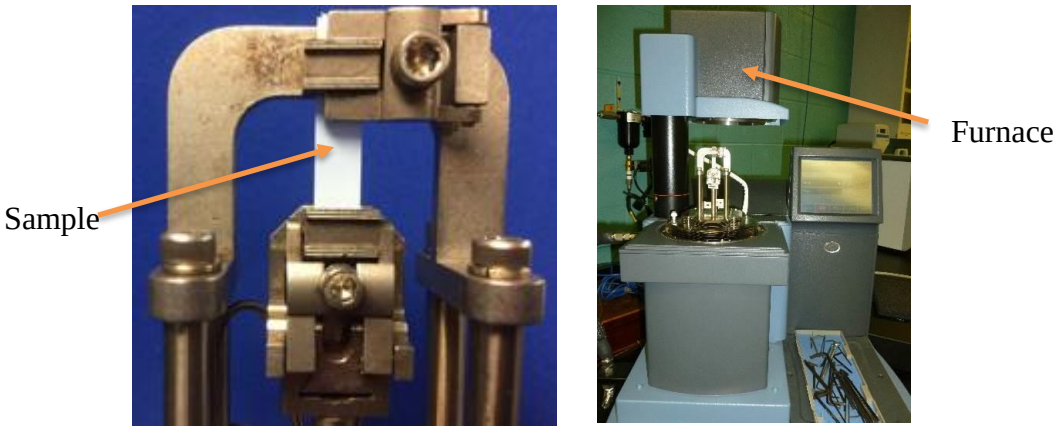

Figure 5.1 (a) A sample is mounted in the tensile clamp in DMA Q800. (b) The furnace will then be closed for temperature ramp.

The samples, in the form of long strips with a gage length of 15 mm and width of 6 mm, were cut using a razor blade. The sample width was then measured, on a flat surface, using a caliper. To investigate the influence of the sample aspect ratio, the sample length was increased to 24mm or decreased to 6mm while the sample width remained as 6mm. Samples were prepared both along MD and TD, as shown in Fig. 5.2. Three types of separators were tested in iso-stress mode. Both MD sample and TD sample were tested for each type of separator. So far, only Celgard® 2400 MD samples have been tested in iso-strain mode.

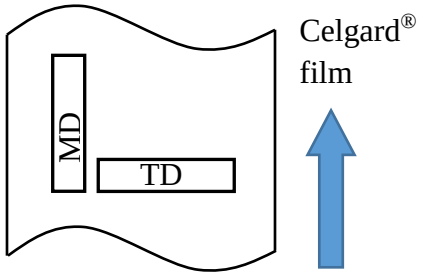

Figure 5.2 The MD sample and TD sample.

In iso-stress mode, Celgard® 2400 was tested first to investigate the effect of the test parameters such as the level of the tensile load and the temperature ramp rate. The experiments were performed at multiple heating rates and force levels. A preload of 0.01N and 0.001N was selected for the MD and TD samples, respectively, and a heating rate of 3ºC/min was selected for both samples. The results of these investigations will be presented in Section 5.3.1.1.

In iso-strain mode, Celgard® 2400 was tested at the strain level 0.1%, 0.3%, 0.9%, 2.7%.

5.2.3 Calibration

Prior to the CTE measurement, the DMA needs to be calibrated using a material with known CTE. In this work, the calibration was performed with Al thin foil of 25μm thickness with a purtiy of 99%. The sample dimensions and their mounting in the DMA were the same as that described in 2.2. The measurement was performed under a small tensile loading of 0.01N over the temperature range from ambient to 220ºC with a heating rate of 3ºC/min.

Figure 5.3a presents the measured grip displacement with increasing temperature obtained with the Al samples. The slopes of the curves appear to be negative, implying a negative CTE, i.e. shrinkage instead of expansion. For a sample with a known CTE, the change in sample gage length with temperature can be calculated. For pure Al, the CTE is reported as 24.5×10^{-6}/ºC over the range of 20-200ºC [1]. The displacement predicted this way is presented by the dashed line in Fig. 5.3a. The discrepency between the predicted curve and the measuremed curves indicates that the measured grip displacement included the contribution from other components in addition to that of the sample.

In TA DMA systems, the grip displacement is measured by a sensor located on the drive shaft [2]. The measured displacement includes the dimensional change of the sample, the grip, and

the drive shaft relative to a stationary component [2], in addition to that of the sample. The standard calibration procedure for the DMA uses a steel sample and the calibration is performed at ambient temperature. Based on the calibration, the contribution of the testing fixture compliance is automatically excluded from the DMA output. This is sufficientlly accurate for mechanical testing, as verified by comparing the DMA data with the digital image correlation measurement [3]. In measurements over a temperature range, all components, including the stationary component, will experience thermal expansion/shrinkage. In mechanical testing, the strain due to the dimensional change of the testing fixture is usally negligible compared to the deformation experienced by the sample. For CTE measuremnts, additional calibration is needed. The calibration should be performed with the same experimental set-up and under the same testing condition.

To determine the true dimensional change of the sample, the contribution of the testing fixture must be known in advance. This amount is designated as $\Delta l_{calibration}$, determined by the difference between the predicted dimensional change $\Delta l_{predicted}$ over the gage length l of the sample used in calibration, and the measured dimensional change $\Delta l_{measrued}$ by the DMA [4]

$$\Delta l_{calibration} = \Delta l_{predicted} - \Delta l_{measured} \tag{5.1}$$

The predicted gage length change of the calibration sample is computed as

$$\Delta l_{predicted} = \mathrm{CTE} \times l_0 \times (T - T_0) \tag{5.2}$$

where l_0 is the initial sample length.

Figure 5.3b presents the $\Delta l_{calibration}$ for the current CTE measurement set-up obtained with the Al samples. The true dimensional change of the sample $\Delta l_{corrected}$ can be determined by the following correction

$$\Delta l_{corrected} = \Delta l_{calibration} + \Delta l_{measured} \tag{5.3}$$

The established calibration was verified by testing a Cu foil of 50μm thickness with a purtiy of 99.9%. Figure 5.3c presents the $\Delta l_{measured}$ for two Cu samples and $\Delta l_{corrected}$ calculated using Eq. 5.3. Then, the engineering strain was calculated as $\varepsilon=\Delta l_{corrected}/l_0$. The CTE is defined as a change in strain in response to a change in temperature

$$CTE = \frac{d\varepsilon^T}{dT} \tag{5.4}$$

The CTE for the Cu foil determined in this way was 17.1×10^{-6}/ºC, which is within 1.2% of the reported CTE value of 17.3×10^{-6}/ºC for pure Cu over the range of 20-200ºC [5].

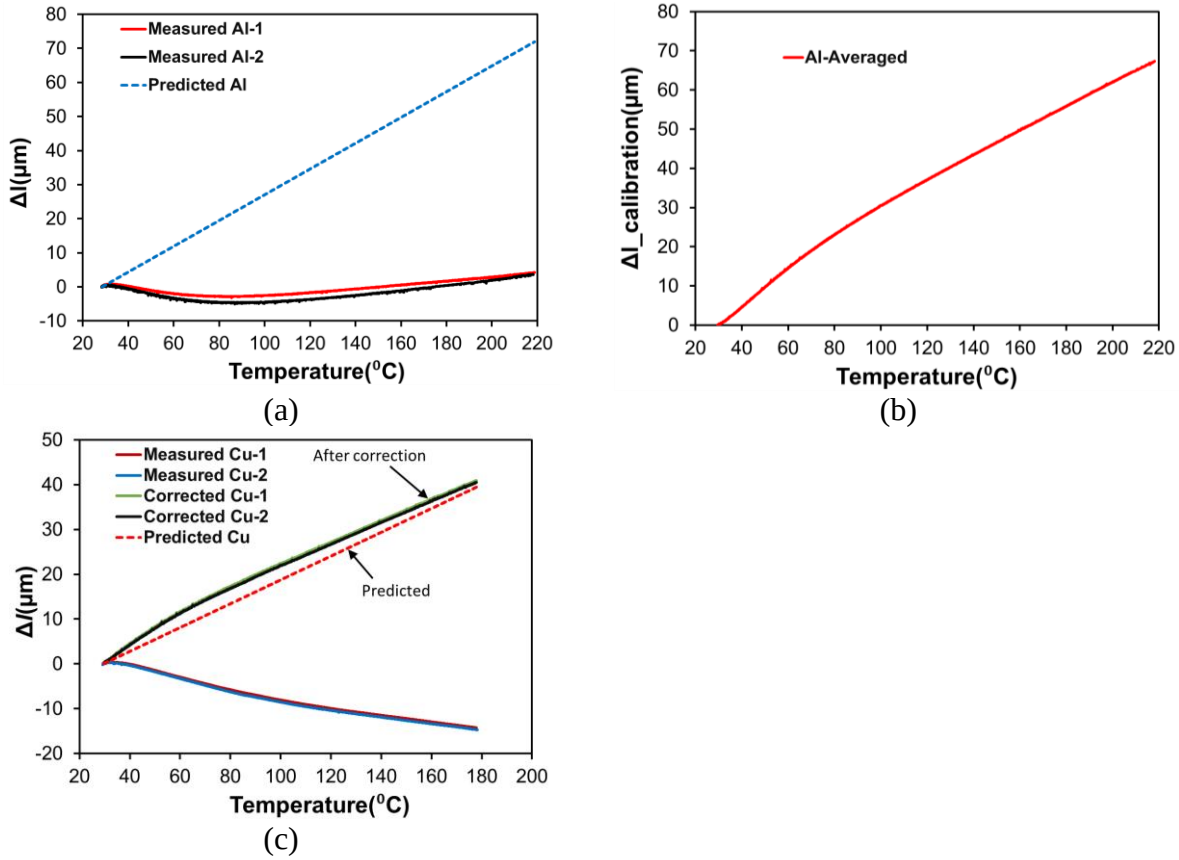

Figure 5.3 (a) The measured Al sample length change and the predicted sample length expansion. (b) The calibration curve. (c) The measured Cu sample length change before and after correction, and the predicted length change.

5.3 Results and Discussions

5.3.1 Iso-stress

5.3.1.1 Expansion/Shrinkage Measurement

5.3.1.1.1 Effect of tensile load

To keep the sample straight during the measurement, a small tensile load is needed. The load should be as small as possible to avoid the influence of creep strain. On the other hand, it is difficult to maintain a very small load accurately. The effect of tensile load on the measurement was investigated using Celgard® 2400 at a ramp rate of 3ºC/min. These measurements were repeated two times at each load level. The repeatability of the measurement was very good. The averaged curves are presented in Fig. 5.4.

Figure 5.4 shows that the load level had a significant effect on the measurement. The repeated tests are shown in Fig. A.1 in Appendix A. For the MD samples (Fig. 5.4a), the measurements were performed under three load levels, 0.01N, 0.02N and 0.45N, corresponding to stress levels of 0.067MPa, 0.13MPa and 3MPa. At 3MPa, the sample did not shrink as the creep strain had exceeded the thermal strain. Under 0.067MPa and 0.13MPa, the measured expansion/shrinkage was almost identical, indicating that a stress level of 0.067MPa is sufficiently low for the MD samples. For the TD (Fig. 5.4b), the measurement was made under 0.007MPa, 0.014MPa, 0.067MPa and 0.13MPa. Unlike the MD, the expansion/shrinkage curve and the peak/valley values of the TD samples continue to change with the stress. Finally, a stress level of 0.007MPa was selected as this corresponds to the minimum force of 0.001N which the DMA can maintain.

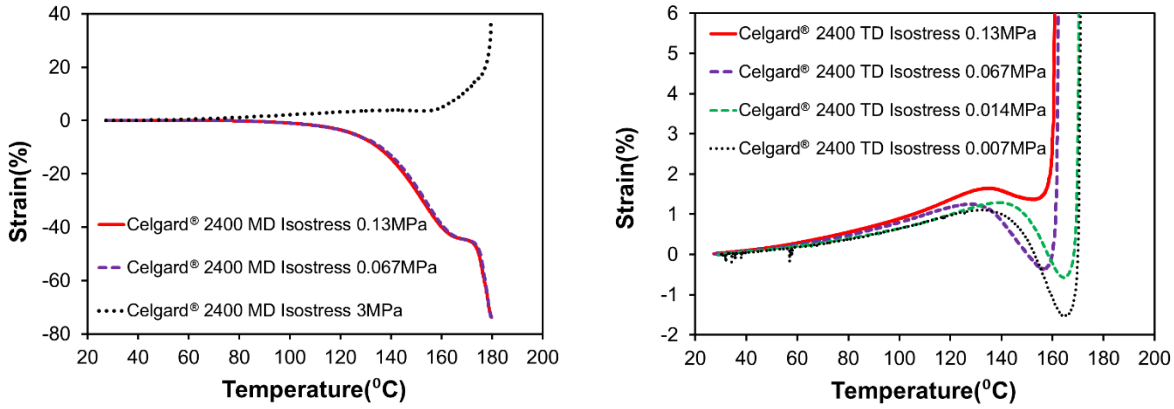

(a) (b)

Figure 5.4 The measured expansion/shrinkage strain under different stress levels for Celgard® 2400 (a) MD and (b) TD samples.

5.3.1.1.2 Effect of heating rate

The effect of the temperature ramp rate on the expansion/shrinkage behavior was investigated using Celgard® 2400 TD samples. The repeated tests are shown in Fig. A.2 in Appendix A. The results are shown in Fig. 5.5. For 3ºC/min and 5ºC/min, the amount of the expansion below 120ºC and shrinkage between 140ºC and 160ºC were about the same. At the two higher rates, however, these amounts decreased. This is probably due to the thermal lag between the temperature measured by the thermocouple of the DMA and the sample [6,7]. A faster temperature ramp rate causes a larger thermal lag [6]. T_{Shrink}, the temperature when the sample starts to shrink, as marked on Fig. 5.5a, may be another indication of the thermal lag effect. As shown in Fig. 5.5b, T_{Shrink} increased sharply when the rate increased from 3ºC/min to 5ºC/min. Therefore, a 3ºC/min ramp rate was selected. Table 5.1 lists the testing conditions for further investigations.

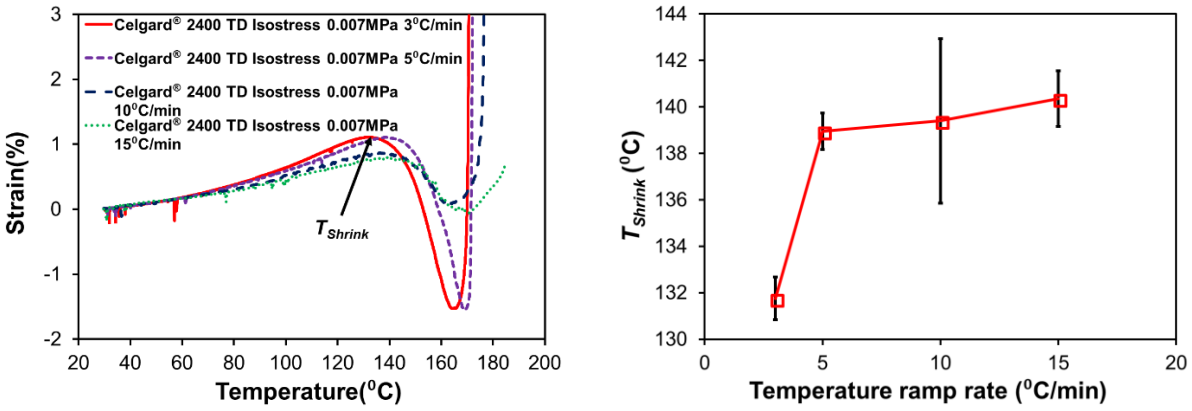

(a) (b)

Figure 5.5 The effect of the temperature ramp rate on Celgard® 2400 TD samples. (a) The measured thermal expansion/shrinkage, and (b) T_{Shrink}, the temperature when the sample starts to shrink.

Table 5.1 Test conditions for MD and TD samples

Testing conditions	MD samples	TD samples
Tensile stress (MPa)	0.067	0.007
Temperature ramp rate (°C/min)	3	

5.3.1.1.3 Comparison with oven isothermal test

The shrinkage of separators is often measured with an oven isothermal test [8-12]. In this method, the sample is heated in an oven to the desired isothermal temperature for a period of 30 minutes to 1 hour. The dimensions of the sample are measured immediately after it has been removed from the oven.

In this study, oven isothermal tests were performed with Celgard® 2400 MD samples of 55x6 mm at 130°C, 155°C, 160°C, 170°C and 180°C. The sample was placed on a clean and smooth microscope slide and heated for 30 minutes in a conventional oven at the desired temperature. The length of the sample before and after was measured with a caliper. The oven tested samples are shown in Fig. 5.6. The change in the sample length and appearance is noticeable. The sample

tested at 170ºC became transparent and curled. At 180ºC, the sample had melted as it became attached to the glass slide.

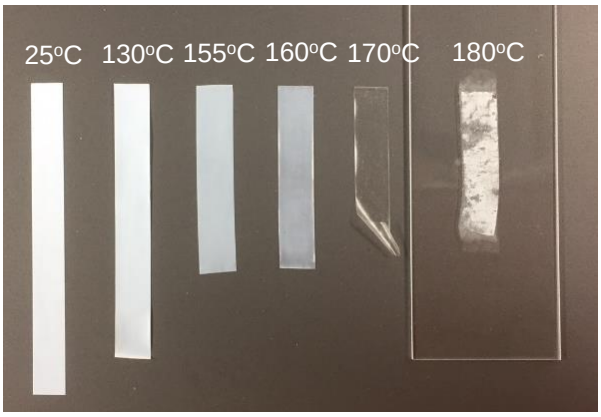

Figure 5.6 Celgard® 2400 MD samples after isothermal conditioning for 30 minutes in an oven. From left to right: 25ºC, 130ºC, 155ºC, 160ºC, 170ºC and 180ºC.

Table 5.2 compares the shrinkage measured using the isothermal method and by the DMA. The agreement between the two methods is rather good except at 180ºC. The glass slide apparently had restricted the shrinkage of the sample during the isothermal conditioning.

Comparing the two methods, the isothermal test is relatively simple and requires only an oven. However, the measurements can be performed only at selected temperatures. The DMA provides a continuous measurement and the measurement is automatically recorded. Overall, the DMA is less time consuming and more accurate than the isothermal method.

Table 5.2 Celgard® 2400 MD shrinkage strains measured using oven isothermal test and DMA temperature ramp test

Testing temperature (ºC)	130	155	160	170	180
Shrinkage measured by oven isothermal test (%)	-9.1	-37.3	-40.0	-43.6	-50.9
Shrinkage measured using DMA (%)	-6.6	-31.8	-38.7	-44.4	-73.6

5.3.1.1 Expansion/Shrinkage of Three Separators

Figure 5.7 compares the typical expansion/shrinkage behaviors of three types of separators after calibration as shown in section 5.2.3. The raw data and calibrated data are shown in Appendix B.

Figure 5.7a compares the expansion/shrinkage behaviors along MD. In general, Celgard® 2400 and 2325 show similar behavior, whereas Q20S1HX is distinctively different. For a better comparison, Fig. 5.7b and Fig. 5.7c provide zoom-in views for 20-80°C and small strain regions, respectively. As shown in Fig. 5.7b, 2400 and 2325 expanded slightly up to 60°C, and then started to shrink. At 180°C, the shrinkage was about 75%. On the other hand, Q20S1HX shrank steadily with increasing temperature. Its maximum shrinkage was less than 1%. The sample ruptured at 220°C.

Table 5.3 compares the shrinkage data provided in manufacturer's datasheet and the results from the current DMA measurement. The shrinkage in the datasheet was indicated as one hour at the temperature.

For 2400 and 2325 MD, the shrinkage reported in the datasheet is <5% at 90°C. The value measured using the DMA was about 0.3%. At 105°C, the shrinkage for 2325 is 2.21% in the datasheet. The DMA value was about 1.2%. For Q20S1HX MD, the DMA data were within the shrinkage reported in the datasheet.

Table 5.3 Shrinkage from manufacturer's data sheet measured after being kept at the temperature for one hour and from DMA measurement at 3°C/min

	Celgard® 2400		Celgard® 2325		Celgard® Q20S1HX	
Thickness	25 μm		25 μm		20 μm	
Shrinkage	Datasheet	DMA	Datasheet	DMA	Datasheet	DMA

Table 5.3(cont'd)

MD, 90°C	<5.0%	0.3%	<5.0%	0.4%		
TD, 90°C	0.0%	0.0%	0.0%	0.0%		
MD, 105°C			2.21%	1.2%		
TD, 105°C			0.0%	0.0%		
MD, 130°C					<2%	0.5%
TD, 130°C					<1%	0.0%
MD, 150°C					<4%	0.8%
TD, 150°C					<2%	1.7%

0% indicates there was no shrinkage.

Figure 5.7d compares the shrinkage behavior in the TD. The tendency of shrinkage in the TD for these three separators is opposite to that in the MD. The TD shrinkage value is Q20S1HX>2400>2325, although their differences were smaller than that in the MD. Q20S1HX started to shrink at about 130°C. The shrinkages was about 0% at 130°C and 1.7% at 150°C. These values compared well with the values in datasheet. The datasheet reports no shrinkage for 2400 up to 90°C and for 2325 up to 105°C. These are confirmed by the DMA data in this work. Both 2400 and 2325 displayed expansion behavior up to about 130°C.

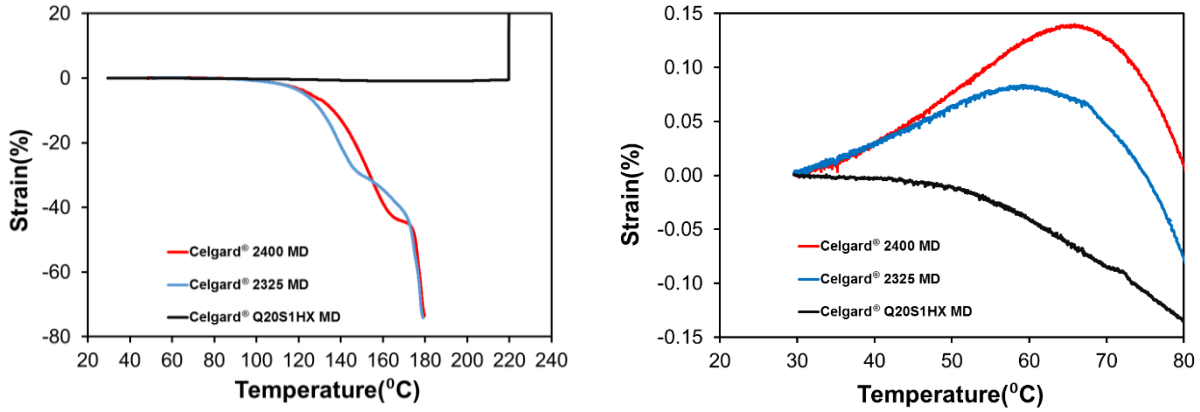

(a) (b)

Figure 5.7 Comparison of expansion/shrinkage behaviors of three types of separators, (a) the MD samples, (b) the MD samples from 20-80°C, (c) the MD samples for small strain range, and (d) the TD samples.

Figure 5.7(cont'd)

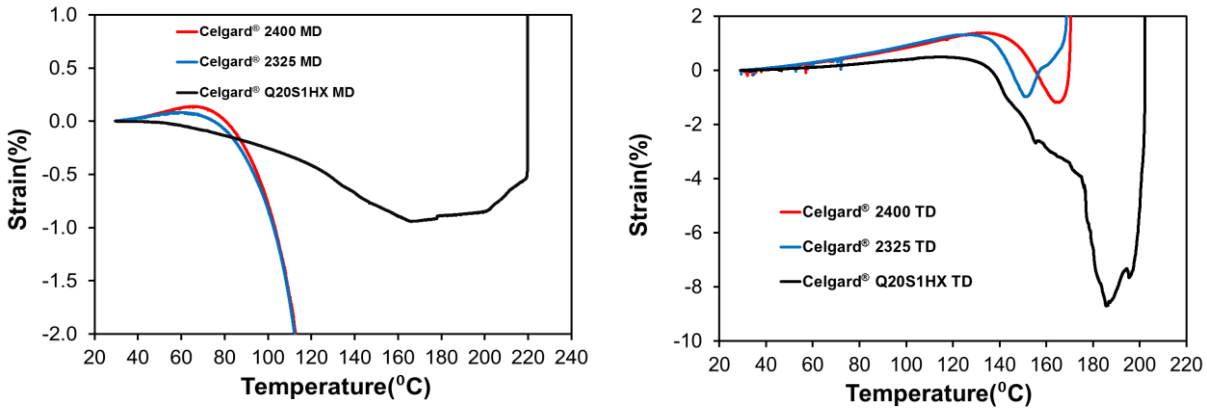

(c) (d)

The significant shrinkage of Celgard® 2400 and 2325 in the MD is due to their microstructures showed in Fig. 1.2. The pores and fibers were introduced by uniaxially stretching the film along the MD [13]. As a result, the polymer chains are disentangled and elongated. When the temperature was increased, the oriented amorphous phase shrank before the fusion of crystals. Then, the crystals melted, and the chains became disoriented. This leads to the large thermal shrinkage along the MD [14]. The shrinkage of Celgard® 2400 and 2325 TD samples was less than 2% as the TD was not stretched during manufacturing. This anisotropic shrinkage would be restricted with a ceramic coated layer, as in the case of Q20S1HX.

Figure 5.8 compares the samples after the experiment. For 2400 and 2325 MD samples, the measurement terminated when the gage length reached the minimum value allowed by the tension clamp. The length of the tested samples shrank from 15mm to about 5mm without noticeable change in the width (Fig. 5.8a). Their rupture temperature would be higher than 180°C. On the other hand, the measurement for Q20S1HX lasted until 220°C when the separator actually ruptured (Fig. 5.8b). This corresponds to a sharp increase in strain in Fig. 8a. At the end of the tests, the Celgard® 2400 and 2325 TD samples necked (Fig. 5.8c) while Q20S1HX TD samples ruptured (Fig. 5.8d). Table 5.4 provides a summary for the temperature when necking/rupture

occurs. For the TD samples, these values were 15ºC ~35ºC lower than the MD samples for all three separators. Table 5.4 compares the temperatures when the samples started to shrink and neck/fracture for three separators in the MD and TD.

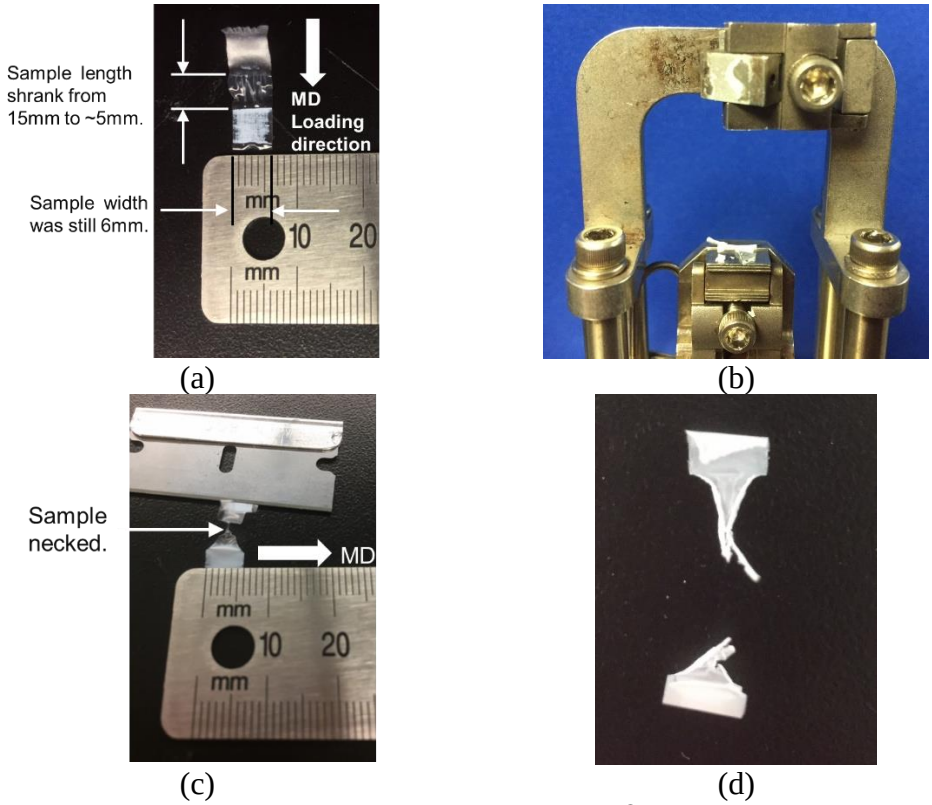

Figure 5.8 Samples after the experiment: (a) Celgard® 2400 MD (2325 MD is similar), (b) Celgard® Q20S1HX MD, (c) Celgard® 2400 TD (2325 TD is similar); and (d) Celgard® Q20S1HX TD sample.

Table 5.4 Temperatures when the samples started to shrink and neck/fracture

Sample / Temperature	Celgard® 2400		Celgard® 2325		Celgard® Q20S1HX	
	MD	TD	MD	TD	MD	TD
T At Shrink (ºC)	~65	~133	~60	~125	~30	~115
At Neck/fracture (ºC)	>180	~165	>180	~150	~220	~185

In summary, the shrinkage data obtained by the DMA measurement yielded a similar trend as that in the datasheet. At 90ºC, Celgard® 2400 and 2325 have similar shrinkage behavior and the shrinkage is much higher in the MD. Q20S1HX shows more isotropic shrinkage behavior.

5.3.1.2 Coefficient of Thermal Expansion (CTE)

As described by Eq. 5.4, the CTE is the derivative of the strain-temperature curve. Since the curves in Fig. 5.7 were all nonlinear, each curve was divided into several segments and the CTEs were determined in a piecewise fashion. This procedure is illustrated in Fig. 5.9 using the Celgard® 2400 MD sample as an example.

The strain-temperature curve of 2400 MD sample (Fig. 5.7a) can be divided into two segments. The first segment is 25<T<65°C, where the sample expanded, and the strain increased linearly. This segment is replotted in Fig. 5.9a. The curve was fitted using a linear function as shown by the blue dashed curve. The slope of the curve was constant and is given by the black line with a scale shown by the secondary vertical axis.

The second segment is 65<T<180°C. It was replotted in Fig. 5.9b. In this segment, the sample shrank and the strain decreased nonlinearly. The curve was fitted using a power function. The derivative of the curve provides the CTE function. Figure 5.9c presents the combined strain and CTE curves. As shown, the piecewise method yields a smooth relation for the CTE over the entire temperature range. This relation can be used conveniently in finite element analysis.

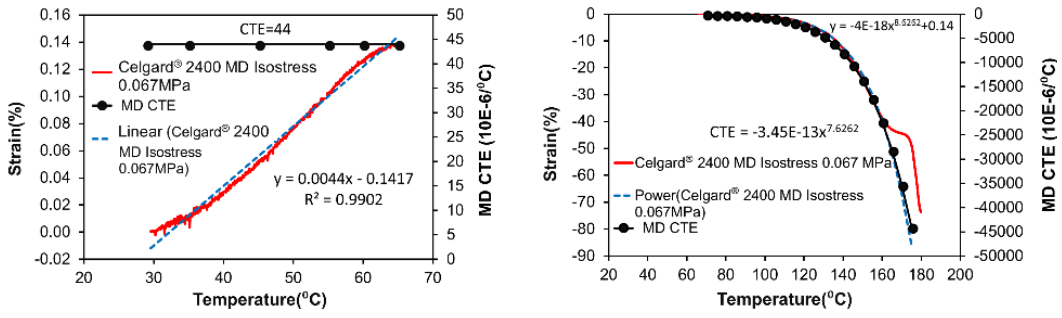

(a) (b)

Figure 5.9 Determine the CTE of Celgard® 2400 MD. The shrinkage curve was divided into two segments, curve fitting was performed for each segment, and the slope of the curve for the segment gave the CTE. (a) The first segment, (b) the second segment, and (c) the combined curve.

Figure 5.9(cont'd)

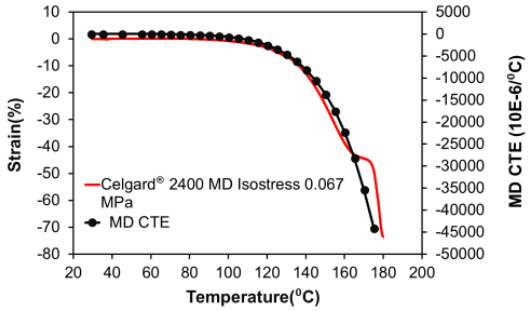

(c)

Following the same procedure, the CTE was determined for Celgard® 2400 TD, 2325 and Q20S1HX MD and TD. The details are shown in Appendix C. These results are summarized in Table 5.5.

Table 5.5 CTE for Celgard® 2400, 2325 and Q20S1HX

Material	Temp (ºC)	CTE (x10-6/°C)
2400 MD	30-65	44
	65-175	$-3.45 \times 10^{-13} T^{7.6262}$
2400 TD	30-130	1.4T+26
	130-140	0
	140-160	-88T+12044
2325 MD	30-60	30
	60-175	$-5.1 \times 10^{-13} T^{7.5641}$
2325 TD	30-120	1.6T+25
	120-130	0
	130-150	-124T+16087
Q20S1HX MD	30-160	-1.2T+39
	160-200	29

Table 5.5(cont'd)

Q20S1HX TD	30-110	T-1
	110-135	0
	135-175	28T-5479
	175-185	540T-101850

5.3.2 Iso-strain

5.3.2.1 The Effect of Iso-strain Levels

The effect of the iso-strain level was investigated. The Celgard® 2400 MD samples were tested at 0.1%, 0.3%, 0.9%, 2.7% strains. Data was considered as stable when the strain variation was within ±5% of the iso-strain level. Figure 5.10 shows that the strain variation becomes larger than ±5% at 140ºC at a strain of 0.1%. For strain levels of 0.3%~2.7%, the strain variation becomes larger than ±5% at ~160ºC. The values are shown in Table 5.6.

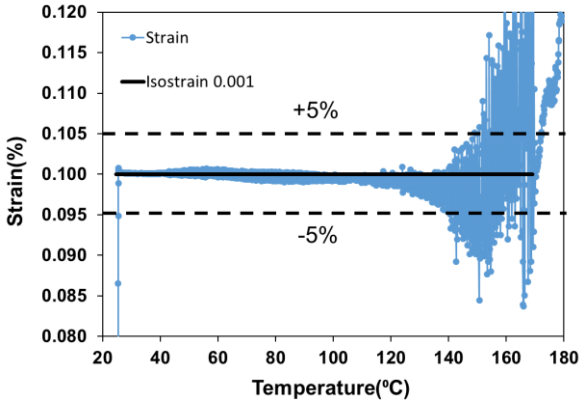

Figure 5.10 Strain variation at an iso-strain level of 0.1%.

Table 5.6 Temperature when strain variation started to become larger than ±5%

Iso-strain (%)	T (ºC) when strain variation started to become larger than ±5%
0.1	140
0.3	156

Table 5.6(cont'd)

0.9	160
2.7	162

Figure 5.11 presents the iso-strain response of Celgard® 2400 MD samples at four different strain levels. It is interesting to note that the curves in Fig. 5.11 changed the curvature with increasing temperature three times. In the range of ambient temperature < T< T_1, the stress decreased with increasing temperature. The samples were relaxed when they were heated. When T_1 < T < T_2, the stress increased with temperature. The samples tended to shrink but they were restricted by the longitudinal tensile strain. As a result, the stress built up in the samples. Finally, when T > T_2, the stress decreased again with temperature. The samples started to melt when temperature was above the melting point 162~165ºC [13,15]. At T_f, the sample fractured.

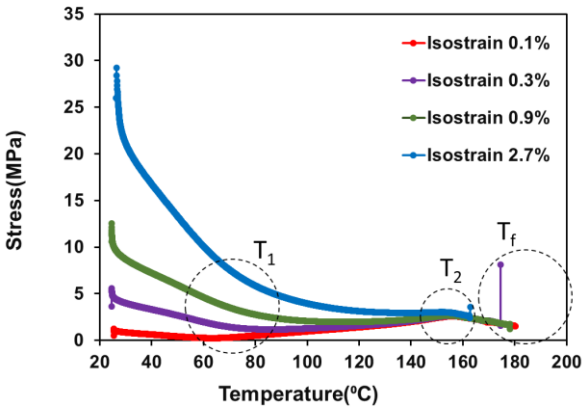

Figure 5.11 Iso-strain response of Celgard® 2400 MD samples

The effect of iso-strain level on T_1 is shown in Fig. 5.12a and b. T_1 and the corresponding stress at T_1 increased with decreasing the strain. T_1 was 64, 86, 114, 138ºC for an iso-strain at 0.1, 0.3, 0.9, 2.7%. The stresses at T_1 was in the range of 0.2 and 2.9MPa for the iso-strain levels of 0.1-2.7%.

The effect of the iso-strain level on T_2 is shown in Fig. 5.12c and d. T_2 was in the range of 156 to 152ºC while the stress at T_2 was in the range of 2.6 to 3.0MPa.

The effect of the iso-strain level on T_f were shown in Fig. 5.12 (e) and (f). T_f decreased from 180 to 162ºC while the stress at rupture increased from 1.5MPa and 2.5MPa with increasing the iso-strain. The stress at rupture was about 2±0.5MPa.

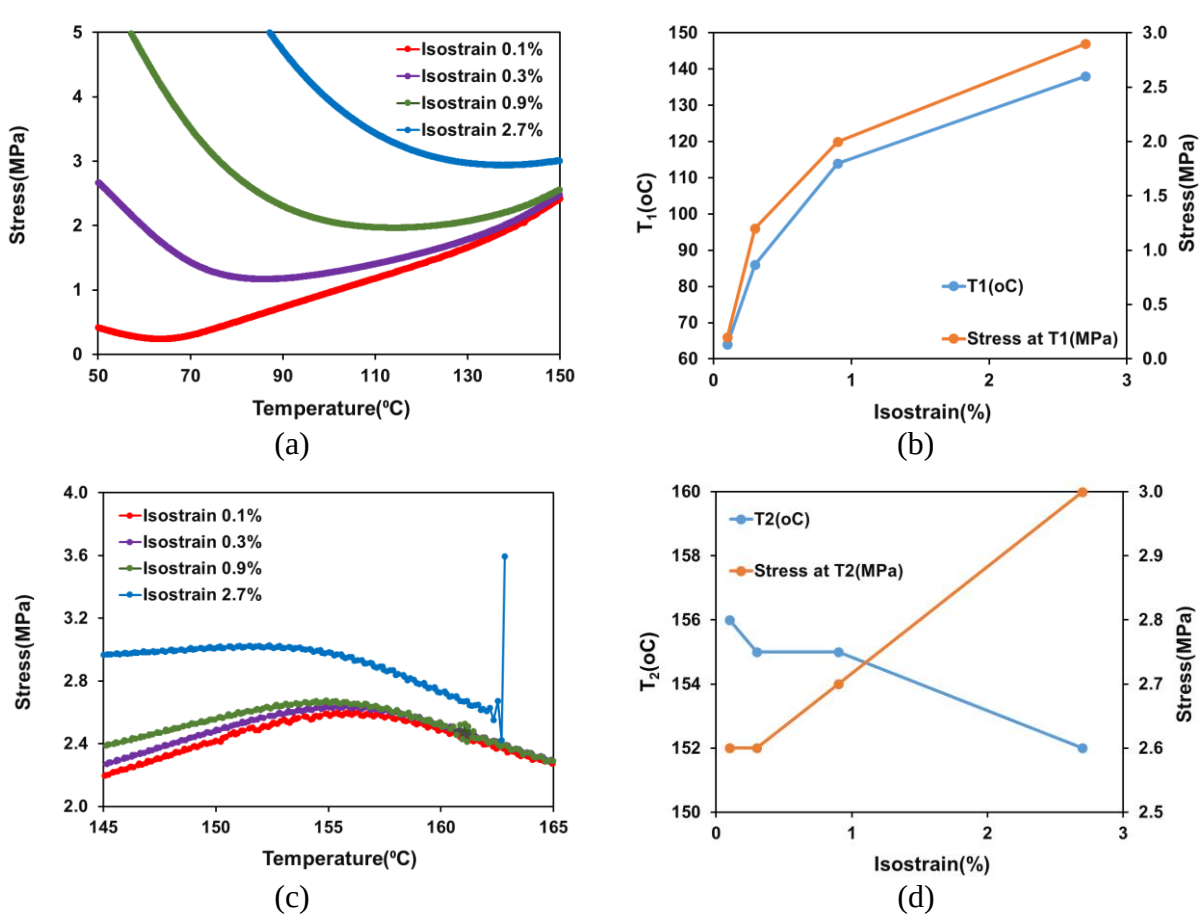

(c)

Figure 5.12 (a) Zoom in view at range of ambient temperature < T< T_1 in Figure 4.11 (b) T_1 and the stress at T_1 versus the iso-strain. (c) Zoom in view at range of T_1 < T < T_2 in Figure 4.11 (d) T_2 and the stress at T_2 vs. the iso-strain. (e) Zoom in view at range of T > T_2 in Figure 4.11 (f) T_f and the fracture stress vs. the iso-strain.

Figure 5.12(cont'd)

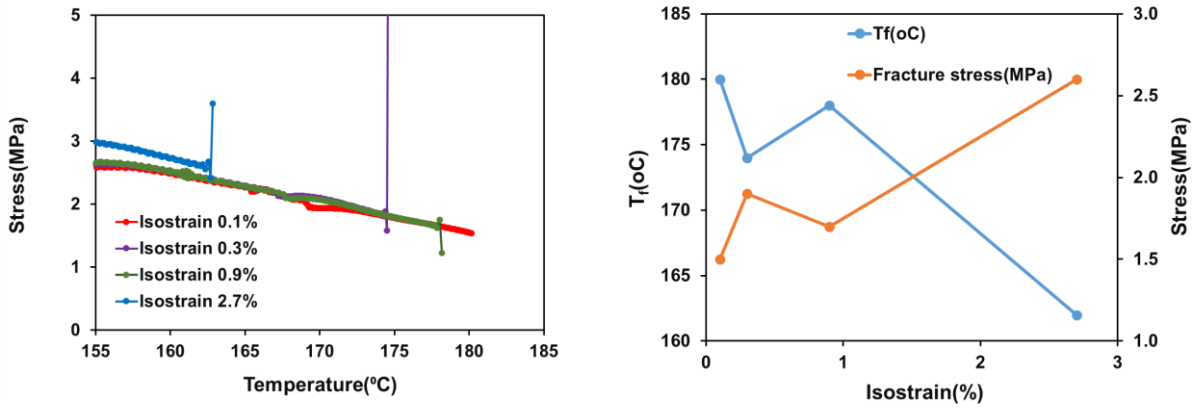

(e) (f)

5.3.2.2 The Effect of Sample Aspect Ratio

The effect of sample aspect ratio (AR) was investigated. The aspect ratio would change the stress state in the sample. For the same width, decreasing the sample length, the stress in the sample will change from uniaxial stress to become increasingly biaxial. This will have an influence on the temperature and stress at rupture. In this investigation, the samples were tested in three length/width ratios: 24mm/6mm (AR=4), 15mm/6mm (AR=2.5), and 6mm/6mm (AR=1).

Figure 5.13 (a) showed Celgard® 2400 MD sample response at an iso-strain of 0.3%. With decreasing AR, the curve was shifted horizontally to a higher temperature. The difference between the curve with AR=2.5 and AR=1 was larger than AR=4 and AR=2.5. As shown in Fig. 5.13b-d, T_1 and T_2 were ~10° C higher and T_f was ~13° C higher when AR decreased from 2.5 to 1. The stress at rupture was decreased from 1.8MPa to 1.5MPa when AR decreased from 2.5 to 1. In contrast, T_1, T_2 and T_f were only ~3° C higher when AR decreased from 4 to 2.5. The stress at rupture was the same as 1.8MPa when AR=4 and AR=2.5.

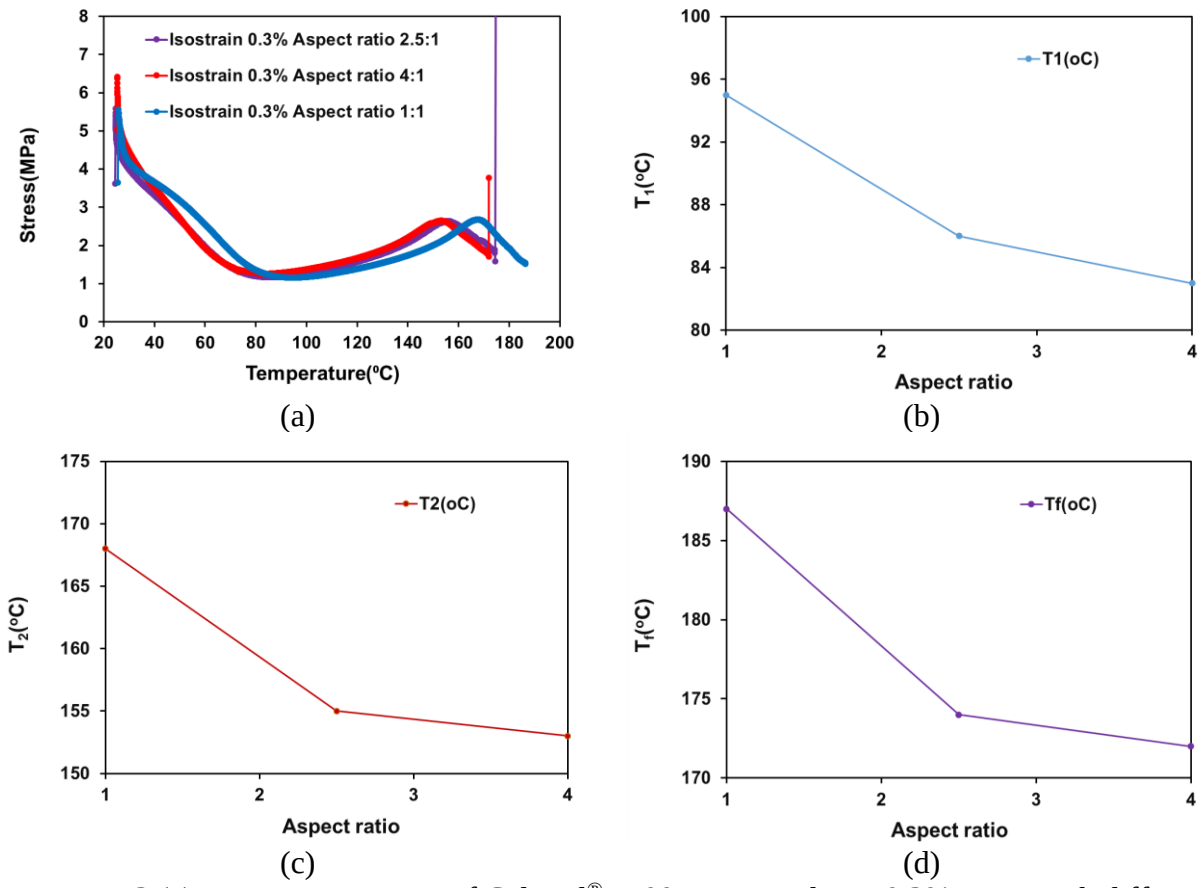

Figure 5.13 (a) Iso-strain response of Celgard® 2400 MD samples at 0.3% strain with different sample aspect ratios (AR). (b) T_1 vs. AR, (c) T_2 vs. AR, and (d) T_f vs. AR.

Sample responses at an iso-strain of 2.7% shown in Fig. 5.14 also confirmed this conclusion. T_1 and T_2 were ~10° C higher and T_f was 19° C higher when the AR decreased from 2.5 to 1. The stress at rupture was decreased from 2.6MPa to 1.8MPa when AR decreased from 2.5 to 1.

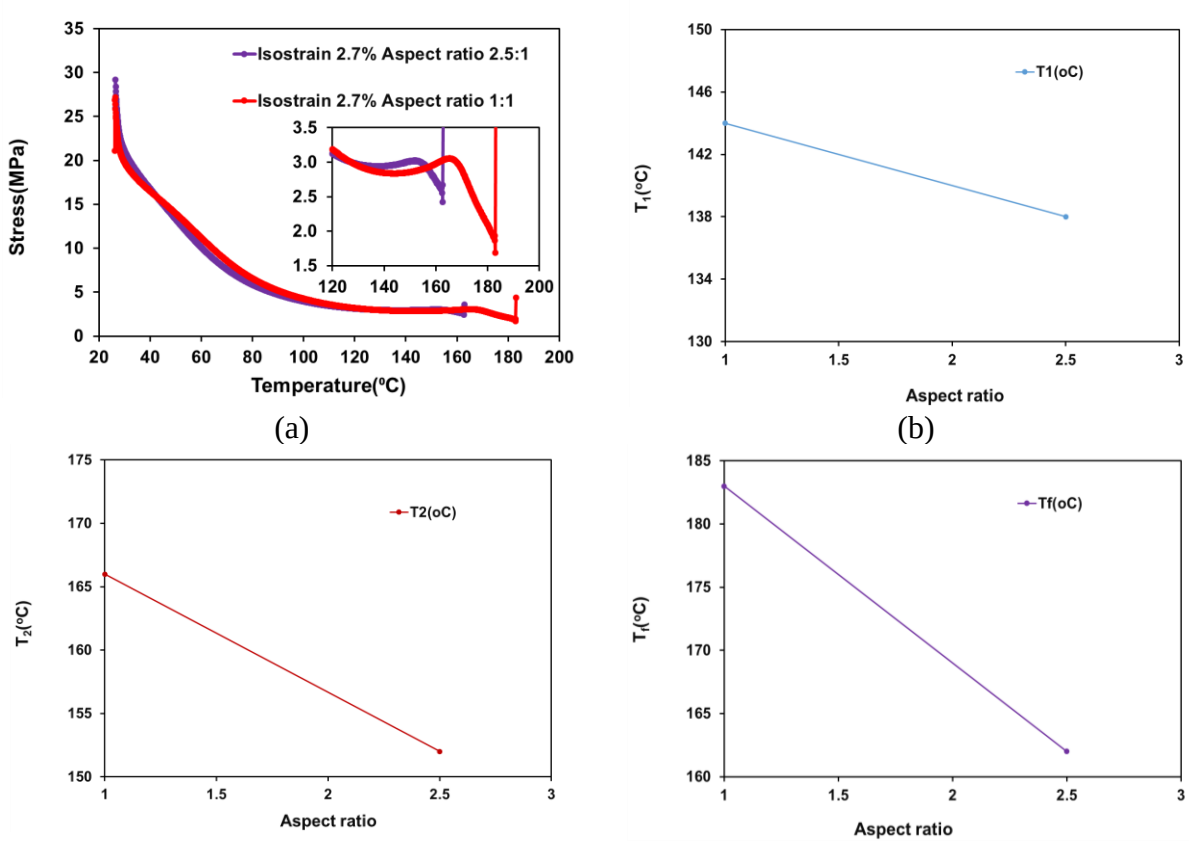

Figure 5.14 (a) Iso-strain responses of Celgard® 2400 MD samples at 2.7% strain with different ARs. (b) T_1 vs. AR, (c) T_2 vs. AR, and (d) T_f vs. AR.

5.4 Conclusions

The use of a dynamic mechanical analyzer (DMA) in the measurement of thermal expansion/shrinkage of battery separators was explored. For this measurement, it is important to perform a calibration test to determine the dimensional change of the testing fixture and to compensate for this contribution in the DMA measurement. The preloading level and heating rate were found to affect the measurement. The shrinkage data obtained from the DMA agreed well with the values obtained with an unconstrained sample under iso-thermal conditions. From the DMA results, the CTE relationships for three typical separators have been established. The DMA offers a continuous measurement in an automatic fashion. It is an efficient and convenient method to characterize the thermal expansion/shrinkage behavior of thin films.

Celgard® 2400 and 2325 have similar shrinkage behaviors. Their shrinkage in the MD is much higher than that in the TD. Q20S1HX shows more isotropic shrinkage behavior. For all three separators, the necking/fracture temperatures of the TD samples were 15ºC ~35ºC lower than the MD samples.

The response of Celgard® 2400 MD under the iso-train mode has also investigated. For iso-strain levels of 0.1 to 2.7%, the stress at rupture was about 2±0.5MPa.

APPENDICES

APPENDIX A Repeated tests of the measured expansion/shrinkage strain

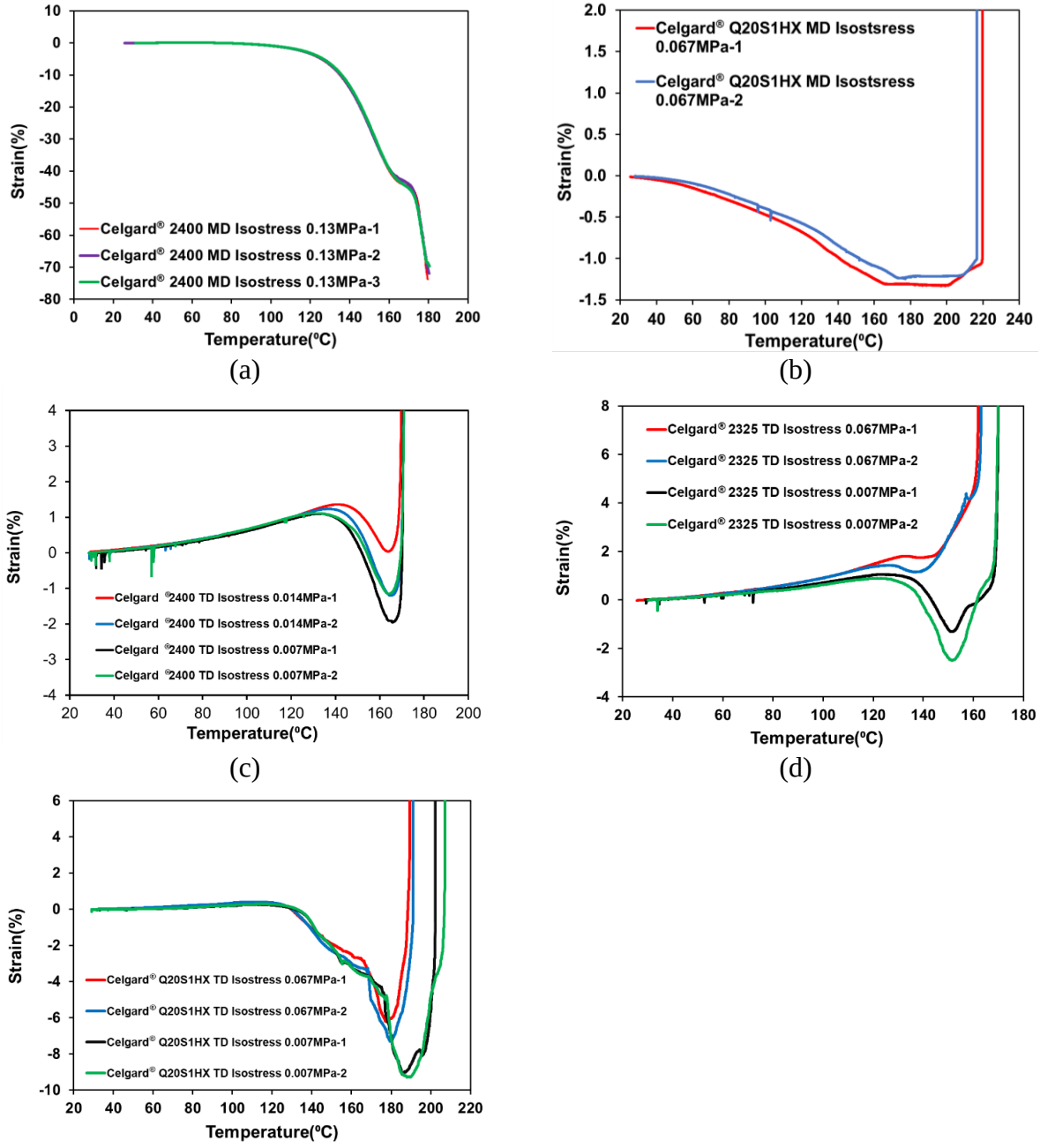

Figure A.5 Repeated tests of the measured expansion/shrinkage strain under different stress levels at 3°C/min for (a) Celgard® 2400 MD, (b) Celgard® Q20S1HX MD, (c) Celgard® 2400 TD, (d) Celgard® 2325 TD, (e) Celgard® Q20S1HX TD.

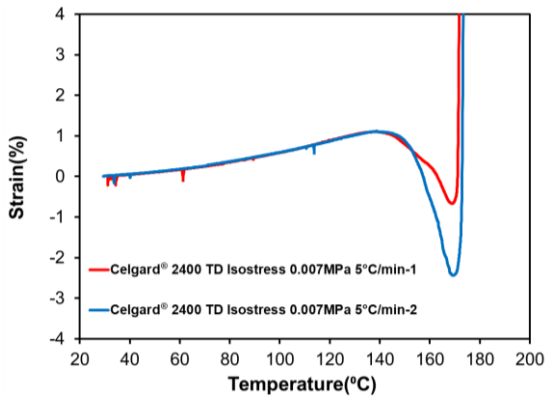

(a)

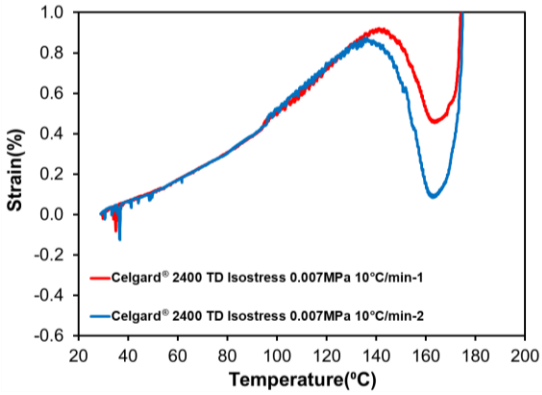

(b)

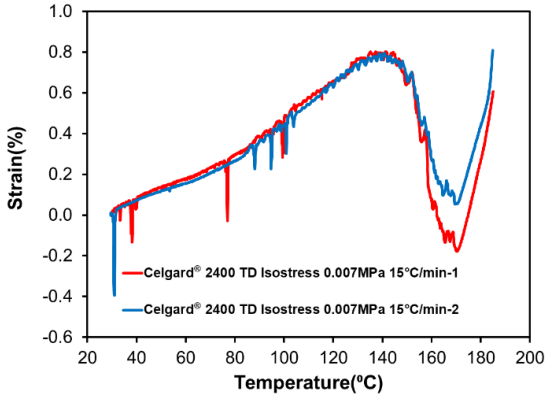

(c)

Figure A.6 Repeated tests of the measured expansion/shrinkage strain under 0.007MPa for Celgard® 2400 TD (a) 5°C/min, (b) 10°C/min, (c) 15°C/min.

APPENDIX B Raw data and calibrated data for the measured expansion/shrinkage strain

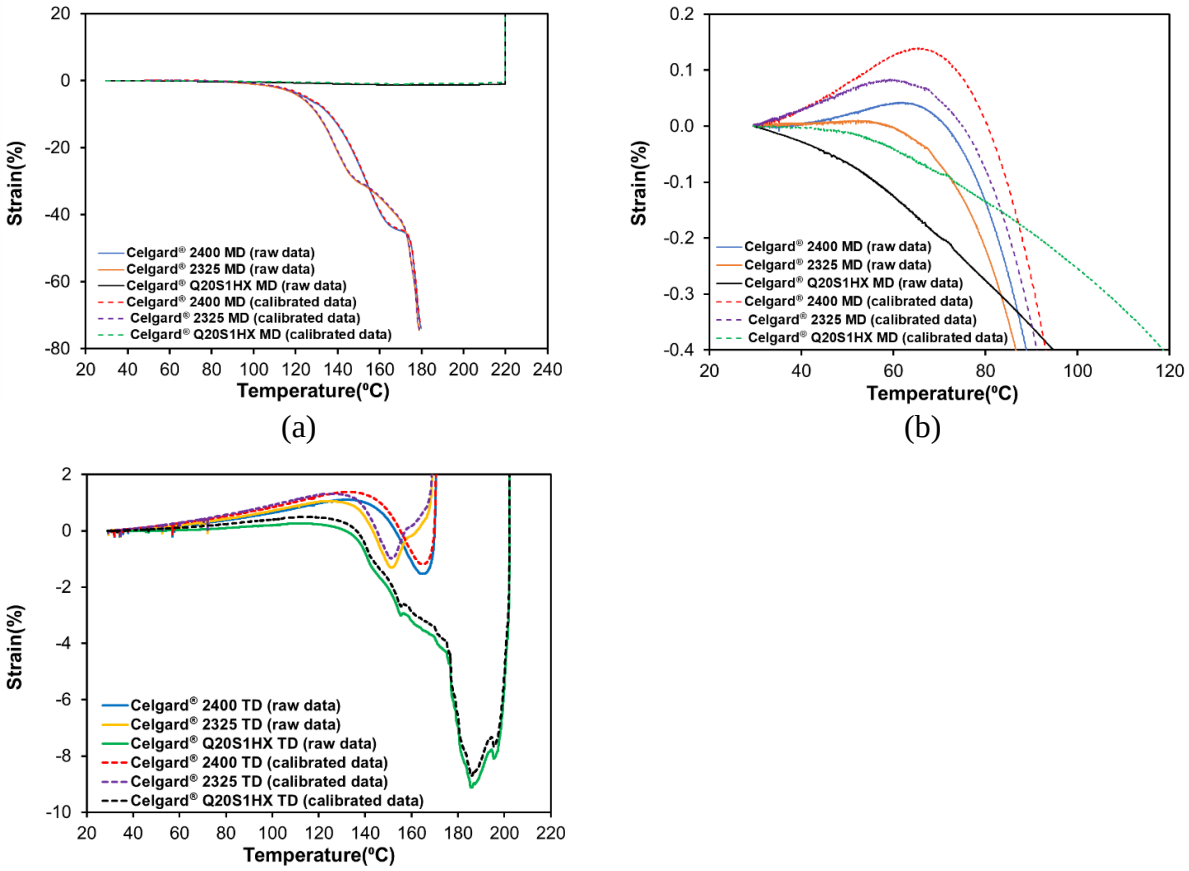

Figure B.2 Raw data and calibrated data for expansion/shrinkage strain of three types of separators, (a) the MD samples, (b) the MD samples from 20-120°C, (c) the TD samples.

APPENDIX C Determination of CTE for Celgard® 2400 TD, 2325 MD and TD and Q20S1HX MD and TD

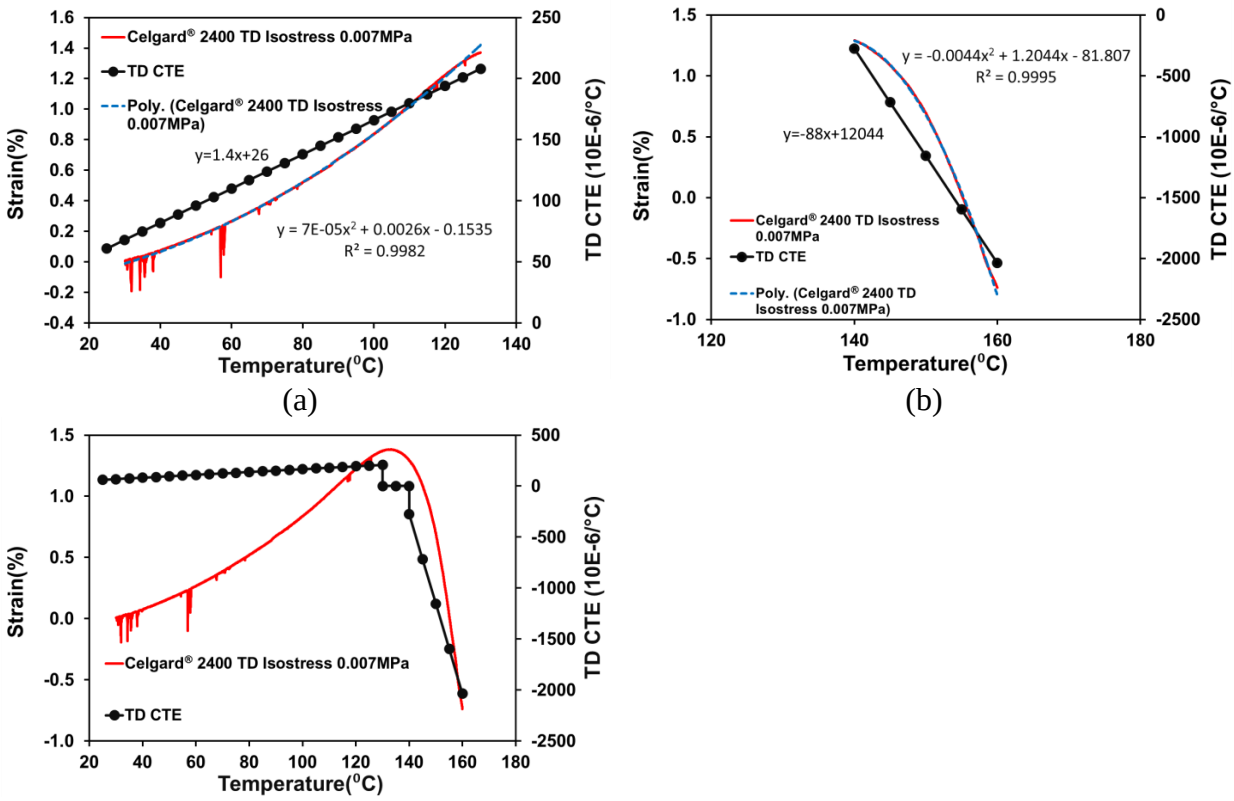

Figure C.1 Determine the CTE of Celgard® 2400 TD. (a) The first segment, (b) the second segment, and (c) the combined curve.

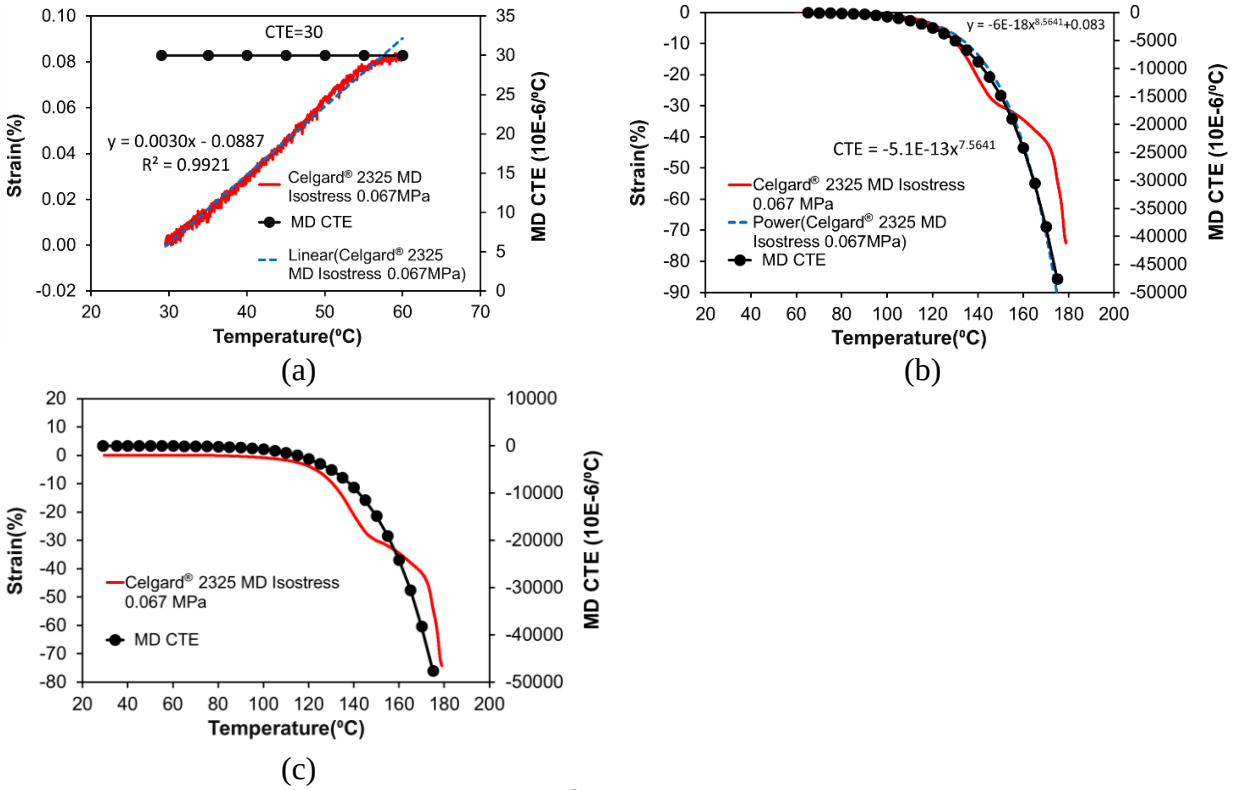

Figure C.2 Determine the CTE of Celgard® 2325 MD. (a) The first segment, (b) the second segment, and (c) the combined curve.

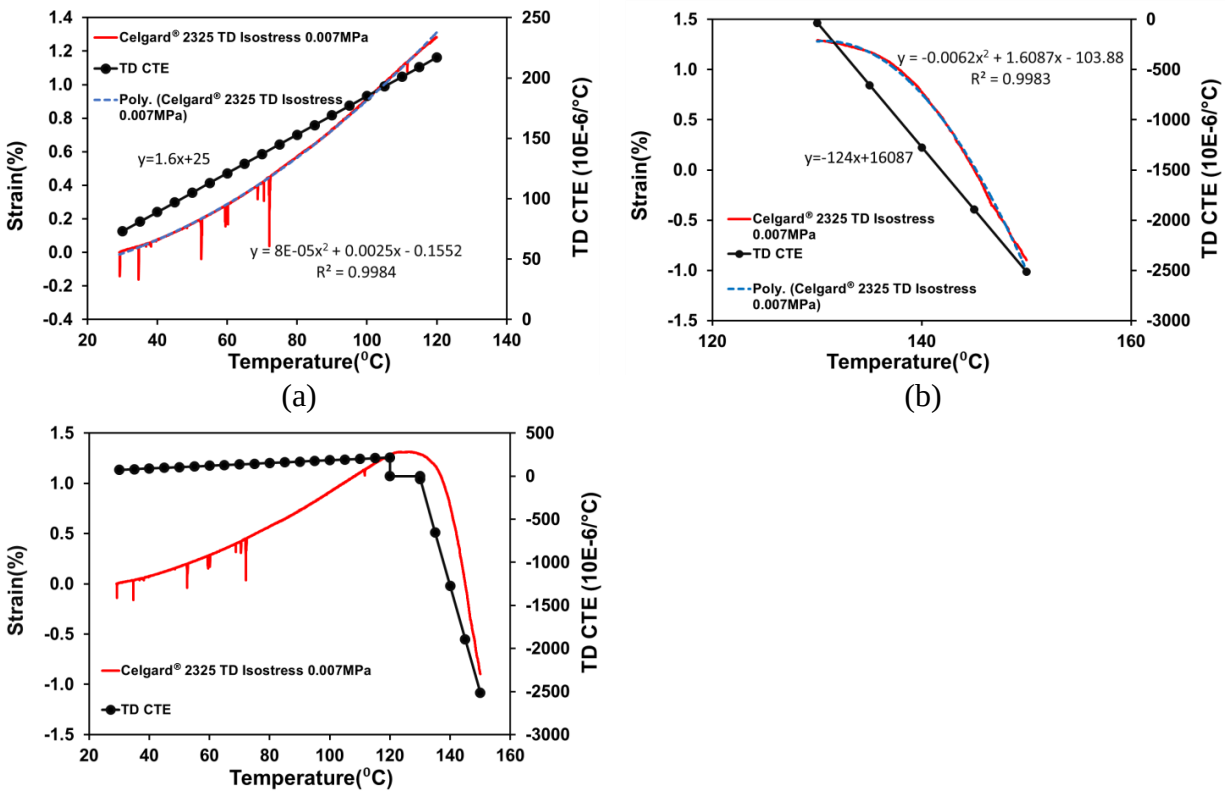

Figure C.3 Determine the CTE of Celgard® 2325 TD. (a) The first segment, (b) the second segment, and (c) the combined curve.

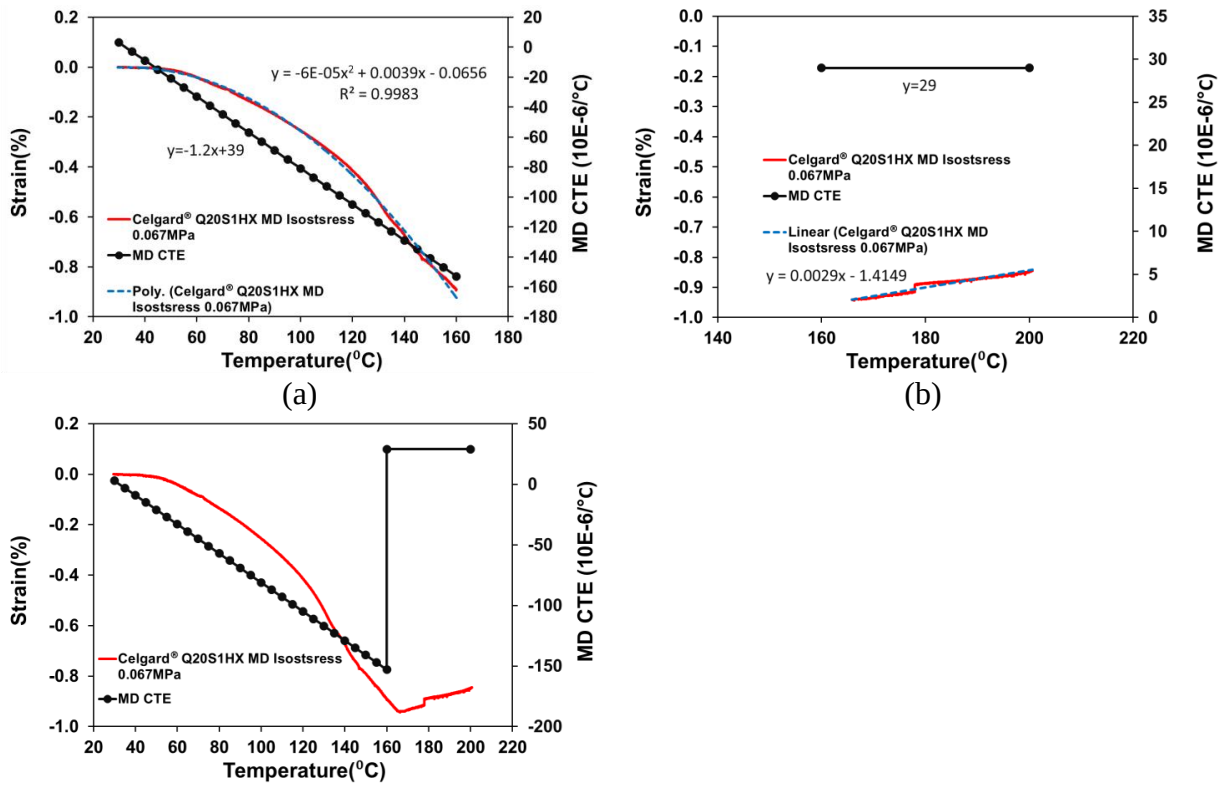

Figure C.4 Determine the CTE of Celgard® Q20S1HX MD. (a) The first segment, (b) the second segment, and (c) the combined curve.

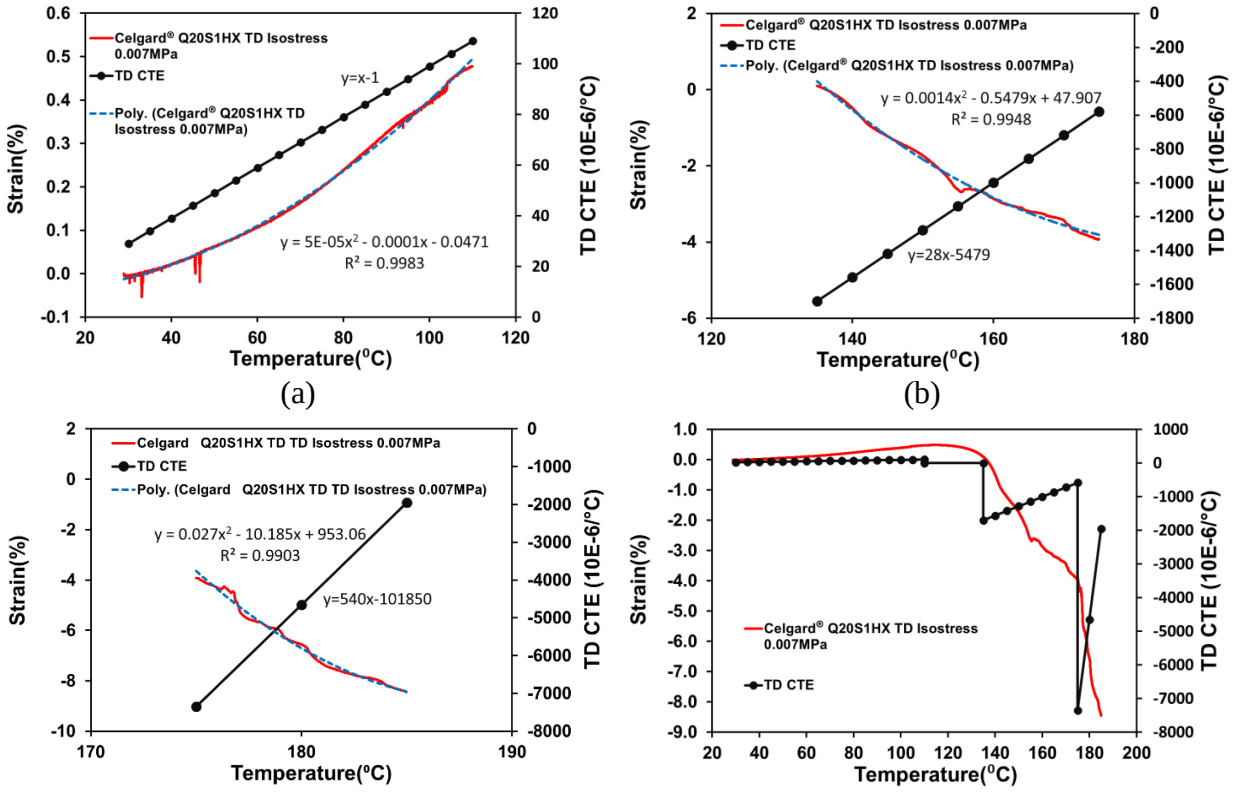

Figure C.5 Determine the CTE of Celgard® Q20S1HX TD. (a) The first segment, (b) the second segment, and (c) the third segment, (d) the combined curve.

REFERENCES

REFERENCES

1. P. Hidnert and H. S. Krider, Thermal Expansion of Aluminum and Some Aluminum Alloys, Journal of Research of the National Bureau of Standards, 48 (1952) 209-220.

2. TA Instruments, Dynamic Mechanical Analyzers: How Do They Work? http://www.tainstruments.com/pdf/literature/TA229.pdf (accessed June 18, 2018)

3. S.Yan, Y. He, A. Asta, J. Deng, C. Bae, X. Xiao, Characterization of the in-plane orthotropic viscoelastic property of a polymeric battery separator, Polymer Testing, 72 (2018) 46-54.

4. PerkinElmer, Inc., Expansion Coefficient of Polymeric Materials using DMA 8000, Waltham, 2007.

5. S.J. Bennett, The thermal expansion of copper between 300 and 700 K, Journal of Physics D: Applied Physics, 11 (1978) 777-780.

6. TA Instruments, Dynamic Mechanical Analyzer, Operator's Manual, New Castle, 2002.

7. W. Sun, A.P. Vassilopoulos, T. Keller, Effect of thermal lag on glass transition temperature of polymers measured by DMA, International Journal of Adhesion & Adhesives, 52 (2014) 31–39.

8. R.S. Baldwin, W.R. Bennet, E.K. Wong, M.R. Lewton, M.K. Harris, Battery Separator Characterization and Evaluation Procedures for NASA's Advanced Lithium-Ion Batteries, NASA/TM-2010-216099.

9. C. Shi, J. Dai, X. Shen, L. Peng, C. Li, X. Wang, P. Zhang, J. Zhao, A high-temperature stable ceramic-coated separator prepared with polyimide binder/Al2O3 particles for lithium-ion batteries, Journal of Membrane Science, 517 (2016) 91–99.

10. J. Song, M. H. Ryou, B. Son, J.N. Lee, D.J. Lee, Y.M. Lee, J.W. Choi, J.K. Park, Co-polyimide-coated polyethylene separators for enhanced thermal stability of lithium ion batteries, Electrochimica Acta, 85 (2012) 524–530.

11. J. Li, Q. Zhong, Y. Yao, S. Bi, T. Zhou, X. Guo, M. Wu, T. Feng, R. Xiang, Electrochemical performance and thermal stability of the electrospun PTFE nanofiber separator for lithium-ion batteries, Journal of Applied Polymer Science, 135 (2018) 46508.

12. Y. Li, H. Pu, Y. Wei, Polypropylene/polyethylene multilayer separators with enhanced thermal stability for lithium-ion battery via multilayer coextrusion, Electrochimica Acta, 264 (2018) 140–149.

13. P. Arora, Z.M. Zhang, Battery Separators, Chemical Reviews, 104 (2004) 4419–4462.

14. B. Xiong, R. Chen, F. Zeng, J. Kang, Y. Men, Thermal shrinkage and microscopic shutdown mechanism of polypropylene separator for lithium-ion battery: In-situ ultra-small angle X-ray scattering study, Journal of Membrane Science, 545 (2018) 213–220.

15. C.T, Love, Thermomechanical analysis and durability of commercial micro-porous polymer Li-ion battery separators, Journal of Power Sources, 196 (2011) 2905–2912.

CHAPTER 6 THERMAL VISCOELASTIC CHARACTERIZATION

6.1 Introduction

The temperature dependence of the polymeric separator's mechanical properties is of great concern. The time-temperature dependence of viscoelastic solids can be modeled based on the framework of the time-temperature superposition principle (TTSP) of the linear viscoelasticity theory [1]. According to TTSP, the temperature effect is equivalent to a time shift in the relaxation spectra. The effect of temperature can be included in a viscoelastic function through the use of a reduced time $t'=t/a_T$ where a_T is the shift factor.

In this Chapter the creep tests has carried out from room temperature up to 60°C. At this temperature range, both Celgard® 2400 MD and TD sample expands while MD sample starts to shrink as shown in Chapter 5. A master curve is contructed by superposing individual plot of different temperatures along log-time axis. The amount of horizontal shift required for these curves to form the master curve yielded the time-temperature shifting function a_T.

6.2 Experimental

The creep tests are performed within the temperature range from 25°C to 60°C, which is the common range for a battery in the working situation [2,3]. The testing temperatures are chosen as 25°C, 40°C, 45°C, 50°C, 55°C and 60°C. All creep tests are performed in dry condition/in air.

Creep tests were carried out using a DMA Q800 under a tensile mode with a film clamp as shown in Fig. 5.1a. The clamp had a fixed gage length 15 mm. The samples Celgard® 2400 were cut along MD in the form of long strips with nominal width 5mm.

Individual creep test was performed following a three-step procedure: (1) the isothermal environment was established by accommodating the clamp and film in a closed furnace as shown

in Fig. 5.1b. (2) The temperature was increased from the ambient temperature to the specified testing temperature with a ramp rate 4°C/min. After reaching the testing temperature, the sample was allowed to be held isothermally for 5 minutes. Since the thickness of Celgard® 2400 is only 25 μm, an isothermal heating time of 5 minutes was sufficient for the sample to reach equilibrium. (3) The sample was then subjected to a specified constant load for 20 minutes and the sample length change was monitored.

6.3 Results

Firstly, the stress level of the linear creep response was determined. For linear viscoelastic behavior, the creep compliance is independent of the stress level [4]. Figure 6.1a presents the creep compliance curves at 60°C at 1 MPa, 1.5 MPa, 1.75 MPa and 2 MPa. A new sample was tested under each stress. The curves at 1 MPa and 1.5 MPa overlap together, indicating that the creep response is linear at 1.5 MPa. The curves for 1.75 MPa and 2 MPa are higher, showing the tendency to nonlinear viscoelasticity. Therefore testing at a stress level of 1.5 MPa for temperature up to 60°C will ensure a linear creep response.

Next, creep tests were conducted at each testing temperature at 1.5 MPa. A new sample was tested at each temperature. Figure 6.1b presents the creep compliance curves. The creep compliance curves were converted to the stress relaxation curves by Laplace transformation [1,4] and plotted versus logarithmic time in Fig. 6.1c. A master curve was constructed by horizontally shifting the curves until they coincide, using the curve at 25°C as the reference curve. The amount of horizontal shift required for these curves to form the master curve yielded the time-temperature shifting function a_T, as shown in Fig. 6.1d. a_T will be further included in viscoelastic function to account for the temperature effect as

$$G(t) = G_0 + \sum_{i=1}^{n} G_i \, exp\left(-\frac{t}{a_T \tau_i}\right) \tag{6.1}$$

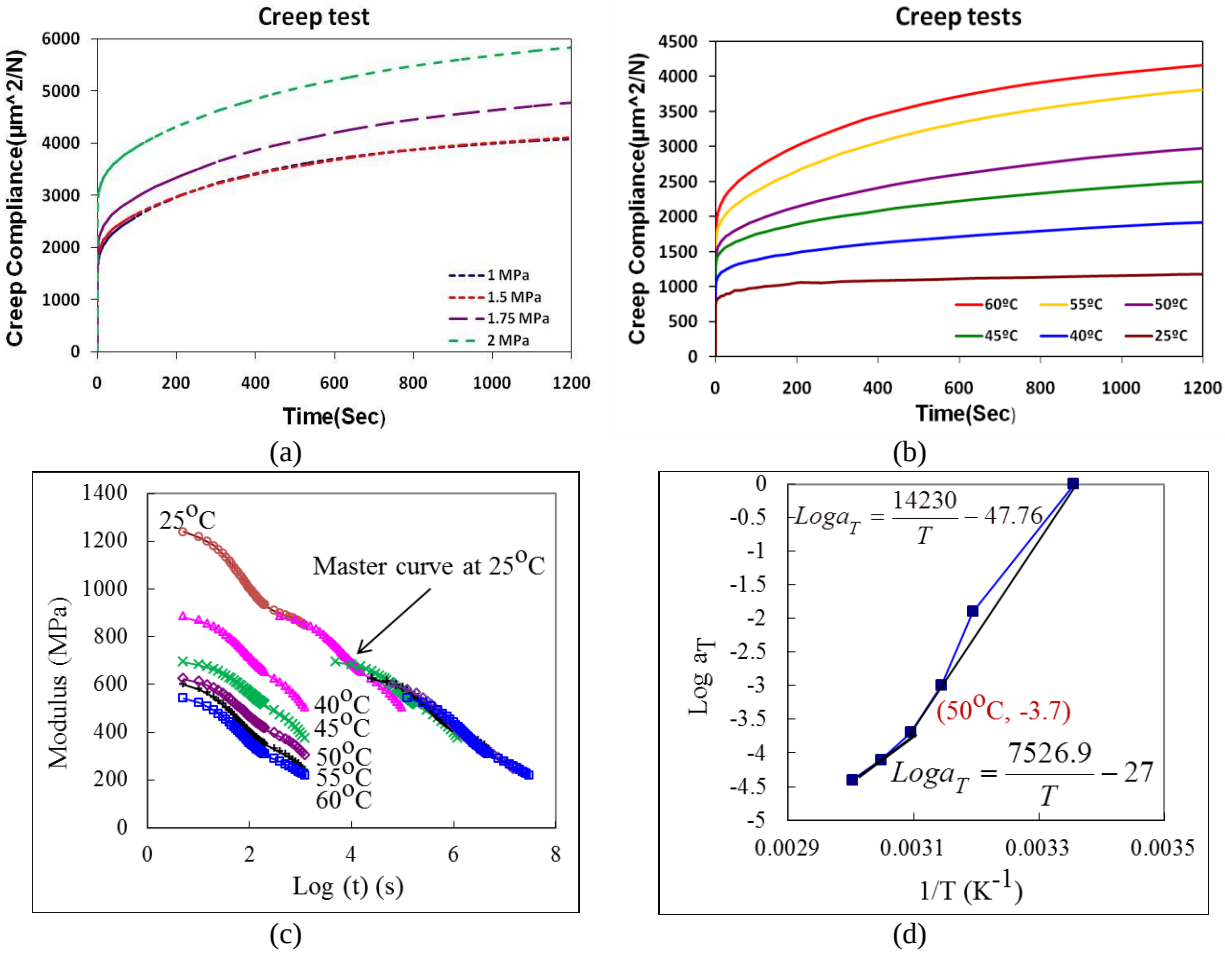

Figure 6.1 (a) Creep compliance curves at 60°C at 1 MPa, 1.5 MPa, 1.75 MPa and 2 MPa. (b) Creep compliance curves at different tempretures under stress 1.5 MPa. (c) Construction of a master curve using stress relaxation curves at different temperatures. The stress relaxation curves are obtained from creep compliance curves by Laplace transformation [5] (d) Time-temperature shift function a_T [5]

6.4 Conclusion

Creep tests of MD sample have been carried out from room temperature up to shrink at 60°C. A master curve has been constructed by superposing individual creep of different temperatures along log-time axis, using creep as 25°C as reference. The time-temperature shifting

function a_T is obtained from the amount of horizontal shift required for these curves to form the master curve.

REFERENCES

REFERENCES

1. I.M. Ward, J. Sweeney, An Introduction to the Mechanical Properties of Solid Polymers, 2 edition, Wiley, Chichester, West Sussex, England, 2004.

2. W. Wu, X. Xiao, X. Huang, The effect of battery design parameters on heat generation and utilization in a Li-ion cell, Electrochimica Acta, 83 (2012) 227–240.

3. X. Zhang, Mechanical Behavior of Shell Casing and Separator of Lithium-ion Battery (Doctoral dissertation), Massachusetts Institute of Technology, 2017.

4. A. Sheidaei, X. Xiao, X. Huang, J. Hitt, Mechanical behavior of a battery separator in electrolyte solutions, Journal of Power Sources, 196 (2011) 8728–8734.

5. W. Wu, A Multiphysics Model for the Stress Analysis of the Separator In a Lithium-Ion Battery(Doctoral dissertation), Michigan State University, 2013.

CHAPTER 7 ORTHOTROPIC VISCOELASTIC MODELING

7.1 Introduction

An orthotropic viscoelastic model has been implemented in LS-DYNA®. A discretization algorithm is developed to evaluate stiffness-based hereditary integral with a kernel of Prony series. The model is verified with existing isotropic viscoelastic model and orthotropic elastic model in LS-DYNA® uniaxial loading conditions and examined for biaxial loading condition.

7.2 Model Implementation in LS-DYNA®

The stress-strain behavior of a linear viscoelastic material is described as [1,2]

$$\sigma(t) = \int_0^t G(t-t')\frac{d\varepsilon}{dt'}dt' \tag{7.1}$$

where G(t) is the relaxation stiffness matrix. G(t) is a required input in model in LS-DYNA® because the models in LS-DYNA® are stiffness based.

Under plane stress condition $\boldsymbol{\sigma} = \begin{bmatrix}\sigma_1(\mathrm{t})\\ \sigma_2(\mathrm{t})\\ \tau(\mathrm{t})\end{bmatrix}$, $\boldsymbol{\varepsilon} = \begin{bmatrix}\varepsilon_1(\mathrm{t})\\ \varepsilon_2(\mathrm{t})\\ \gamma(\mathrm{t})\end{bmatrix}$, $\boldsymbol{G}(\mathrm{t})$ is the relaxation modulus matrix

$$[\boldsymbol{G}(t)] = \begin{bmatrix} G'_{11}(t) & G'_{12}(t) & 0 \\ G'_{12}(t) & G'_{22}(t) & 0 \\ 0 & 0 & G'_{44}(t) \end{bmatrix} \tag{7.2}$$

Each components of the stiffness matrix are often expressed by Prony series

$$G(t) = G_\infty + \sum_{i=1}^{n} G_i \, exp(-t/\tau_i) \tag{7.3}$$

where G_∞ is fully relaxed modulus, G_i is stress relaxation constant and τ_i is relaxation time.

The main challenge in implementing the viscoelastic model into LS-DYNA® is the evaluation of the hereditary integral. Eq. 7.1 shows that the stress relaxation depends on the time elapsed for the strain increment at each time step. For a process with an arbitrarily varying stress strain history, a direct evaluation of the hereditary integral would require to store the strain increment at each time step. This algorithm is prohibitive expensive.

7.2.1 Discretization Algorithm of Hereditary Integral With a Kernel of Prony Series

Puso and Weiss [3] presented an algorithm for the evaluation of hereditary integral with a single exponential function as its kernel. This starts from the analysis of Eq. 7.1. At time t+Δt, Eq. 7.1 becomes

$$\sigma(t+\Delta t) = \int_0^{t+\Delta t} G(t+\Delta t - t')\frac{d\epsilon}{dt'}dt' \tag{7.4}$$

Eq. 7.4 can be separated into two terms

$$\sigma(t+\Delta t) = \int_0^{t} G(t+\Delta t - t')\frac{d\epsilon}{dt'}dt' + \int_t^{t+\Delta t} G(t+\Delta t - t')\frac{d\epsilon}{dt'}dt \tag{7.5}$$

where each term will be evaluated separately. The 2nd term on the right hand side of the Eq. 7.5 can be solved approximately as using the Mean Value Theorem when Δ*t* is very small:

$$\int_t^{t+\Delta t} G(t+\Delta t - t')\frac{d\epsilon}{dt'}dt' = \frac{\varepsilon_{t+\Delta t}-\varepsilon_t}{\Delta t}\int_t^{t+\Delta t} G(t+\Delta t - t')\,dt' = \frac{\varepsilon_{t+\Delta t}-\varepsilon_t}{\Delta t}G(\Delta t)\Delta t \tag{7.6}$$

To evaluate the 1st term in Eq. 7.5, a specific kernel function has to be defined. Assuming *G*(*t*) is a single term exponential function

$$G(t) = C_1 exp\left(-\frac{t}{\tau}\right) \tag{7.7}$$

The 1st term becomes

$$\int_0^t G(t+\Delta t-t')\frac{d\varepsilon}{dt'}dt' = \int_0^t C_1 \exp\left(-\frac{t+\Delta t-t'}{\tau}\right)\frac{d\varepsilon}{dt'}dt' =$$

$$\exp\left(-\frac{\Delta t}{\tau}\right)\int_0^t C_1 \exp\left(-\frac{t-t'}{\tau}\right)\frac{d\varepsilon}{dt'}dt' = \exp\left(-\frac{\Delta t}{\tau}\right)\sigma(t) \tag{7.8}$$

The significance of Eq. 7.8 is that to evaluate the hereditary integral at t+Δt, we only need to know the stress at the previous time step. Based on this mathematical derivation, a discretization algorithm for the evaluation of hereditary integral with a kernel of a single exponential function was developed [3].

A single exponential function is insufficient to represent the relaxation stiffness over a broad time spectrum. To extend the algorithm to hereditary integral with Prony series, we examine the generalized Maxwell model in Fig. 7.1, which is the physical representation of Eq. 7.3. It shows that the total stress in the material is contributed by the long term relaxation stress σ_∞ and n individual Maxwell components, each with its characteristic relaxation time τ_i ($i=1,2, \ldots n$). If the stress with each component is known, the total stress will be

$$\sigma(t) = \sigma_\infty + \sum_{i=1}^{n} \sigma^i(t) \tag{7.9}$$

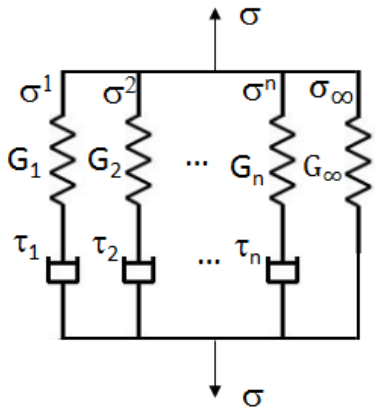

Figure 7.1 The generalized Maxwell model

Following the same mathematical operation as in Eq. 7.8, the 1st term of Eq. 7.5 is derived for a kernel of Prony series as

$$\int_0^t G(t+\Delta t-t')\frac{d\varepsilon}{dt'}dt$$

$$= \sigma_\infty + \sum_{i=1}^{n} \exp\left(-\frac{\Delta t}{\tau_i}\right)\int_0^t G_i exp\left(-\frac{t-t'}{\tau_i}\right)\frac{d\varepsilon}{dt'}dt' = \sigma_\infty + \sum_{i=1}^{n} \exp\left(-\frac{\Delta t}{\tau_i}\right)\sigma^i(t)$$

(7.10)

The evaluation of Eq. 7.10 requires the stress value in each Maxwell component in the previous step. As the Prony series contains a limited number of terms, the required storage can be easily managed.

Figure 7.2 presents the model implementation flowchart. The algorithm script is written in FORTRAN language and integrated with LS-DYNA®. At certain timestep, LS-DYNA® provides strain increment and time increment with the user to calculate the stress increment at current time step. Firstly, the elastic stress increment is calculated. Next, the stress increment after relaxation is calculated using Eq. 7.6 and 7.8. Only history variables of stress at the previous time step are needed to calculate the stress increment at the current time step. Then the calculated stresses at current time step are updated for the stress calculation in next time step. This iteration procedure is repeated at each time step till the end.

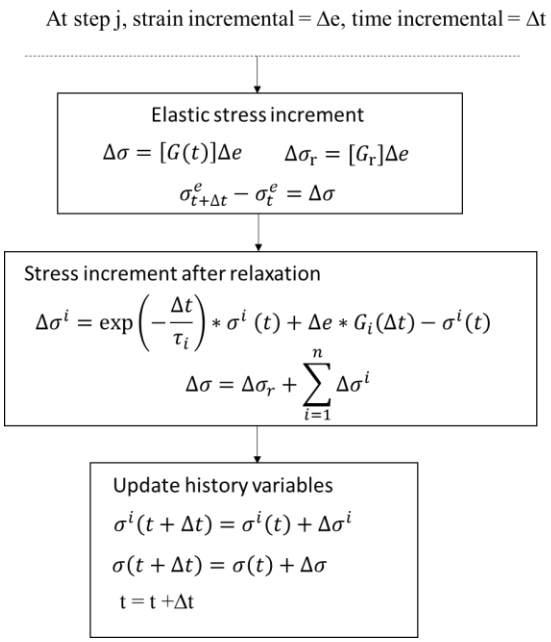

Figure 7.2 Model implementation flowchart

7.2.2 Relaxation Stiffness Matrix

7.2.2.1 Isotropic Material for Plane Stress Situation

$$[\boldsymbol{G}(t)] = \frac{1}{1-\nu^2}\begin{bmatrix} G(t) & \nu G(t) & 0 \\ \nu G(t) & G(t) & 0 \\ 0 & 0 & \frac{1}{2}(1-\nu)G(t) \end{bmatrix} \tag{7.11}$$

Each hereditary integral is evaluated separately.

[$\boldsymbol{G}(t)$] is derived from [4]

$$\boldsymbol{\sigma} = \int_0^t \boldsymbol{K}(t-s)\frac{d\boldsymbol{\varepsilon}^{\mathbf{vol}}}{ds}ds \; + 2\int_0^t \boldsymbol{\mu}(t-s)\frac{d\boldsymbol{\varepsilon}^{\mathbf{dev}}}{ds}ds \tag{7.12}$$

where $\boldsymbol{\varepsilon}^{\mathrm{vol}}$ is the volumetric component of strain as $\boldsymbol{\varepsilon}^{\mathbf{vol}} = \begin{bmatrix} \varepsilon_1(t) + \varepsilon_2(t) + \varepsilon_3(t) \\ \varepsilon_1(t) + \varepsilon_2(t) + \varepsilon_3(t) \\ 0 \end{bmatrix}$,

$\boldsymbol{\varepsilon}^{\mathbf{dev}}$ is the deviatoric component of strain as $\boldsymbol{\varepsilon}^{\mathbf{dev}} = \begin{bmatrix} \varepsilon_1(t) \\ \varepsilon_2(t) \\ \frac{1}{2}\gamma(t) \end{bmatrix} - \frac{1}{3}\begin{bmatrix} \varepsilon_1(t) + \varepsilon_2(t) + \varepsilon_3(t) \\ \varepsilon_1(t) + \varepsilon_2(t) + \varepsilon_3(t) \\ 0 \end{bmatrix}$,

and out-of-plane strain $\varepsilon_3(t) = -\frac{\nu}{1-\nu}(\varepsilon_1(t) + \varepsilon_2(t))$.

Assuming Poisson's ratio *v* is time independent, volumetric and deviatoric parts of the stress are assumed to follow same relaxation behavior [5]. Bulk relaxation modulus is calculated as $K(t) = \frac{G(t)}{3(1-2\nu)}$ while shear relaxation modulus is calculated as $\mu(t) = \frac{G(t)}{2(1+\nu)}$.

7.2.2.2 Transverse Orthotropic Material for Plane Stress Situation

$$[\boldsymbol{G}(t)] = \frac{1}{1-\nu_{12}\nu_{21}}\begin{bmatrix} G_{11}(t) & \nu_{12}G_{22}(t) & 0 \\ \nu_{12}G_{22}(t) & G_{22}(t) & 0 \\ 0 & 0 & (1-\nu_{12}\nu_{21})\,G_{66}(t) \end{bmatrix} \tag{7.13}$$

There are four independent material properties need to be characterized $G_{11}(t)$, $G_{22}(t)$, $G_{44}(t)$ and ν_{12} [6]. Poisson's ratio ν_{12} is assumed to be time independent. ν_{21} is calculated as $\nu_{21} = \nu_{12} \times \frac{G_{22}(t)}{G_{11}(t)}$, which is similar to the relationship $\nu_{21} = \nu_{12} \times \frac{E_2}{E_1}$ [6].

7.2.2.3 Transverse Orthotropic Material for Complex Loading Situation

In the situation where out-of-plane shear is involved, e.g. bending, the out-of-plane shear stress is calculated as

$$\sigma_{13}(t) = \int_0^t G_{13}(t-t')\frac{d\gamma_{13}}{dt'}dt' \tag{7.14}$$

$$\sigma_{23}(t) = \int_0^t G_{23}(t-t')\frac{d\gamma_{23}}{dt'}dt' \tag{7.15}$$

where $G_{13}(t)$=$G_{12}(t)$ and $G_{23}(t) = \frac{G_2(t)}{2(1+\nu_{23})}$.

7.3 Simulation Details

7.3.1 One Element Uniaxial Tensile test

As the first step, the model is validated in the uniaxial loading situation. Shell element is used in all simulations because the thickness of sample is much smaller than the in-plane dimension. Belytschko-Tsay element formulation is used. For simplicity, one square shell element is used as the sample in the simulation. The shell element in blue square with its node numbers and coordinate system is shown in Fig. 7.3. The length of the shell element L_C is 6mm. The displacement or force is applied on node #3 and #4: Node #1 is fully constrained while node #2 is allowed to move in x direction but constrained in y direction. Node #3 is constrained in x direction but allowed to move in y direction. Node #4 is free to move in both directions. Five uniaxial loadings are used as stress relaxation in Fig. 7.4a, creep in Fig. 7.4b, creep test with two steps in Fig. 7.4c&d and tensile test at different force ramp rates.

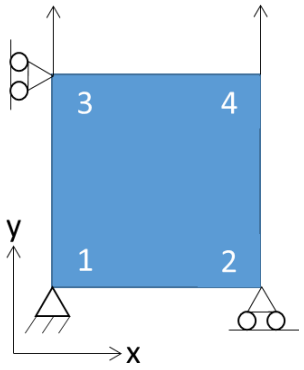

Figure 7.3. Shell element with boundary conditions and loadings under uniaxial stress state

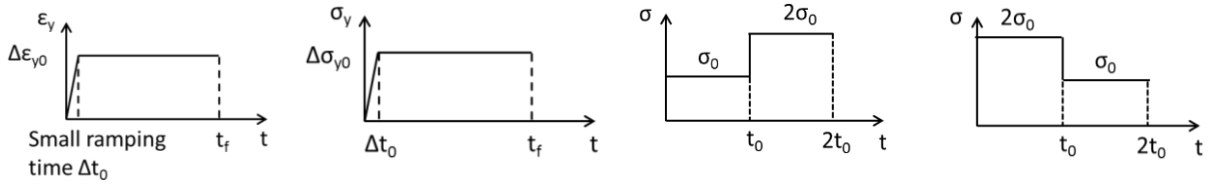

(a) (b) (c) (d)

Figure 7.4 Uniaxial loadings (a) Stress relaxation (b) Creep (c) Creep test with two steps (case 1): low-high stress. (d) Creep tests with two steps (case 2): high-low stress.

7.3.2 Biaxial Punch Test

The orthotropic model also needs to be validated in biaxial loading situation. Biaxial loading can be introduced in several ways, like uniaxial tensile test of a sample with a hole, uniaxial tensile test of a sample with short length, biaxial tensile test, biaxial punch test [7-10] etc. Among them, the biaxial punch test is better representing the out-of-plane deformation of an electric vehicle battery during crash event [10].

Biaxial punch test in [10] is simulated. The size and the mesh of punch and sample is shown in Fig. 7.5. Element formulation #16 fully integrated shell element is used for the separator. The nodes on the perimeter of the sample were constrained in all directions. The punch was treated as a rigid body with a prescribed velocity as 0.2mm/ms in the downward direction. The contact between the punch and the sample was modelled using penalty formulation. The punch was treated as the master part while the sample was treated as the slave part. The static coefficient of friction was chosen as 0.4 while the dynamic friction coefficient was chosen as 0.2.

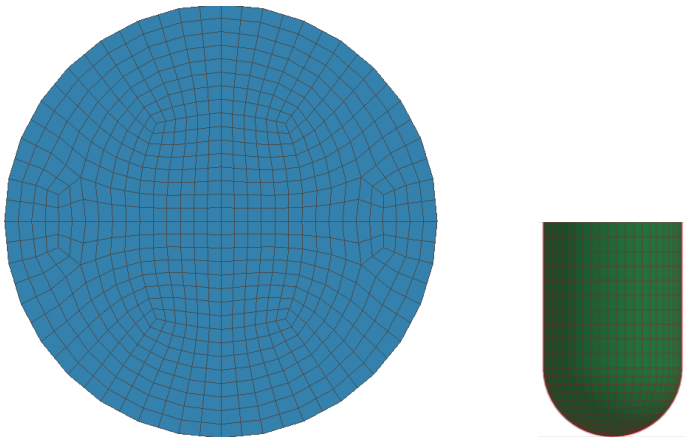

Figure 7.5 Mesh for sample R=38mm and punch R=25.4mm

7.3.3 Solver, Simulation Time and Timestep

All simulations are run using explicit solver. The total simulation time are reduced to 1/1000 of experimental time by scaling down the relaxation time constants τ_i accordingly. The timestep is determined by the shortest element size L_C and the speed of sound for shell element as $\Delta t = L_c/\sqrt{E/\left((1-\nu^2)\rho\right)}$ [11], where the modulus E is the instantaneous modulus $G_\infty+\sum G_i$ and ρ is the density. The timestep is scaled down to half of the computed timestep to make the simulation stable.

7.4 Verification With Existing Material Models in LS-DYNA®

7.4.1 MAT_076 and MAT_002 in LS-DYNA®

The model is firstly verified with MAT_076 *MAT_GENERAL_VISCOELASTIC to examine the implementation of viscoelasticity/rate dependency. Then the model is compared with MAT_002 * MAT_ ORTHOTROPIC_ELASTIC to examine the implementation of anisotropy.

MAT_076 is an isotropic model. In MAT_076, the required inputs are the constants in bulk relaxation modulus function $K(t) = \sum_{i=1}^{i=6} K_i e^{-\beta_{K_i} t}$ and shear relaxation modulus function$\mu(t) =$

$\sum_{i=1}^{i=6} \mu_i e^{-\beta_{\mu_i} t}$. The rate effects are taken into account through linear viscoelasticity by a convolution integral [12]

$$\sigma_{ij} = \int_0^t g_{ijkl}(t-\tau)\frac{\partial \varepsilon_{kl}}{\partial \tau} d\tau \tag{7.16}$$

$K(t)$ and $\mu(t)$ are calculated from the tensile relaxation modulus $G(t)$ as $K(t) = \frac{G(t)}{3(1-2\nu)}$ and $\mu(t) = \frac{G(t)}{2(1+\nu)}$. Decay constants β are calculated as the reciprocal of the relaxation time τ.

Next the model is verified with an existing model in LS-DYNA® MAT_002 * MAT_ ORTHOTROPIC_ELASTIC. Elastic properties obtained at force ramp rate 0.1N/min in [6] were used. However, it is hard to measure ν_{23}. A parameter study of ν_{23} as 0.1, 0.2 and 0.3 is carried out to see the influence of ν_{23} on the calculated strain.

7.4.2 Verification of Isotropic Viscoelastic Model with MAT_076

Uniaxial loadings in Fig. 7.4 are simulated using isotropic model using material parameters in [13]. All the simulated results as shown in Fig. 7.6a-d agree well with the one using MAT_076. For stress relaxation and creep tests, the simulation results agree well with analytical solutions as listed in Table. 7.1. This indicates the developed method works as expected. For uniaxial tensile test as shown in Fig. 7.6e, the simulated stress-strain curve is rate dependent for both using the model and MAT_076.

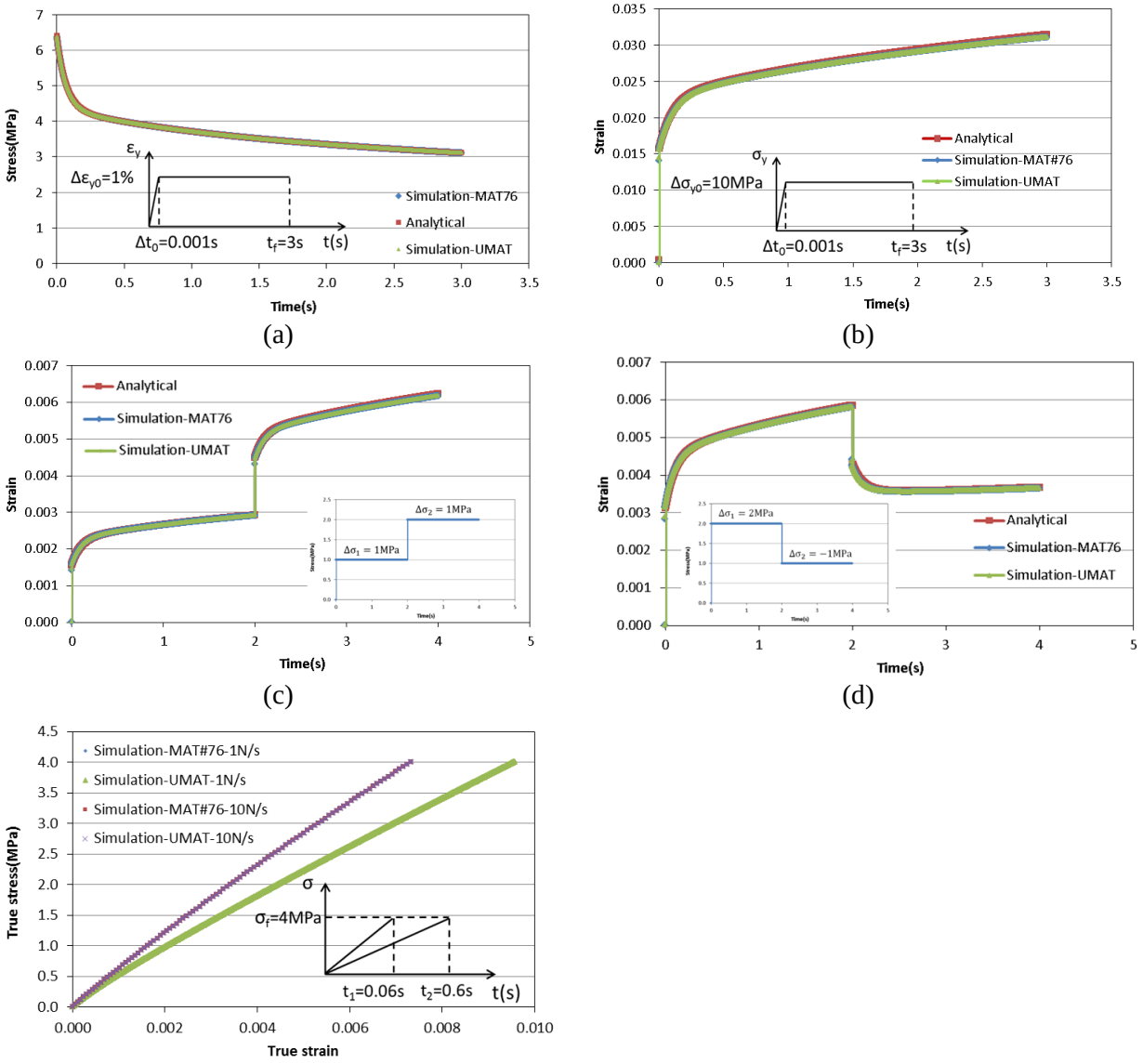

Figure 7.6 Comparison of simulation results using the developed model and MAT_076 and analytical solutions of uniaxial test (a) Stress relaxation (b) Creep (c) Creep test with two steps (case 1) (d) Creep test with two steps (case 2) (e) Tensile test at different force ramp rates

Table 7.1 Analytical solutions

Uniaxial Loading	Analytical solution
Stress relaxation [2]	$\sigma(t)=\Delta\varepsilon_{y0}\times G(t)$
Creep test [2]	$\varepsilon(t)=\Delta\sigma_{y0}\times J(t)$
Creep test with two steps (case 1) [2]	• 0~2s, $\varepsilon(t)=\Delta\sigma_1\times J(t)=1\times J(t)$ • 2~4s, $\varepsilon(t)=\Delta\sigma_1\times J(t)+\Delta\sigma_2\times J(t-2)=1\times J(t)+1\times J(t-2)$

Table 7.1(cont'd)

Creep test with two steps (case 2) [2]	• 0~2s, $\varepsilon(t) = \Delta\sigma_1 \times J(t) = 2 \times J(t)$ • 2~4s, $\varepsilon(t) = \Delta\sigma_1 \times J(t) + \Delta\sigma_2 \times J(t-2) = 2 \times J(t)\text{-}1 \times J(t-2)$
Off-axis creep test	$\begin{bmatrix}\varepsilon_1\\ \varepsilon_2\\ \gamma\end{bmatrix} = \begin{bmatrix}J_{11} & J_{12} & 0\\ J_{12} & J_{22} & 0\\ 0 & 0 & J_{44}\end{bmatrix}\begin{bmatrix}\Delta\sigma_1\\ \Delta\sigma_2\\ \Delta\tau\end{bmatrix}$, $\begin{bmatrix}\Delta\sigma_1\\ \Delta\sigma_2\\ \Delta\tau_{12}\end{bmatrix} = \begin{bmatrix}m^2 & n^2 & 2mn\\ n^2 & m^2 & -2mn\\ -mn & mn & m^2-n^2\end{bmatrix}\begin{bmatrix}\Delta\sigma_{x0}\\ \Delta\sigma_{y0}\\ \Delta\tau_{xy0}\end{bmatrix}$[14] $m = \cos\theta, n = \sin\theta$[14]

Isotropic viscoelastic model is also examined in the biaxial punch test. The patterns of X strain, Y strain and 1st principal strain was very close using this model and MAT_076 at the same punch displacement. Fig. 7.7 compares the results at displacement of 2.4mm. 1st principle strain was observed here because it could be an indication of separator failure [10].

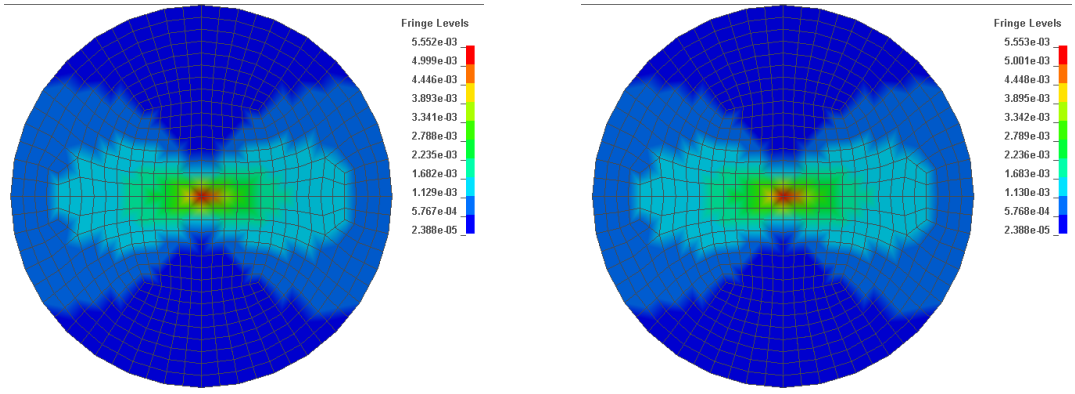

(a) (b)

Figure 7.7 (a) X strain predicted using MAT_076 (b) X strain predicted using isotropic viscoelastic model (c) Y strain predicted using MAT_076 (d) Y strain predicted using isotropic viscoelastic model (e) 1st principle strain predicted using MAT_076 (f) 1st principle strain predicted using isotropic viscoelastic model

Figure 7.7(cont'd)

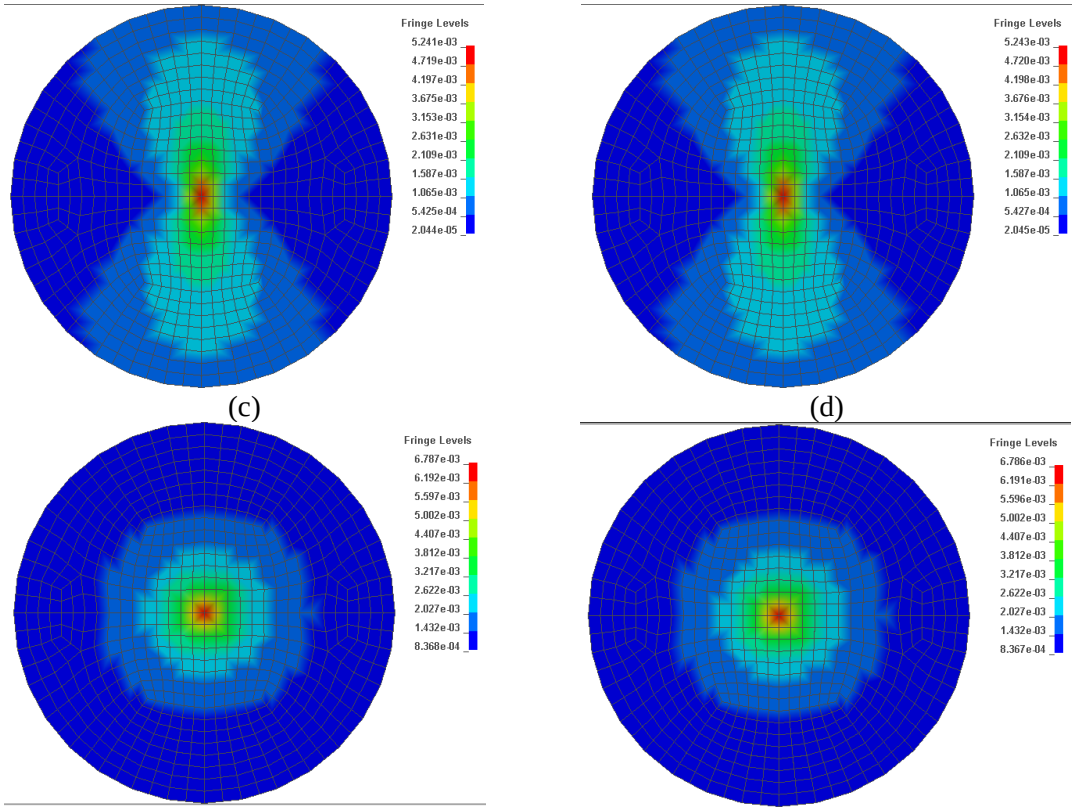

7.4.3 Comparison of Orthotropic Viscoelastic Model with MAT_002

Orthotropic viscoelastic model is compared with MAT_002 in the biaxial punch test. The patterns of MD strain, TD strain and 1st principal strain was very close using viscoelastic model and MAT_002 at the same punch displacement 2.4mm, as shown in Fig. 7.8. v_{23} does not have influences on these predicted strains when v_{23} is chosen as 0.1 or 0.3.

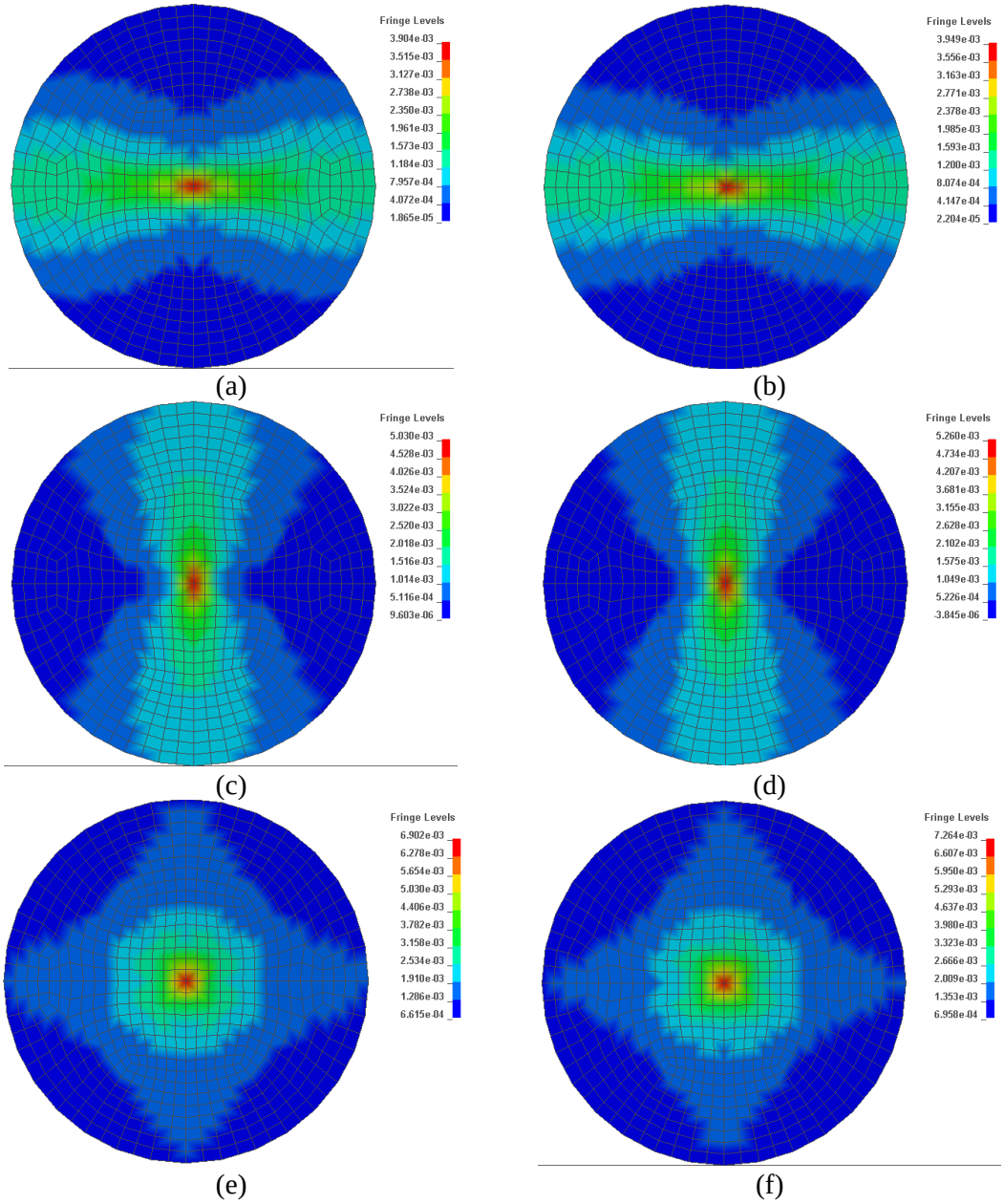

Figure 7.8 (a) MD strain predicted using MAT_002 (b) MD strain predicted using orthotropic viscoelastic model (c) TD strain predicted using MAT_002 (d) TD strain predicted using orthotropic viscoelastic model (e) 1st principle strain predicted using MAT_002 (f) 1st principle strain predicted using orthotropic viscoelastic model

The predicted strain showed anisotropic pattern. The maximum MD strain in Fig. 7.8a&b is smaller than maximum TD strain in Fig. 7.8c&d because Young's modulus along MD is larger than the one along TD. The 1st principle strain pattern in Fig. 7.8e&f is different from the one predicted in Fig. 7.7e&f. This is attributed to the small value of G_{12}. In this work G_{12} is measured

as 0.1GPa. The 1st principle strain pattern looked similar when G_{12} was 0.05 and 0.01GPa in Fig. 7.9a&b, but the pattern became more isotropic when G_{12} is increased to 0.2 and 0.3GPa in Fig. 7.9c&d. Similar pattern could be obtained using data from [15] in Fig. 7.9e. In [15], G_{12} was measured as 0.044GPa while Young's modulus along MD was close to our measurement as 1GPa with a much smaller Young's modulus along TD which was ~1/3 of our measurement. Therefore, the in-plane shear deformation contributed to the anisotropy of 1st principle strain pattern.

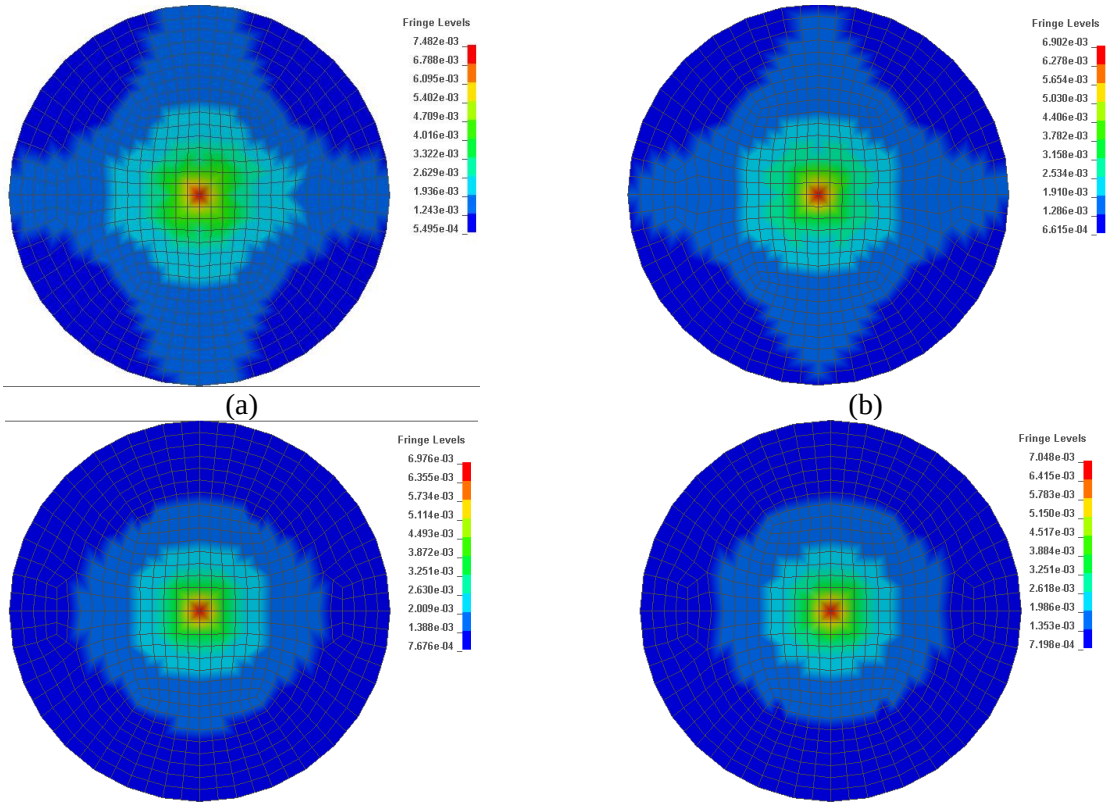

Figure 7.9 1st principle strain predicted using (a) G_{12}=0.05GPa (b) G_{12}=0.1GPa (c) G_{12}=0.2GPa (d) G_{12}=0.3GPa (e) Data in [15]

Figure 7.9(cont'd)

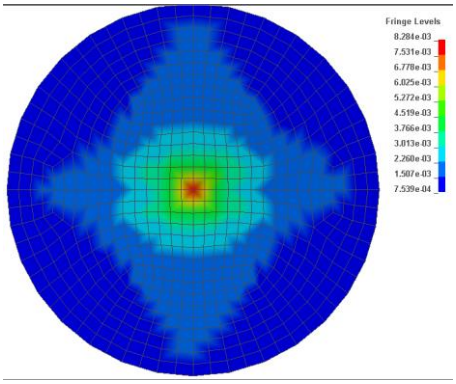

(e)

7.5 Validation of Orthotropic Viscoelastic Model with Experiments and Analytical Solutions

The simulated creep strains along MD, TD and longitudinal direction of 45° off-axis as shown in Fig. 7.10a-c agree well with the experimental data at linear range as 5MPa for MD, 2MPa for TD, and 2MPa for 45° orientation [6]. In 45° off-axis test, the simulated strains along each direction (MD, TD and shear) in material coordinate system as shown in Fig. 10d-f agree well with the analytical solution as listed in Table. 7.1.

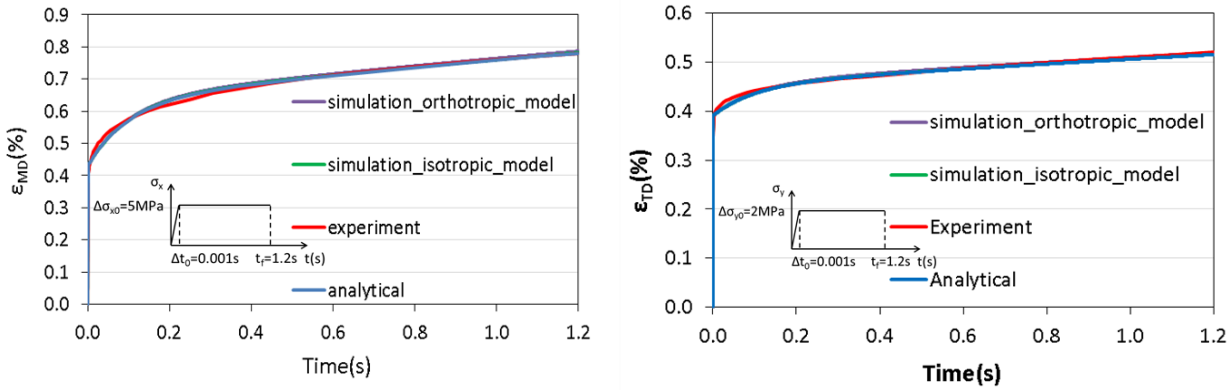

(a) (b)

Figure 7.10 Comparison of simulated creep strain with experimental data and analytical solutions (a) along MD (b) along TD (c) along longitudinal direction of 45° off-axis test (d) along MD of 45° off-axis test (e) along TD of 45° off-axis test (f) along shear direction of 45° off-axis test

Figure 7.10(cont'd)

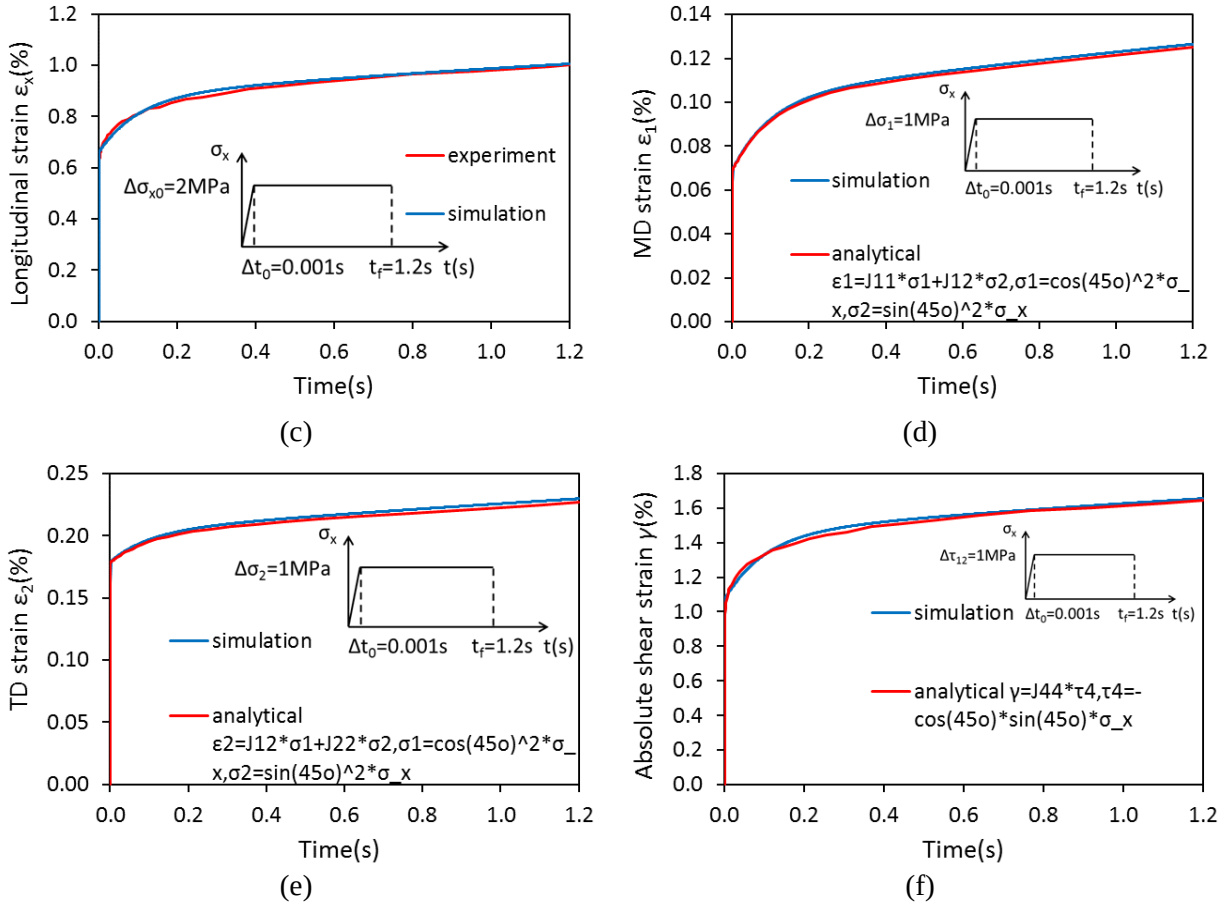

The simulated tensile behaviors along MD, TD and longitudinal direction of 45° off-axis test are rate dependent, which agree reasonably well with the experiments at force ramp rates 0.1N/min, 1N/min and 10N/min as shown in Fig. 11a-c. In 45° off-axis test at force ramp rate 0.1N/min, the simulated strains along each direction (MD, TD and shear) in material coordinate system as shown in Fig. 11d agree reasonably well with the experimental data [6].

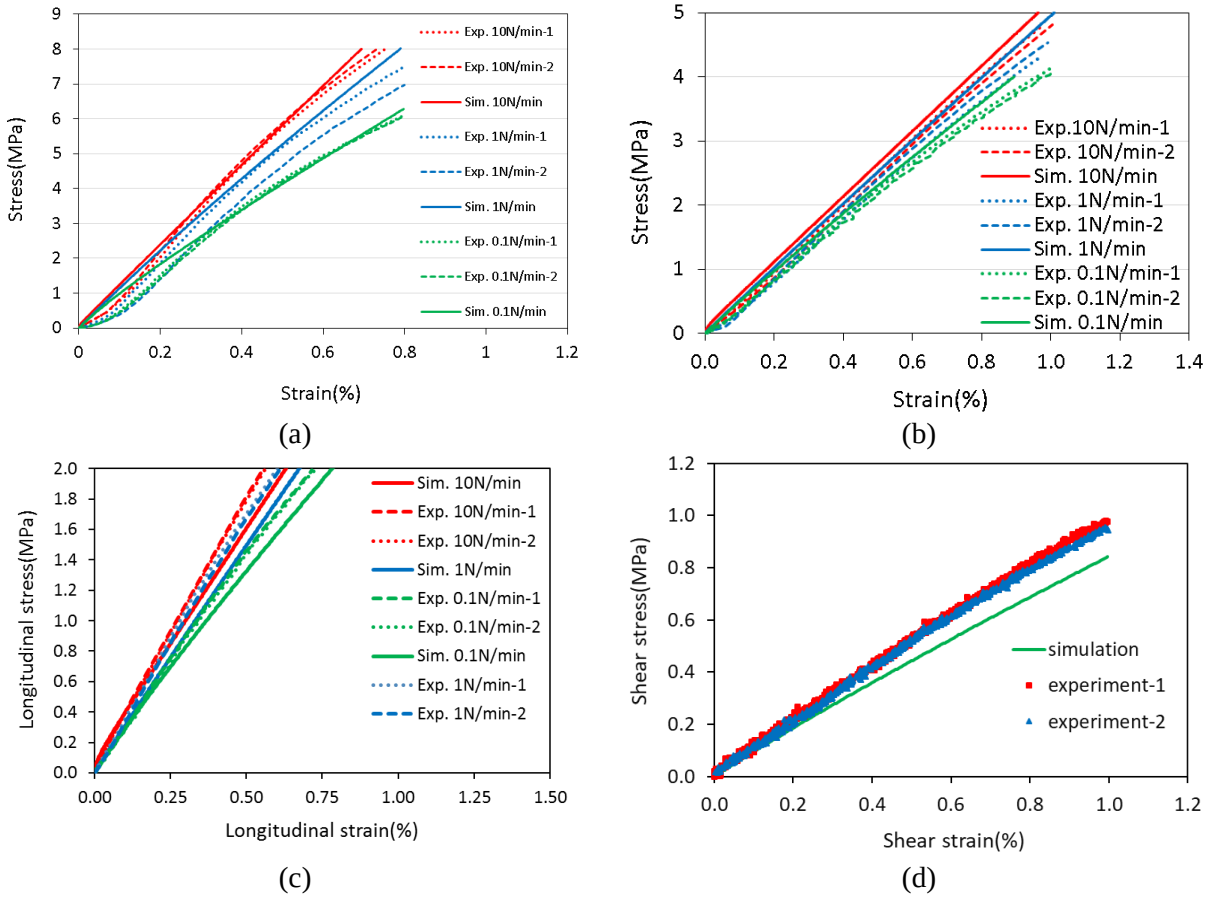

Figure 7.11 Comparison of simulated stress-strain with experimental data (a) along MD at different force ramp rates (b) along TD at different force ramp rates (c) along longitudinal direction of 45° off-axis test at different force ramp rates (d) along shear direction of 45° off-axis test at force ramp rate 0.1N/min

7.6 Conclusion

The thermomechanical model is developed on an orthotropic viscoelastic framework. A discretization algorithm has been proposed for the evaluation of a stiffness-based hereditary integral with a kernel of Prony series. The model has been implemented in commercial FE package LS-DYNA®. It is verified with experiments under uniaxial loading conditions and examined for biaxial loading condition.

REFERENCES

REFERENCES

1. J.D. Ferry, Viscoelastic Properties of Polymers, Wiley, New York, 1980.

2. I.M. Ward, J. Sweeney, An Introduction to the Mechanical Properties of Solid Polymers, John Wiley & Sons, West Sussex, 2004.

3. M.A. Puso, J.A. Weiss, Finite Element Implementation of Anisotropic Quasi-Linear Viscoelasticity (QLV) Using a Discrete Spectrum Approximation, Journal of Biomechanical Engineering, 120 (1998) 62-70.

4. R. Behrou, A Thermo-Poro-Viscoelastic Model for the Behavior of Polymeric Porous Separators, ECS Transactions, 80 (2017) 583-591.

5. R.M. Haj-Ali, A.H. Muliana, Numerical finite element formulation of the Schapery non-linear viscoelastic material model, International Journal for Numerical Methods in Engineering, 59 (2004) 25-45.

6. S. Yan, Y. He, A. Asta, J. Deng, C. Bae, X. Xiao, Characterization of the In-plane Orthotropic Viscoelastic Property of a Polymeric Battery Separator, Polymer Testing, 72 (2018) 46-54.

7. E. Sahraei, E. Bosco, B. Dixon, B. Lai, Microscale failure mechanisms leading to internal short circuit in Li-ion batteries under complex loading scenarios, Journal of Power Sources, 319 (2016) 56-65.

8. X. Zhang, E. Sahraei, K. Wang, Deformation and failure characteristics of four types of lithium-ion battery separators, Journal of Power Sources, 327 (2016) 693-701.

9. X. Zhang, E. Sahraei, K. Wang, Li-ion battery separators, mechanical integrity and failure mechanisms leading to soft and hard internal shorts, Scientific Reports, 6 (2016) 32578.

10. S. Kalnaus, A. Kumar, Y. Wang, J. Li, S. Simunovic, J.A. Turner, P. Gorney, Strain distribution and failure mode of polymer separators for Li-ion batteries under biaxial loading, Journal of Power Sources, 378 (2018) 139–145.

11. J.O. Hallquist, LS-DYNA® theory manual, Livermore Software Technology Corporation, 2006.

12. LS-DYNA® keyword user's manual, Livermore Software Technology Corporation, 2014.

13. A. Sheidaei, X. Xiao, X. Huang, J. Hitt, Mechanical Behavior of a Battery Separator in Electrolyte Solutions, Journal of Power Sources, 196 (2011) 8728-8734.

14. I.M. Daniel, O. Ishai, Engineering Mechanics of Composite Materials, Oxford University Press, New York, 1994.

15. J. Zhu, X. Zhang, T. Wierzbicki, Stretch-induced wrinkling of highly orthotropic thin films, International Journal of Solids and Structures, 139-140 (2018) 238-249.

CHAPTER 8 CONCLUSION AND FUTURE WORK

8.1 Conclusion and Summary

In this work, an orthotropic viscoelastic model has been developed for battery separators in LIBs. Thermal and mechanical properties characterization techniques have been developed for thin film with several dozen microns. The model can be implemented as orthotropic viscoelastic model in commercial FEM software. It can be incorporated in thermo-electro-mechanical battery model for vehicle crash simulation. The major summaries and findings are

8.1.1 In-plane Orthotropic Property Characterization Technique

Experimental methods have been developed to measure shear properties and Poisson's ratio. The shear properties were measured in uniaxial tension with specimens cut at an off-axis angle. The digital image correlation (DIC) technique was used in the strain measurements for the Poisson's ratio and the shear modulus.

The major and minor Poisson's ratios were found to follow the elastic symmetry relationship up to 1% longitudinal strain in TD.

The shear modulus determined from the DIC strain agreed well with that from the off-axis modulus and the elastic constants, which indicates that the separator follows the orthotropic elastic framework.

The creep compliances in shear and in the principal material directions were also determined. Based on the analogy for anisotropy between the elastic and linear viscoelastic domains, the shear creep response was measured with the off-axis tensile creep experiments.

8.1.2 Through Thickness Compression Characterization Technique

A capacitance-based displacement measurement set-up has been developed in house. This method allows to measure the TTD compression stress-strain behavior with double layer samples as thin as 50μm. It also allows to examine the interaction between the thin film and other materials, e.g., the electrodes. Comparisons of the experimental results in air and in DMC reveal that the separator compression modulus can be affected by the presence of DMC. The effect of solvent on modulus is similarity between TD and TTD while they are both smaller than that of in MD.

The iso-stress based rule of mixtures was also examined. The predicted compressive stress-strain curve for PP/NMC/PP stack was slightly stiffer first and then softer as compared to the experimental curve. Overall the prediction agreed with the experimental curve reasonably well up to about 0.16 strain. Above this strain, the measured response became increasingly stiffer than the prediction.

8.1.3 Thermal Expansion/Shrinkage Characterization Technique

Experimental method has been developed to measure thermal expansion/shrinkage of battery separators using a DMA. Calibrations are performed to determine the dimensional change of the testing fixture and to compensate for this contribution in the DMA measurement. The preloading level was reduced to minimize the creep contribution. The heating rate was reduced to minimize the thermal lag of temperature measurement between the thermocouple and the sample. The shrinkage data obtained from the DMA agreed well with the values obtained with an unconstrained sample under iso-thermal conditions. From the DMA results, the CTE relationships for three typical separators (PP, trilayer, and ceramic coated trilayer) have been established. DMA offers continuous measurements in an automatic fashion, which is an efficient and convenient method to characterize the thermal expansion/shrinkage behavior of thin polymer films.

It was found the dry-process polymeric separator Celgard® 2400 and 2325 have similar shrinkage behaviors. Their shrinkage in the MD is an order higher than that in the TD. With a layer of ceramic coating, Q20S1HX shows more isotropic shrinkage behavior which is an order smaller than MD shrinkage of polymeric separator.

8.1.4 Orthotropic Viscoelastic Modeling

The thermomechanical model is developed on an orthotropic viscoelastic framework. A discretization algorithm has been proposed for the evaluation of a stiffness-based hereditary integral with a kernel of Prony series. The orthotropic viscoelastic model has been implemented in commercial FE package LS-DYNA®. The implemented model has been verified under uniaxial loading conditions and examined for biaxial loading condition.

8.2 Future Work

The thermomechanical modeling of battery separator is not fully settled. As a first step, the current orthotropic viscoelastic framework was successfully implemented in LS-DYNA® and validated with experiments under uniaxial loading conditions. Next steps include model validation with biaxial load cases, model extensions, application to different type of battery separators and integration into coupled thermo-electro-mechanical analysis.

8.2.1 Model Extensions

To predict the mechanical integrity of separator during thermal ramp process, the model needs to be developed further. The following works are required:

(1) Validation with biaxial loading cases. A biaxial punch test has been identified as the test case.

(2) Temperature-dependent behavior. The relaxation modulus or creep compliances at elevated temperatures are needed.

(3) Electrolyte solvent effect needs to be considered.

(4) The model needs to be extended to large deformation including nonlinear viscoelastic and viscoplastic behavior.

8.2.2 Model Application To Different Types of Battery Separators

Currently the model is established for PP separator. It may be applicable for other different types of polymeric separator such as the dry-processed trilayer separators which are also anisotropic and have similar tensile behavior and thermal shrinkage behavior to PP separator; wet-processed separators which have more isotropic microstructure, tensile behavior and thermal shrinkage behavior; and ceramic coated separator.

8.2.3 Thermo-electro-mechanical Battery Model

The extended model will be examined for the prediction of the occurrence of various failure modes for thermal ramp scenarios in coupled thermal-mechanical analysis. It will then be integrated with the Randle circuit based battery model that is available in LS-DYNA® to be a part of thermo-electro-mechanical battery model for crash simulations.